XFEL.EU TR-2022-001A

TECHNICAL DESIGN REPORT

Scientific Instrument Soft X-Ray Port (SXP). Part A: Science cases

January 4, 2022

Manuel Izquierdo

on behalf of European XFEL and the international SXP community that contributed to the science cases

European X-Ray Free-Electron Laser Facility GmbH

Holzkoppel 4

22869 Schenefeld

Germany

Contents

List of Figures

List of Tables

1 Introduction

Manuel Izquierdo
European XFEL, Schenefeld, Germany

The European X-Ray Free-Electron Laser Facility (European XFEL, or EuXFEL) produces femtosecond coherent electromagnetic radiation in the soft and hard X-ray regimes by accelerating electrons up to 17.5 GeV in a superconducting linear accelerator (LINAC). This technology increases the typical 10–120 Hz repetition rate achievable with other LINACs to the kHz–MHz regime. At the European XFEL, the bunch pattern consists of bursts up to 2700 pulses with 220 ns separation running at 10 Hz frequency. This results in an effective repetition rate of 27 kHz. The facility has been designed with five self-amplified spontaneous emission (SASE) tunnels [1], each of which can accommodate an undulator system. In the first implementation phase, three of the SASE tunnels were funded, thus defining the current day-one implementation of the project. The SASE1 and SASE2 tunnels have been equipped with planar undulators that produce horizontally polarized hard X-ray photons in the range of 5–30 KeV, depending on the acceleration energy of the electrons. On the other hand, the SASE3 undulators are optimized to produce soft X-rays between the carbon edge, 0.25 KeV, and 3.0 KeV. The installation of an afterburner will allow to generate variable polarization soft X-ray pulses. The experiment hall provides space to host three experiments at each SASE branch (Fig. 1.1), two defined as baseline instruments. For SASE3, the experiments are Spectroscopy and Coherent Scattering (SCS) and Small Quantum Systems (SQS). The experiment hutch for the third experiment was built during the SASE3 construction. The area, initially named “SCS/SQS-II open port”, has been renamed following the European XFEL convention to “Soft X-Ray Port (SXP)”.

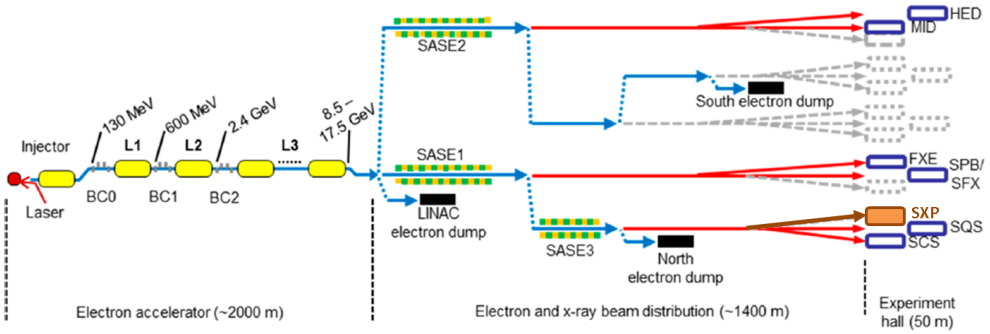

Figure 1.1: Layout of the European XFEL, modified from [1]

The SXP project is driven by groups of the soft X-ray scientific community with scientific applications requiring the use of experiment stations beyond the ones available at SCS and SQS. Among them, the motivation and funding provided by the Time Resolved X-Ray Photoelectron Spectroscopy (TR-XPES) consortium has been essential for the realization of this project. From the European XFEL, many groups have provided a key contribution to the project: X-Ray Optics (XRO), X-Ray Photon Diagnostics (XPD), Mechanical Engineering (ME), Project Management Office (PMO), Satety and Radiation Protection (SRP), and Sample Environment and Characterization (SEC).

This first part of the technical design project summarizes the identified science cases for the SXP experiment. It is organized as follows: this chapter revises the properties of SASE3 FEL radiation and proposed extensions to improve its performance. The remaining chapters describe the scientific applications proposed so far by the scientific community. They come from a broad potential user community as well as from internal European XFEL groups. The significant contribution of the Time-Resolved X-Ray Photoelectron Spectroscopy (TR-XPES) consortium described in Chapter 2 on page 20 is the main driving force that has led to the realization of this project. This is a direct consequence of the SAC recommendation to install the TR-XPES station(s) at SXP in order to implement the technique at SASE3. Since SXP is conceived as an open port, the momentum given to the SXP project by the TR-XPES consortium was followed by suggestions and contributions from other groups coming mainly from different European XFEL partner countries. These manifested contributions involve: (i) soft X-ray spectroscopy of high-valent metal intermediates in biological and inorganic catalysts for chemical bond activation (Chapter 3 on page 67), (ii) the possible use of SXP as a laboratory for astrophysics, atomic physics, and fundamental research with highly charged ions (Chapter 4 on page 73) and (iii) the use SXP to develop new diagnostics or experimental techniques (Chapter 5 on page 83). These science cases, techniques, and experimental setups will extend the portfolio of European XFEL beyond the baseline.

1.1 SASE3 photon beam properties

The SASE3 experiments have been defined to operate in the energy range of 0.25–3.0 KeV. The selected energy is defined by the undulator parameter, K, which depends on the undulator gap value and the electron acceleration energy. The gap value can be varied between its physical limits: 10–25 mm. As a consequence, the full energy range cannot be covered with a single electron energy. Instead, a few electron-acceleration-energy working points have been defined: 8.5, 12, 14, and 17.5 GeV. They set the low energy threshold to 0.25 keV (C K-edge), 0.48 keV (O K-edge), 0.710 keV, and 1.01 keV, respectively. The two highest energies will enable reaching the maximum photon energy of 3.0 keV. Figure 1.2 on the facing page summarizes the defined operation acceleration energies for SASE3 and how they cover the respective soft X-ray photon energy range. The calculations have been extended beyond the maximum nominal value of 25 mm for the lowest electron acceleration energies in order to show the highest photon energies that could be produced by the SASE3 undulators. Operation of the undulator systems at gap values larger than 25 mm is mechanically possible, the lasing stability and pulse energy remain to be verified. The SASE3 undulator system is placed after the SASE1 undulator system as indicated in Figure 1.1 on page 8. The electron dump system for both SASE1 and SASE3 is at the end of the SASE3 undulator system. As a consequence, electron bunches will radiate in both SASE1 and SASE3 undulator systems, thus coupling them. The energy spread introduced in SASE1 by the FEL radiation process will result in a degradation of the SASE3 output. The higher the radiation level in SASE1, the lower in SASE3. In order to minimize the contamination introduced by the SASE1 pulses, a soft kick can be given to the SASE3 dedicated electron bunches. The kick will induce a betatron oscillation in the orbit of the electron bunches and therefore they will radiate only in SASE3. This "fresh bunch technique" has been tried using soft kicks, and the level of radiation in SASE1 has been reduced down to the percent level. This mode work wells for fast detection detectors. For low frequency detectors, the background contamination can be still too high. In this case, other schemes can be used: i) 5 Hz operation split trains between the two SASEs thus decoupling their radiation. The interleaved mode provides alternative pulses for each SASE while still working at 10 Hz [2]. Other schemes can be implemented with the bunch pattern server that allows independent configuration of the pulses for each SASE [3].

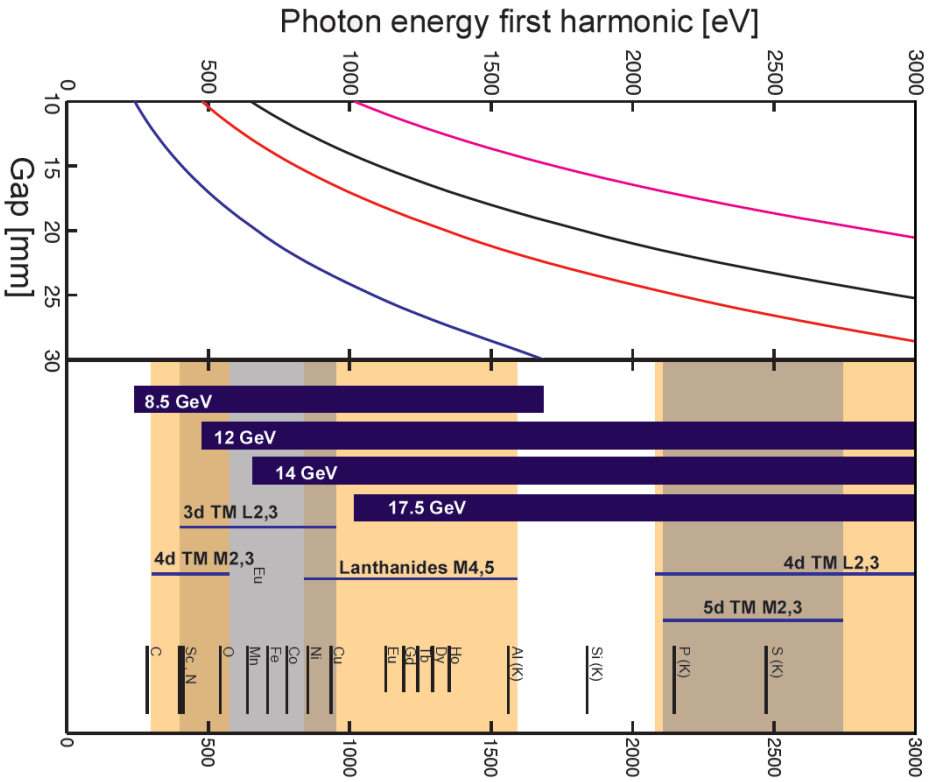

Figure 1.2: SASE3 electron acceleration working points in GeV and the respective photon energies covered by them

The SASE3 photon beam properties have been updated for the new electron energies in terms of source size, source divergence, pulse energy, and spectral bandwidth as a function of bunch charge and wavelength. The source parametrization as well as its coefficients and definitions can be found in Appendix A. The accelerator has been designed to operate with bunch charges between 0.1 and 1 nC. The pulse duration depends linearly on the electron charge with a slope of ~100 fs/nC [4]. In the left panel of Figure 1.3 on the following page, the expected peak and average brightness are displayed. In the right panel, the pulse energy is displayed for two values of the charge, 0.02 nC and 1 nC, that will result in ~2 fs and ~100 fs, respectively. The values have been calculated using the results from [4]. Based on the number of photons per pulse expected for different charge values, a few operation modes with a given number of pulses have been defined and are summarized in Appendix B.

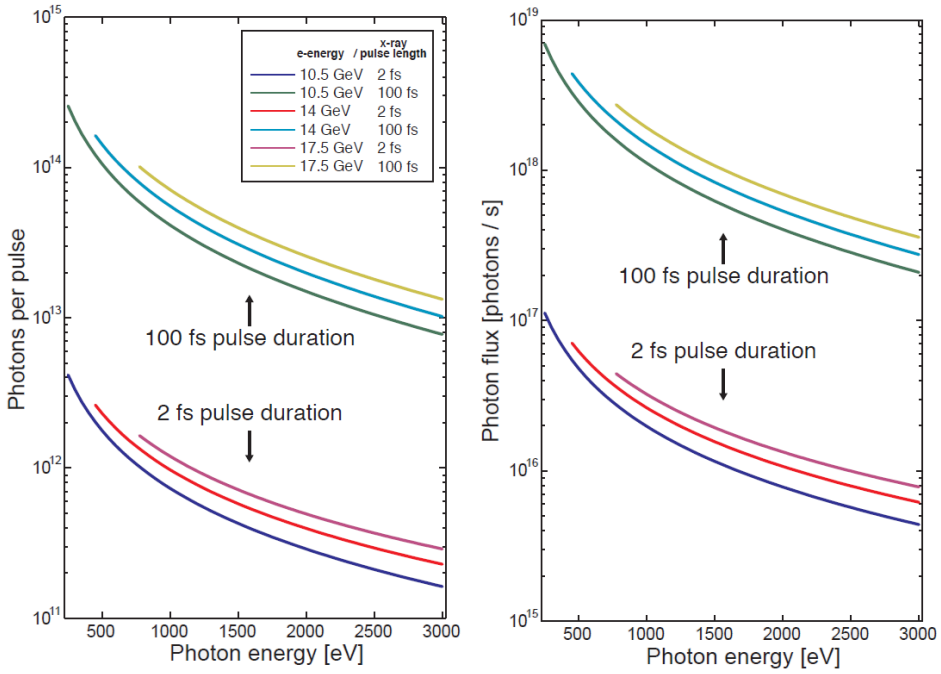

Figure 1.3: SASE3 pulse properties for two different electron charge values from [5]. *Left panel:* Photons per pulse. *Right panel:* Photon flux. Two charge values have been used: 0.02 nC and 1 nC covering the available charge range at the EuXFEL.

The polarization of the photons will initially be linear. In order to have variable polarization, two afterburners with a modified Delta design are going to be installed. Besides this, other extensions of SASE3 also under implementation consider the integration of harmonic laser self-seeding (HLSS) and two-colour pulse generation. The different possibilities are described in Section 1.2 on the next page. More involving techniques in terms of hardware upgrades—like self-seeding, attosecond production, or the integration of an X-ray split and delay unit—have also been studied. They are described in Appendix C.

1.2 SASE3 beyond the baseline

Extensions of the X-ray delivery capabilities at SASE3 have been studied. They cover a wide range of possibilities, from the generation of circularly polarized light to the production of attosecond pulses. In the framework of this report, they can be divided in two categories: (i) Those that are being implemented or planned: HLSS FEL (Section 1.2.1), variable polarization (Section 1.2.2 on page 15), and two-colour experiments (Section 1.2.3 on page 18). (ii) Those under study or for which implementations have been proposed so far are described in Appendix C: self-seeding (Section C.0.1), attosecond generation (Section C.0.2), or X-ray pump – X-ray probe experiments using a split and delay unit (Section C.0.3). Their final implementation is subject to the availability of funding. Technical modifications are to be expected before their final implementation, based on the evolution of the field.

1.2.1 HLSS FEL

One possibility to improve the properties of SASE FEL radiation using the existing undulator systems is using a harmonic lasing self-seeded (HLSS) FEL. This technique also allows the extension of the wavelength of the radiation with respect to the fundamental radiation with an increase in radiated power and smaller bandwidth than the fundamental. The latter requires the suppression of the fundamental wavelength. This can be achieved by different techniques: phase shifters, filters, etc. [6; 7].

The basic idea of HLSS is to amplify the lasing at a high harmonic h and use it as a seed to lase at a given photon energy. Besides an increase in the radiated power, there is also a reduction of the bandwidth. The latter occurs due to the fact that the bandwidth, $\Delta\lambda$, can be defined in terms of the Pierce parameter $\rho \sim \Delta\lambda/\lambda$, indicative of the radiation-interaction efficiency and proportional to the inverse of the harmonic number. This contrasts with the non-linear harmonic generation that occurs during SASE lasing. In this case, the bandwidth is independent of the harmonic number.

Several theoretical strategies have been proposed for hard and soft X-rays and for fixed-gap and variable-gap FELs [7]. One of them, HLSS versus the retuned fundamental mode, has been demonstrated at the “Free-electron LASer in Hamburg (FLASH)” for third-harmonic lasing [8]. The implementation was done by tuning the first part of the undulators to the K value corresponding to a harmonic of the fundamental and the second part of them to the K value of the fundamental one.

Provided that a beta function larger that the harmonic gain length can be achieved in the electron beam, conditions can be found in which the gain length of the harmonic is shorter than that of the fundamental. In this case, the radiation power of the harmonics can be efficiently amplified.

On the left side of Figure 1.4, the scheme of the HLSS is depicted. On the right side, the calculations done for SASE3 at 4.5 nm using an acceleration energy of 10.5 GeV are provided [7]. The results show that the third harmonic can be amplified up to 12% and the fifth harmonic up to 3% without suppressing the fundamental lasing. Upon suppression of the fundamental, the radiation power of the harmonics is increased one order of magnitude compared to the non-linear harmonic generation (2% and 0.3% for third and fifth harmonic, respectively [9]). Besides the significant increase in the radiated power, the bandwidth is inversely proportional to the harmonic number. HLSS therefore improves the properties compared to SASE radiation.

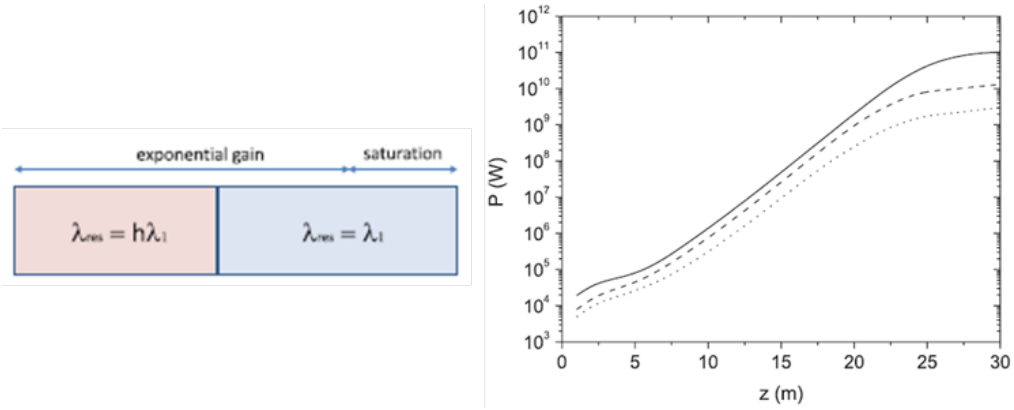

Figure 1.4: *Left:* Scheme of the harmonic lasing self-seeded using the retuned fundamental mode. *Right:* Radiated power for the SASE3 undulator system at 4.5 nm: solid line (fundamental), dashed line (third harmonic), and dotted line (fifth harmonic). The power generated is typically one order of magnitude larger than that obtained with non-linear harmonic generation. The bandwidth is inversely proportional to the harmonic order.

HLSS has been successfully demonstrated at the SASE3 undulator system [10]. Two implementations have been done, one at 2.1 keV (0.59 nm) and the second one at 4.5 keV (0.28 nm). The first HLSS was achieved using 12 undulator sections. The first five segments were tuned to the third harmonic h =3, 700 eV, and the subsequent 7 cells to the fundamental at 2.1 keV. Radiation levels of 700 µJ have been achieved with a reduction of the number of spikes. The expected factor of R=2 increase of the longitudinal coherence (reduction of the bandwidth) could not be achieved due to chirp in the electron system. On the other hand, the 4.5 keV (0.28 nm) was achieved by the so called harmonic lasing cascade. In this case, the undulator is divided

in three parts. The first one comprising five undulator sections lases at the fifth harmonic, the second part with six undulators is set to lase at the third harmonic and the last one with also six undulators at the fundamental. Radiation levels of 200 µJ have been achieved.

HLSS will be available at SXP since day one. The available energy range depends on the electron acceleration energy since one needs to be able to radiate at the harmonic *h* wavelengths and the low energy cutoff is defined by it (see Figure 1.2 on page 11). Moreover, the longitudinal coherence will depend on the electron chirp. An alternative and complementary approach would be to use self-seeding described in Appendix C.

1.2.2 Variable polarization

The baseline undulators at the European XFEL are planar and can therefore produce horizontal polarized radiation. In order to produce circularly polarized soft X-rays, two afterburners will be installed in the SASE3 undulator tunnel. The afterburners are Apple-X type and have been developed at the Paul Scherrer Institute (PSI) for the Athos beamline at SwissFEL. They are a modified version of the Delta undulators implemented at the SLAC National Accelerator Laboratory Linac Coherent Light Source (LCLS) [11]. The magnetic pole arrangement, displayed in Figure 1.5 on the next page, is similar in both types of undulators. The main difference is that, in the Apple-X, the magnetic field strength, and therefore the K parameter, is changed by changing the gap (movement perpendicular to the undulator axis) of the horizontal/vertical magnet arrays, $K_{Tot} = \sqrt{(K_x^2 + K_y^2)}$, whereas, in the Delta undulator, the change in K is done by an amplitude shift (movement along the undulator axis) of one of the horizontal/vertical pole versus the other. In both cases, the polarization is changed by a phase shift (movement along the undulator axis) of the two horizontal field magnet arrays versus the vertical field ones. The gap change of the Apple-X undulator results in a larger region, ±0.8 mm in this particular case, where the magnetic field homogeneity is $\Delta/K_{Tot} < 5 \cdot 10^{-5}$. This allows sufficient alignment of a 30 µm RMS electron beam.

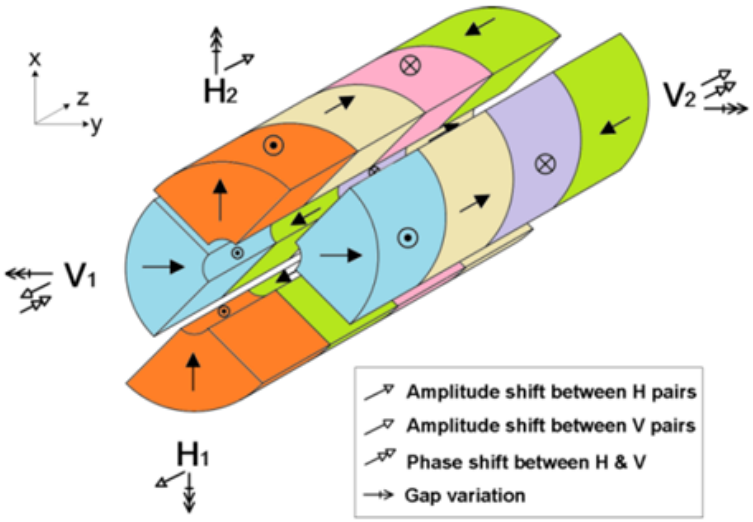

Figure 1.5: Geometrical configuration of the Apple-X undulators to be installed at the end of the SASE3 undulators to produce variable polarization. The change of the *K* parameter will be realized by changing the gap value. The polarization is changed by a phase shift of two horizontal arrays with respect to the two vertical ones.

The Apple-X undulators are designed to provide full polarization control over the wavelength range from 0.4 to 1.6 nm using a 15 GeV electron beam. In order to achieve this goal, a period of 90 mm has been chosen [12]. It will provide right/left circularly polarized radiation and alternatively linearly polarized radiation with an arbitrary polarization angle between $\pm 90°$. They will be placed after the 21 planar undulator segments in a collinear geometry. The implementation of the afterburner will be done using the same FODO lattice used for the planar undulators. For the planar undulators, the lattice is made by two quadrupoles (one focusing, one defocusing) and two undulator sections of 5 m length. The afterburners sections will be only 2 m long, and two of them they will be installed after each quadrupole section. The total length, 12.4 m, is slightly larger than that of the planar undulators, 12.2 m (Figure 1.6) [13].

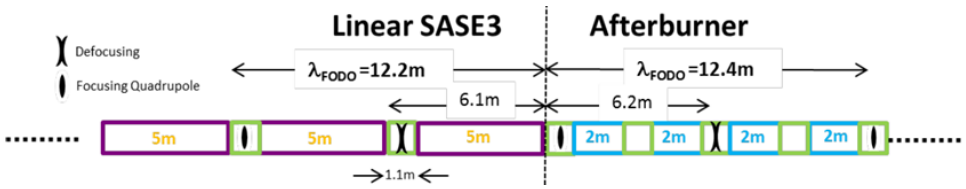

Figure 1.6: FODO configuration of the Apple-X afterburners at the end of the SASE3 undulators

To reduce the linearly polarized radiation produced by the planar undulators, a reverse tapering scheme can be applied to the linear undulator system. In this scheme, the undulator gap is closed along the electron propagation direction. This implementation allows building microbunching while minimizing the generated radiation [14; 13]. As a consequence, the linearly polarized radiation will be reduced by more than two orders of magnitude compared to the non-tapered level, and the afterburner polarized radiation will dominate in intensity. In Figure 1.7, the undulator configuration for reverse tapering is displayed on the top panel. The bunching factor and power obtained are displayed in the bottom panel.

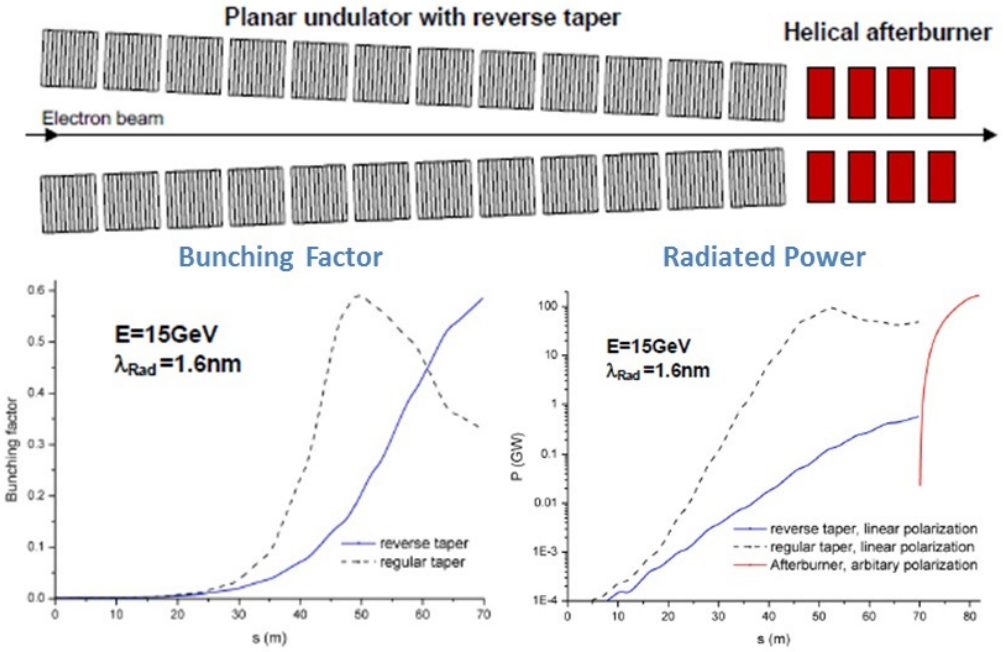

Figure 1.7: Reverse tapering concept to suppress the linear radiation versus the circularly polarized one. *Top:* Undulator gap in a reverse tapering scheme; the closer the gap, the lower the photon energy. *Bottom-left:* Evolution of the bunching factor along the undulator with (solid line) and without (dashed line) reverse tapering. *Bottom-right:* Expected radiated power of the planar undulator system with (solid line) and without (dashed line) tapering. The radiation of the afterburners is displayed in red for comparison. The implementation of reverse tapering reduces the radiated power in the planar undulator section by two orders of magnitude.

The installation of the afterburners to produce variable polarization is scheduled to the 2021 winter shutdown. This will provide variable polarization at SXP from day one.

1.2.3 Two-colour pulse generation

Following implementations at LCLS and SPring-8 Angstrom Compact Free Electron Laser (SACLA), the European XFEL Simulation of Photon Fields group has put forward a project aiming to generate two colours with the SASE3 undulator system. This implementation will allow the realization of X-ray pump – X-ray probe experiments. The two colours between the pulses can be arbitrarily chosen within the limits allowed by the electron acceleration energy [15]. The idea of the project is to divide the undulator system into two parts by inserting a magnetic chicane at a selected position. The gap in one part of the undulator will be set to lase at a wavelength λ_1, and the second part will be set to lase at a wavelength λ_2 as displayed in 1.8(a). The magnetic chicane between the two undulator parts has two purposes: (i) control the delay between the two pulses with the strength of the magnetic fields and (ii) wash out the microbunching produced in the first undulator part to start with a fresh electron bunch when the two wavelengths are contained within the SASE bandwidth. The best two-colour output in this configuration is achieved when λ_1 is shorter than λ_2. The time delay between the two pulses depends on the strength of the magnetic chicane and the electron acceleration energy.

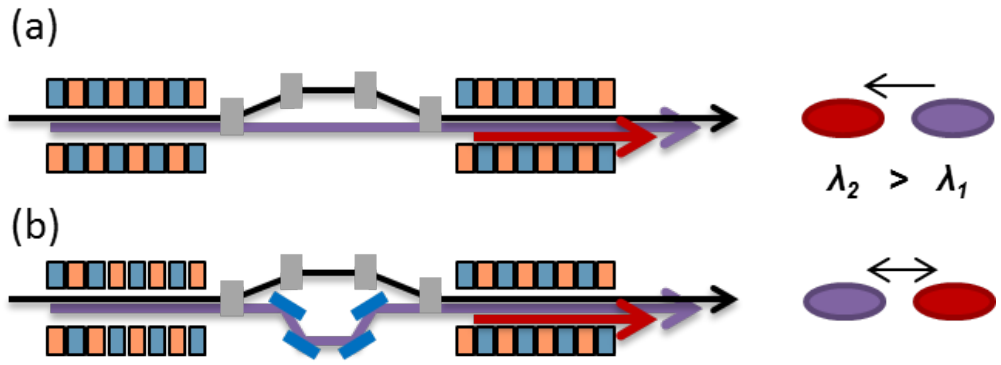

Figure 1.8: Two-colour configurations proposed at SASE3: (a) Using a magnetic chicane to produce delays between 0 and 1 ps. (b) Using both a magnetic chicane and a delay mirror unit to produce delays ±100 fs around zero delay.

An upgrade scheme of the one proposed above is to insert a delay mirror unit for the X-rays in front of the magnetic chicane (Figure 1.8(b)). This configuration will allow the realization of both positive and negative delays between the two wavelengths λ_1 and λ_2. The transversal size of the photon beam at this position will be in the same order of magnitude as the electron bunches, therefore allowing the use of short mirrors. The installation of a corrugated structure—an R&D project lead by the accelerator team—could also be beneficially coupled to the two schemes described above to

enable fresh bunching.

Two-colour experiments have been already implemented at SASE3. Test experiments were done without the magnetic chicane. Using two wavelengths separated by more than a SASE bandwidth allowed the production of two-colour pulses with a fixed delay. The installation of the magnetic chicane has allowed to extend the delay. The current range depends on the electron acceleration energy. It is ~ 3 ps for electrons 8.5 GeV accelerated electrons and ~ 1 ps for 17.5 GeV acceleration energy. The typical intensity of the two pulses is quite high, ~ 0.5 mJ/pulse. The ultimate performance is nevertheless defined by the selected photon energy.

2 Complete TR-XPES

Sebastian Thiess, Jens Buck, Chul-He Min, Kai Rossnagel[*]
Christian-Albrechts-Universität Kiel
[*] **also** ***FS-SXQM, DESY, Hamburg, Germany***

Lukas Wenthaus, Wolfgang Eberhardt
Center for Free Electron Laser Science, DESY, Hamburg, Germany

Michael Heber
Universität Hamburg, Hamburg, Germany

Gerd Schönhense, Jure Demsar, Katerina Medjanik
Institut für Physik, Johannes Gutenberg-Universität, Mainz, Germany

Claus M. Schneider, Christian Tusche
Fakulät für Physik, Universität Duisburg-Essen, Germany

Jaime Sánchez-Barriga, Andrei Varykhalov, Emile Rienks, Dmitry Marchenko, Florin Radu, Florian Kronast and Oliver Rader
Helmholtz-Zentrum Berlin für Materialien und Energie, BESSY II, Berlin, Germany

Olga V. Molodtsova[**], **Federico Pressacco, Dmytro Kutnyakhov**
DESY Photon Science, Hamburg, Germany
[**] **also** ***ITMO University, Saint Petersburg, Russia***

Friedrich Reinert, Christian Metzger, Kiana Baumgartner
Julius-Maximilians-Universität, Würzburg, Germany

Friedrich Roth
Institute of Experimental Physics, TU Bergakademie, Freiberg, Germany

Clemens Laubschat, Jochen Geck
Technische Universität, Dresden, Germany

Eckart Rühl
Freie Universität Berlin, Germany

Markus Scholz, Wei Lu, Chan Kim, Anders Madsen, Dimitrii V. Potorichin[***], **Manuel Izquierdo, Serguei Molodtsov**[***]
European XFEL GmbH, Schenefeld, Germany
[***] **also** ***ITMO University, Saint Petersburg, Russia, and TU Bergakademie, Freiberg, Germany***

Ekaterina Ivanova, Mikhail Lapushkin, Igor Pronin, Maxim Rabchinskii
Russian Academy of Science Ioffe PTI, St. Petersburg, Russia

Ekaterina Fedorovskaya
Novosibirsk State University, Novosibirsk, Russia

Alena Maratkanova
Russian Academy of Science UB FTI, Izhevsk, Russia

Maksim Gudkov
Russian Academy of Science CHPH, Moscow, Russia

Viktor Sivkov
Russian Academy of Science UB KSC, Syktyvka, Russia

Tatyana Asanova, Yuliya Fedoseeva
Russian Academy of Science SB IIC, Novosibirsk, Russia

Vladimir Kovivchak
Russian Academy of Science, SB OSC, Omsk, Russia

Sergey Turishchev
Voronez State University, Voronezh, Russia

Lada Yashina
Lomonosov University, Moscow, Russia

Daniil Itkis
Russian Academy of Science CHPH, Moscow, Russia

Tatyana Kuznetsova, Alexey Shkvarin
Russian Academy of Science UB IMP, Ekaterinburg, Russia

Sergey Kasatikov, Dmitrii Pudikov, Artem Rybkin, Victor Shevelev
Saint Petersburg University, St. Petersburg, Russia

Leon Avakyan, Yuriy Dedkov, Arshak Tsaturyan, Alexander V. Soldatov
Southern Federal University, Rostov-on-Don, Russia

Victor Y. Aristov
Russian Academy of Science, ISSP, Chernogolovka, Russia

Fausto Sirotti, Jacques Peretti, Alistair Rowe
LPMC, CNRS, Ecole Polytechnique, France

Luca Perfetti, Jelena Sjakste, Matteo Gatti[****]**, Lucia Reining**[****]
Laboratoire des Solides Irradiés, Ecole Polytechnique, Palaiseau, France
[****] **also *ETSF: European Theoretical Spectroscopy Facility***

Lenart Dudy, Jean-Pascal Rueff, Mathieu Silly
SOLEIL Synchrotron, L'Orme des Merisiers, Saint Aubin, France

Evangelos Papalazarou, Marino Marsi
Laboratoire de Physique des Solides, CNRS, UPSay, France

Guy Le Lay
Aix-Marseille University, CNRS, PIIM UMR 7345, Marseille, France

Veronique Langlais
CEMES - CNRS Centre d'Élaboration de Matériaux et d'Etudes Structurales, Paris, France

Maurizio de Santis
Institut NEEL, Grenoble, France

Emmanuel L'huillier, Charlie Greboval, Herve Cruguel
Institut NanoSciences, Paris, France

Sebastien Sauvage
Centre de Nanosciences et Nanotechnologies, Palaiseau, France

Giancarlo Panaccione, Riccardo Cucini, Martina Dell'Angela, Giorgio Rossi[*****]
IOM, Consiglio Nazionale delle Ricerche, Trieste, Italy
[*****] **also** ***Dipartimento di Fisica, Università di Milano, Milano, Italy***

Paolo Moras, Polina M. Sheverdyaeva, Carlo Carbone
ISM, Consiglio Nazionale delle Ricerche, Trieste, Italy

Claudio Masciovecchio, Tevfik O. Mentes, Andrea Locatelli
Elettra Sincrotrone Trieste, Basovizza, Trieste, Italy

Francesco Offi
CNISM and Dipartamento di Scienze Universitá Roma Tre, Rome, Italy

Irene de Padova, Roberto Flammini, Stefano Colonna
Istituto di Struttura della Materia CNR-ISM, Rome, Italy

Stefan Jurga
NanoBioMed Centre AMU, Poznań, Poland

Maciej Kozak[******], **Adam Mickiewicz**[******], **Artur Stefankiewicz, Maciej Wiesner**
University Poznań, Poland
[******] **also** ***NCPS SOLARIS, Krakow, Poland***

Marco Roy
University of Medical Sciences, Poznań, Poland

Piotr Kuświk
Institute of Molecular Physics, Polish Academy of Sciences, Poznań, Poland

Jacek Szade
University of Silesia and SOLARIS, Poland

Maciej Chrobak, Michal Jurczyszyn, Krzysztof, Mackosz, Marcin Sikora
AGH University of Science and Technology, Krakow, Poland

Bogdan Kowalski, Andrzej Wiśniewski, Tomasz Story
Institute of Physics, Polish Academy of Sciences, Warsaw, Poland

Geoff Thorthon
Centre for Nanotechnology and Chemistry Department, University College Londond, United Kingdom

Charlotte Sanders, Yu Zhang
UKRI and STFC, Didcot, United Kingdom

Cephise Cacho, Karol Hricovini, Jan Minar, Marco Battiato, Sarnjeet Dhesi
Diamond Light Source, Didcot, United Kingdom

Philip Hoffman, Søren Ulstrup, Simon Wall, Jill Miwa
University Aarhus, Denmark

Peter Bøggild, Peter Uhd Jepsen
Denmark Technical Universtiy Copenhagen, Denmark

Ulf Karlsson
Physics Department, University Linkoping, Sweden

Mats Götlid, Martin Månsson, Oscar Tjernberg, Jonas Weissenrieder
KTH Royal Institute of Technology, Stockholm, Sweden

Anders Nilsson
University Stockholm, Sweden

Yasmine Sassa
Chalmers University, Gothenburg, Sweden

Yves Acremann
***ETH Zü*rich**

Claude Monney
University of Fribourg

Nicholas Plumb, Milan Radovic, Valerio Scagnoli, Ming Shi, Vladimir Strocov
Swiss Light Source, Paul Scherrer Institut, Villigen, Switzerland

Maria Eugenia Dávila
Instituto de Ciencia de Materiales de Madrid ICMM-CSIC, Madrid, Spain

Virginia Pérez Dieste, Debora Pierucci
CELLS-ALBA Experiments Division, Cerdanyola del Vallés, Spain

Enrique Ortega, Frederik Schiller, Celia Rogero
Centro Física de Materiales CFM-CSIC, San Sebastian

Jorge Lobo-Checa
Instituto de Ciencia de Materiales de Aragón ICMA-CSIC, Zaragoza, Spain

Eva Mateo-Martí, Maria Paz Zorzano-Mier, Eduardo Cueto Díaz, Laura Jiménez Bonales, Santos Gálvez Martínez, Cristina Pérez Fernéndez
Centro de Astrobiología INTA-CSIC, Madrid, Spain

Leonardo Soriano de Arpe, Pilar Prieto Recio, Carlos Morales Sánchez*******
Departamento Física Aplicada, Universidad Autónoma de Madrid, Spain
******* **also** ***Brandemburg Technological University, Cottbus, Germany***

Xavier Torrelles, Adrian Crespo
Institut de Ciència de Materials de Barcelona ICMAB-CSIC, Barcelona, Spain

Jordi Llorca, Núria J. Divins, Lluís Soler, Xavier Vendrell, Isabel Serrano
Group of nanoengineering of materials applied to energy, Universitat Politècnica de Catalunya - BarceloaTech (UPC)

Arturo Martínez Arias, José Carlos Conesa Cegarra, Patricia Pérez Bailac, Elies Omari********
Instituto de Catálisis y Petroleoquímica ICP-CSIC Madrid, Spain
******** **also** ***Universidad de Biskra, Algeria***

Víctor A. de la Peña O'Shea, Marta Liras, Fernando Fresno, Mariam Barawi, Miguel Gómez, Freddy Oropeza
IMDEA Energy, Madrid, Spain

Avelino Corma, Mercedes Boronat, Patricia Concepcion
Instituto de Tecnología Química, Universidad Politécnica de Valencia, CSIC-UPV, Valencia, Spain

Hernán Míguez, Juan F. Galisteo López, Mauricio E. Calvo Roggiani, Carlos Romero Pérez, María Morán Pedroso
Grupo Materiales Ópticos Multifuncionales, Instituto de Ciencia de Materiales de Sevilla ICMS-CSIC, Sevilla, Spain

Agustín, R. González-Elipe, Juan Pedro Espinós Manzorro, Francisco Yubero Valencia, Ana I. Borrás, Angel Barranco, Victor Rico Gavira
Nanotechnology on Surfaces and Plasma Laboratory, Instituto de Ciencia de Materiales de Sevilla ICMS-CSIC, Sevilla, Spain

Ginesa Blanco Montilla, José M. Pintado Caña, Adrián Barroso Bogeat, Juan José Pérez Sagasti
Grupo de Química de Sólidos y Catálisis. Departamento de Ciencia de los Materiales e Ingeniería Metalúrgica y Quımica Inorgánica de la Universidad de Cádiz, Cádiz, Spain

Neus Domingo, Irena Spasojevic, Christina Stefani
Catalan Institute of Nanoscience and Nanotechnology (ICN2), CSIC and BIST, Barcelona, Spain

Felix Brausse, Oliver Geßner
Chemical Science Division, Lawrence Berkeley National Laboratory, Berkeley, USA

This application has been proposed by the TR-XPES user consortium at European XFEL. The aim is to realize comprehensive photoelectron spectroscopy with soft X-rays and femtosecond time resolution for the study of ultrafast electron dynamics as illustrated in Figure 2.1. In order to achieve this ambitious goal, a photoemission group was created in 2012 with contributors representing the photoemission community at the European level and beyond. The proposition to create a photoemission user consortium was presented and positively evaluated at the Scientific Advisory Committee (SAC) meeting in September 2013. A full proposal was presented and approved at the SAC meeting in September 2015. The SAC recommended to implement the project at the open port in SASE3, SXP.

Photoelectron spectroscopy (PES) is an essential analytical tool for probing the properties and working mechanisms of materials and interfaces, where the functionality is determined by the chemical state and/or electronic band structure. PES measures the kinetic energy and momentum components (i.e. surface-parallel momentum, spin polarization, and orientation) of the valence and core level electrons emitted from a sample as a result of the photoelectric effect. The technique combines high spectral resolution with the momentum selectivity and atomic-site specificity,

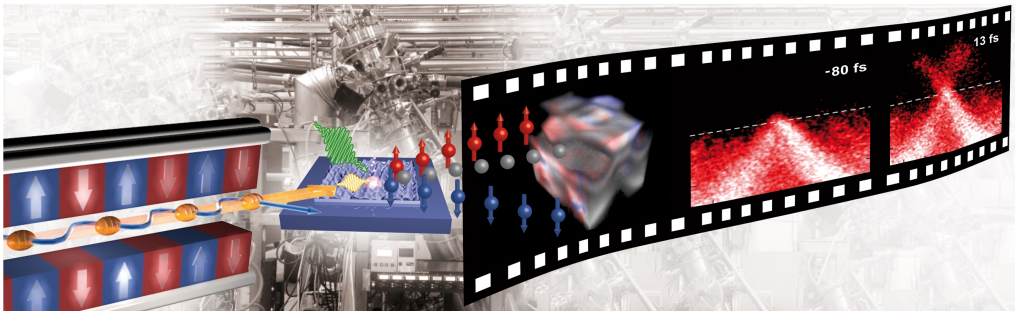

Figure 2.1: Schematic illustration of FEL-based femtosecond time-resolved photoelectron spectroscopy with combined spin and momentum resolution

respectively. It can thus provide direct information on electronic band dispersions in energy-momentum space as well as on the local chemical and structural environment of the emitting atoms. Although most of the photoelectrons are emitted from near-surface regions, using harder X-rays, PES can also probe bulk properties and buried interfaces and discern corresponding electronic states. Since photoemission is a many-body process, the measured spectra generally contain information on the excitation spectrum and excitation probabilities of the probed system under investigation.

The development of the PES technique to the current state of the art is strongly linked to the evolution of accelerator-based photon sources. It is at synchrotrons where the technique reached its maturity and positioned itself as an essential tool in solid state physics, material science, and nanotechnology. Nowadays, PES is a toolbox comprising four major techniques differing on the origin of the electrons, delocalized valence states, or localized core levels electrons, and the way they are analysed (see e.g. [16; 17; 18]).

Angle-resolved photoelectron spectroscopy (ARPES) is the most powerful imaging technique for the energy-momentum space of the active electrons near the Fermi level [16; 17]. The unique capabilities of ARPES originally played a key role in the study of high-temperature superconductor cuprates. Since then, the applications of ARPES expanded and the technique has become one of the most important methods for exploring the electronic structure of materials. Currently, in the condensed matter field, the technique is focusing on so-called “quantum materials”. The definition addresses *solids with exotic physical properties, arising from the quantum mechanical properties of their constituent electrons* [19; 20]. Under this generic qualification, one finds a plethora of the most currently studied materials in view of their interesting properties as well as potential applications: high critical temperature superconductors, topological insulators, colossal magnetoresitance

oxides, ferroelectrics, 2D electron gases, Weyl metals, graphene, etc.

In principle, ARPES measures (matrix element-weighted) energy- and momentum-dependent photo-hole excitation spectra (the spectral function) that are images of the band structure as modified by interactions of the photo-hole quasiparticle, with shifted and broadened bands reflecting its energy renormalization and finite lifetime (as described by the complex self-energy), respectively. The energy-momentum maps directly visualize the occupied part of the global electronic structure as well as its local fine structure. This includes the structure and topology of Fermi surfaces, the symmetry and momentum dependence of energy gaps, specifically superconducting gaps, and kinks in band dispersions or band replica due to electronic coupling to phonons or other collective excitations, as well as characteristic signatures in the bulk and surface electronic structures of topological materials, such as bulk band gaps, bulk Dirac and Weyl cones, and topologically protected (spin-momentum-locked) Dirac surface states or surface Fermi arcs. When spin resolution is added to an ARPES experiment, additional information can be gained directly on electron spin as a central player in correlated electron and topological materials. Traditionally, energy- and momentum-dependent spin structures have been measured for itinerant ferromagnets, where bulk bands are spin-split due to exchange interaction, and for nonmagnetic Rashba systems, where surface states are spin-split due to spin-orbit interaction and inversion-symmetry breaking. More recently, spin-resolved ARPES has become a key in determining the complex spin textures in energy-momentum space of topological materials. While the initial success of ARPES was obtained performing experiments in the ultraviolet (UV) energy range, $h\nu < 100$ eV, in the last decades, soft and hard X-ray ARPES have been quickly developed. The higher photoelectron kinetic energies gives more validity to the free-electron approximation of the final state normally used to analyse the data. It also results in a wider coverage of energy-momentum space, over many Brillouin zones, and better-defined momentum components perpendicular to the surface, due to the enhanced electron scape depth. This facilitates full energy-momentum *microscopy* of 4D electronic structures (photoemission intensity as a function of energy and all three momentum components), often with simpler interpretation of matrix-element effects compared to UV-ARPES. Furthermore, soft X-rays allow accessing electronic resonances where the excitation energy is near the absorption threshold of a core level which can be exploited to enhance or suppress selected valence-electron emissions for identifying their elemental and orbital characters or clarifying the nature of satellites and final-state configurations. The increase in sampling depth from the typical 10 Å of UV photons to more than 10 nm has been key to address open questions in correlated oxides like vanadates, manganites, cuprates, and other quantum materials in the vicinity of phase transition where the surface and bulk properties are different. It has also opened new frontiers in the study of interfaces

in heterostructures where the electronic properties derive from the reduction of the dimensionality.

X-ray photoelectron spectroscopy (XPS) is a universal tool for chemical analysis. The source of information is the energy-resolved photoemission from core levels, which is dominated by atomic effects. Spectral peak positions are highly element-specific, with very little overlap, and peak intensities depend among other factors on elemental concentrations, allowing analysis of the chemical composition. The core-level binding energies vary, depending on the effective charge, encoding the chemical state of the atomic species, the surrounding charge density, and the hybridization of valence levels, as influenced by bond lengths and coordination. This *chemical shift* allows a detailed interpretation of the chemical state of the emitting atom, although screening of the core-hole by the relaxation of the remaining electrons also needs to be considered. More generally, the core electron is a messenger carrying information on the electrostatic potential it was born in, which includes the physical environment, particularly the electrostatics of interfaces. A core-level spectrum principally consists of a main emission peak, representing the lowest-energy state after photoexcitation, and additional emissions (discrete or continuous satellites) at lower kinetic energy, reflecting the excited states of the interacting system. When many-body effects dominate and there is more than one final-state configuration (screening channel), complex satellite/multiplet structures can arise, allowing insight into many-body states and correlation effects. The richness of the information contained in a XPS spectrum has made it possible to obtain relevant information on the electronic properties and many-body interaction in strongly correlated systems and quantum materials. However, the field where the technique has excelled is that of the investigation of chemical reactions and catalysis. The evolution of the initial experiments on ideal systems in ultrahigh vacuum (UHV) conditions towards studies at realistic pressure conditions has given birth to the very powerful near ambient pressure photoemission (NAPP) technique [21].

Soft X-ray radiation allows covering the primary (1*s* and 2*p*) core levels of low to intermediate atomic numbers (Z), ranging from the 1*s* level of C (Z=6) to the 2*p* level of Ru (Z=44). In this section of the periodic table, the most scientifically and consequently relevant elements are found. They are also the most abundant on planet Earth, which make them the ideal candidates for the development of sustainable technologies. The known variations in photoionization cross sections can be utilized in XPS to select the degree of sensitivity to a particular core level. In this respect, XPS experiments performed with electron kinetic energies above 2 keV (HAXPES regime) have shown to be unaffected by surface effects and to display spectroscopic fingerprints representative of the bulk electronic properties[22; 23] in

analogous to the ARPES observations. Furthermore, the use of soft X-ray photons will allow the study of interface physics and electronic devices under electrical bias.

X-ray photoelectron diffraction (XPD) and related photoelectron holography are powerful methods for structural analysis of near-surface layers, buried interfaces, adsorbates, 2D materials, etc. based on scattering of the photoelectrons emitted from specific atomic sites. The scattered and directly emitted waves interferences produce an angle-dependent intensity modulation characteristic of the local structural environment. The fact that no long range-order is required made the technique an essential tool to determine the geometric arrangement of atoms and molecules adsorbed at surfaces, on the one hand, and the atomic structure of thin films, on the other. The versatility of the technique derives from its sensitivity to the kinetic energy of the analysed electrons. For low kinetic energies, 500 eV and below, the electrons are essentially backscattered; multiple scattering dominates and therefore XPD in this regime is best suited to understand the arrangement of the structures with respect to the substrate. The most efficient realization of the technique in this case is the so-called “energy scan mode”. In these type of measurements, the photon energy is scanned for a set of well-defined high-symmetry directions of the system. When the electron kinetic energy is above 500 eV, forward scattering is preferential, which allows, in first approximation, to interpret the intensity maxima in terms of straight-line emissions along directions from the emitting atom to its neighbours. Recording maps as a function of the emission angles, the technique is called angle scan XPD, produces a photoelectron diffraction pattern analogous to the ARPES maps used to measure Fermi surfaces. The chemical shift in the XPS spectra and its sensitivity to the chemical environment as well as to many body effects call for an extension of the XPD technique to extract information not only from the local structure but also from other relevant properties of the materials, like short-range magnetic order using spin-resolved modes. XPD has traditionally been pretty much used with soft X-rays since the interpretations of results is more straightforward in the forward scattering regime [24]. The development of XPD-HAXPES allows to increase sampling depth. This enhances the contribution of the *Kikuchi bands* arising from multiple scattering from Bragg planes [25]. The expectation is that, with the increasing sharpness of XPD patterns, finer structural details can be resolved and quantitative analysis will become easier.

Photoemission electron microscopy PEEM uses the differences in electron emission of different regions at a surface to image of it. The emitted electrons are accelerated with high voltage, typically between 10 and 20 keV, into an electron optical column made of electrostatic and/or magnetic lenses as well as corrector

elements required to image the electrons with a resolution defined by the distance between the sample and the microscope column, the difference in energy among the electrons, and the initial accelerating voltage. A resolution down to 20 nm can be achieved. In the simplest configuration, the image is recorded with an image plate. This requires the retardation of the electrons to energies where the efficiency is much higher. The imaging functionality can be improved by changing the hardware configuration after the electron optical column. Thus, adding an energy filter (time of flight of high pass energy), allows detecting the electrons as a function of their kinetic energy and obtain images with chemical sensitivity. A microanalyser configuration allows to perform XPS or PES in 1 µm regions of the sample. Special transfer lenses and energy filtering make it possible to perform “momentum-resolved measurements” either with time-of-flight (ToF) or conventional hemispherical analysers. Using micro-channel plates (MCPs) coupled with delay line detection (DLD), time-resolved measurements can be performed. PEEM and its low energy counterpart, LEEM, have been successfully used to study the morphology, electronic and chemical properties, and magnetic structure of surfaces and thin film materials [26; 18]. PEEM—in combination with circular and linear dichroism, commonly referred to as XMC/LD-PEEM—has become a hugely successful imaging technique at synchrotrons to visualize magnetic domains and domain walls in thin films and interfaces [27]. Most of the synchrotron applications also use the energy tunability together with the polarization control in order to realize X-ray absorption (XAS) imaging experiments, XAS-PEEM.

Besides these well established applications of PES, a very interesting experimental implementation has emerged in the 2000s, standing wave photoemission (SW-PES). The technique aims to convey the dominant contribution of the surface emitted photoelectrons to the detected PES intensity, even in the high X-ray HAXPES regime, in order to study the deepest layers of the sample under investigation. In order to realize this, the intensity profile of the incident electromagnetic field is tailored to highlight selected regions across the sample depth. This is technically done by using a synthetic multilayered mirror with nanometer period, matching the photon wavelength, as standing wave generator. The first reported implementation was done in the soft X-ray regime, 750 eV, and aimed to measure core levels (XPS) [28]. The intensity modulation of the electromagnetic field at different sample depths was done by performing an angular scan, rocking curve, around the selected reflection. Subsequent implementations have made use of wedge samples thus allowing to extract the layer dependent information by scanning the sample along the wedge direction. The first standing wave XPS studies (SW-XPS) have been extended over the years into the other applications: SW-ARPES, SW-PEEM, and even used to investigate magnetic systems SW-MCD [29]. Pioneering experiments combined with NAPP, have shown the potentiality of the technique to also study solid liquid interfaces

[30].

PES science at synchrotrons has mainly been done in the static regime. While many beamlines dedicated to static ARPES are available in most of the synchrotrons worldwide, time-resolved PES experiments are more scarce. The reason is that the time resolution for these type of experiments is limited to the picosecond timescale, whereas femtosecond resolution is achievable with laser-based sources. Laser sources have, on the contrary, limitations on the accessible energy range, and most of the time-resolved PES experiments are performed in the UV range, $h\nu < 100$ eV. The resulting landscape can therefore be factorized as a function of these two parameters: pulse duration and photon energy. ARPES and XPS experiments with picosecond resolution at energies up to the carbon edge have been implemented at the UVSOR and BESSY synchrotrons. In the soft X-ray regime, the BL5 at the SAGA light source allows experiments up to 0.8 keV, the TEMPO beamline at the SOLEIL synchrotron up to 1.5 keV, and Spring-8 up to 2 keV. The most widely used PES technique in the time domain at synchrotrons is XAS-PEEM. The main reason is that the sub-nanosecond temporal resolution provided by third-generation synchrotron sources fits very well with the timescale of the magnetization reversal [31] and spin precession [32; 33].

In the femtosecond time domain, ARPES has been very successful using the UV pulses produced by high harmonic generation (HHG) techniques with femtosecond near-infrared laser sources. Increasing the time resolution has dramatically expanded PES by allowing to capture the dynamics of the electrons, spins, and atoms on fundamental timescales, thus adding time as a new dimension and a powerful tool to understand complex materials. The femtosecond range corresponds to the sub-eV physics of condensed matter, as given by the meV energy scale of typical elementary excitations. Time-resolved measurements are generally realized in a pump–probe stroboscopic mode: a femtosecond laser pulse, the pump, excites a system into a non-equilibrium state, and the time-delayed probe, synchronized femtosecond (soft X-ray) pulse, monitors the system's response and relaxation. The use of ultrashort photon pulses limits the achievable energy-momentum resolution in pump–probe PES due to time-energy uncertainty and vacuum space-charge effects. But *high-resolution* spectroscopy remains possible, e.g. with 90 meV (FWHM) energy resolution at a time resolution of 20 fs (FWHM).

Time-resolved soft X-ray PES (TR-XPES) promises comprehensive stroboscopic movies of the fundamental electronic structure dynamics in energy-momentum space, including the population of electronic states and the probing of unoccupied states, combined with the atomic site-specific chemical and structural dynamics in real space. In a single experiment, we will be able to simultaneously track the motion of electrons, spins, and atoms on their natural timescales. TR-XPES will also be a creative tool

to access hidden or competing phases that are unattainable in equilibrium and to stabilize and probe entirely novel transient phases. TR-XPES in a NAPP environment will allow to understand chemical reactions and catalytic processes in realistic conditions. Time-resolved SW-PES will provide new opportunities to understand materials like the 2D electron gases buried at the interface between two oxides, multilayer structures, etc. The time variable will also allow investigating the properties of electronic devices, chemical and catalytic systems in-operando conditions.

Currently, the implementation of TR-PES with femtosecond resolution is limited by the photon energy range accessible. Laser-based sources are currently able to produce sufficient photon fluxes at kHz repetition rates to perform experiments up to ~150 eV using HHG techniques [34]. Many HHG implementations below 100 eV are currently available at universities but also as user facilities (ARTEMIS at CLF, NFFA at Elettra, JILA at Boulder, CELIA at Bordeaux, etc.). The production of soft X-rays with laser sources is theoretically possible and has been experimentally demonstrated up to the keV range. However, the maximum flux currently achievable has so far only allowed proof-of-principle experiments. One of the limitations arises from the fact that conventional phase matching required to produce intense HHG pulses is not possible with the typical wavelength of the most powerful femtosecond lasers, 800–1030 nm. Therefore, other implementations like quasi phase matching, use of two counter propagating beams, etc. need to be used and optimized. These techniques will also require the development of intense laser sources at longer wavelengths in the mid-infrared regime, $>$ 2000 nm. Recent successes in this direction have been achieved. High output power at 3000 nm as a first stage of a laser-based soft X-ray source have been recently reported [35]. This paves the way to produce intense photons pulses up to 1 keV for time-resolved PES experiments, thus extending the proof of principle demonstrations and theoretical calculations [36; 37].

Femtosecond PES experiments using accelerator-based sources are available only at free-electron lasers (FELs). The femtosecond pulses produced at slicing sources in synchrotrons are too weak to carry out successful PES experiments. Since the usable photon pulse energy for the successful implementation of PES is limited to the nJ due to space charge effects, the ideal sources need to have at least kHz repetition rate. This calls for the use of FELs with superconducting acceleration technology. In this respect, the FLASH FEL in Hamburg has pioneered the implementation of TR-PES experiments. The facility produces photons up to the carbon edge in the first harmonic. Experiments with a third harmonic up to $\sim$ 1 keV are possible, and results have been reported [38; 39; 40; 41]. The current energy range accessible allows, like in the case of laser-based sources, to realize complete PES experiments, but only shallow core levels in backscattering geometry can be studied. On the hard X-ray end, a proof-of-principle demonstration of HAXPES using 60 Hz repetition rate has been

done at SACLA.

The concept of fs TR-XPES experiments is depicted in Figure 2.2. The chosen example is 1T–TaS_2. The first two panels show ARPES measured with an HHG source [42] and XPS experiments using the FLASH FEL at 165 eV [43]. The diffraction experiments were measured with ultrafast electron diffraction [44]. The ultimate dream of performing complete PES combining ARPES, XPS, and XPD using soft X-rays is now possible at the SASE3 undulator system of the European XFEL. The soft X-ray range available will allow to perform XPD experiments in forward scattering, thereby opening the unique possibility to investigate all the degrees of freedom of materials with femtosecond resolution. The same capabilities will also be available at LCLS-II up to 5 keV after the upgrade is completed. PES is one of the proposed techniques to address three of the six broad areas of science in which LCLS-II has proposed to open new frontiers [45].

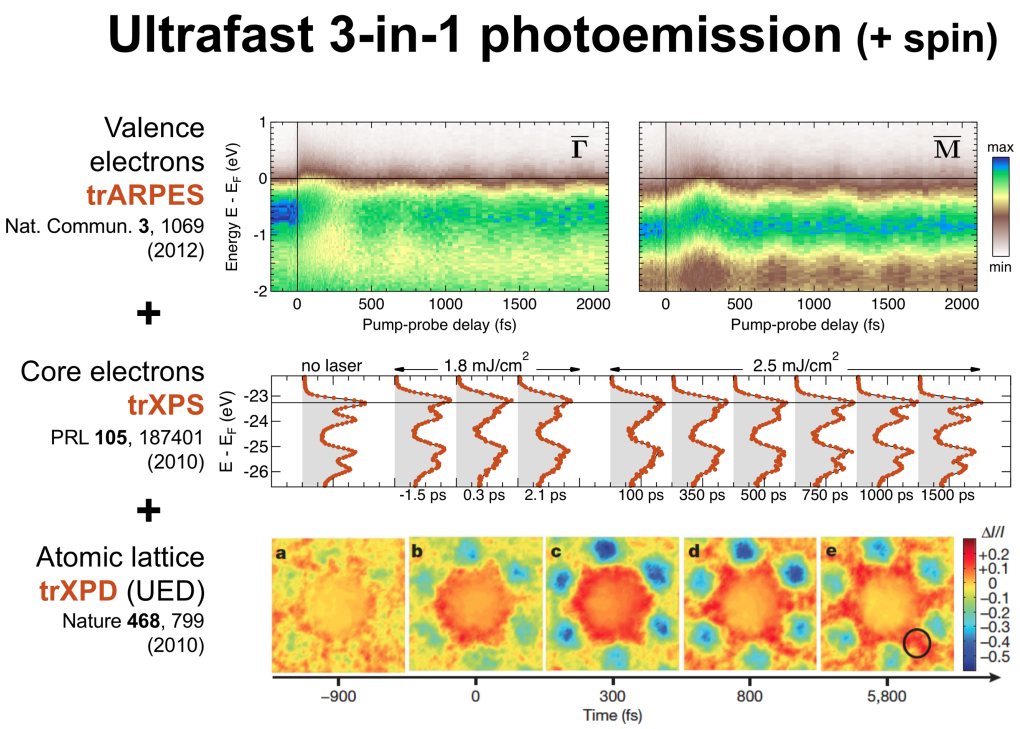

Figure 2.2: Complete time-resolved soft X-ray PES combines time-resolved ARPES, XPS, and XPD into a single experiment and it would allows simultaneous measurement of the time-dependent electronic, chemical, and geometric structure as well as spin structure. Top and middle panels in the figure correspond to PES and XPS measurements on 1T–TaS_2. The bottom panel is a diffraction pattern measured using ultrafast electron diffraction (UED) on the same compound. Equivalent experiments could be done using soft X-ray photoelectron diffraction (XPD).

The implementation of TR-XPES at the SXP experiment in the SASE3 undulator

system is of paramount importance for the scientific community since it will provide a unique environment to investigate unexplored scientific possibilities. On the one hand, TR-XPES expands the energy limits of the FLASH FEL and HHG laser sources to the soft X-ray domain. On the other hand, it allows improving the time resolution currently available at synchrotrons. The implementation of the afterburner to produce variable polarization Section 1.2.2 on page 15 will also allow the realization of spin-resolved experiments both at the valence band and core levels. Besides the broad soft X-ray range that will be used to explore the properties of materials, SXP will benefit from a laser system with a wide tunable wavelength, THz to UV, to cover the characteristic meV to eV energy scales of materials. The controllable excitation fluence (μJ/cm^2 to mJ/cm^2) will allow to go seamlessly from weak to strong perturbation.

The singular possibilities of the TR-XPES project at SXP make it fully compatible and complementary to the goals of other existing European facilities like ESRF or ELI [46; 47] and other sources available to the user community: CLF, SOLEIL, BESSY, FERMI, CITIUS, and NFFA. The TR-XPES project, together with the implementation of TR-PES at LCLS-II, provides the only soft X-ray PES experiments for the user community foreseen so far. Future developments in the field are to be expected, like the upgrade of FLASH to 1 keV or the development of laser-based soft X-ray sources with sufficient flux to carry PES experiments. Altogether, these sources are expected to contribute to the development of complete femtosecond time-resolved photoemission.

2.1 Photoemission science opportunities

Electron dynamics underlies all fundamental processes in chemistry and materials physics; it is intellectually challenging in complex quantum materials and technologically relevant at solid interfaces. Complete time-resolved soft X-ray PES is the ideal tool to study electron dynamics, including spin dynamics, and its intertwining with short-range structural dynamics at the fundamental level, as the dynamics happens in real time in materials and at interfaces. The inherently multimodal technique allows comprehensive characterization of transient states by providing time-dependent snapshots of the electronic, magnetic, chemical, and geometric structure, as shown in Figure 2.2. This unique capability will enable unprecedented insights into underlying microscopic mechanisms. Complete time-resolved soft X-ray PES, as envisioned here, can allow the understanding of key questions in the dynamics of materials science (see e.g. [48; 49; 50]).

2.1.1 Measuring the electron–phonon coupling interaction strength

The fascinating properties and rich electronic behaviour of materials emerge from the interactions of their electronic (charge, spin, orbital) and lattice degrees of freedom. Measuring the strength of the interactions is crucial but often difficult because of the multiplicity of competing interactions. Time-resolved methods can separate a specific interaction from other effects and probe its strength directly. A well-known example is the measurement of the electron–phonon coupling parameter (λ) by time-resolved spectroscopy, originally for metals [51], but later also for other materials, including semiconductors, superconductors, ferromagnets, and strongly correlated electron systems. An ultrashort laser pulse creates a non-equilibrium electron distribution in a cold lattice; the hot electrons thermalize with the lattice on a picosecond timescale via electron–phonon interactions; and the measured thermal relaxation rate gives the coupling parameter. This approach has been extended to extracting the couplings between multiple baths of e.g. electronic charges, their spins, and phonons from the rate of energy flow between them [52]. More recently, an intriguingly direct and purely experimental method has been realized to measure the electron–phonon coupling strength in materials, as quantified by the deformation potential, i.e. the band energy shift per underlying atomic displacement [53]. The approach is based on coherent phonon-generation in two separate time-resolved experiments on the same material: the oscillations in the atomic displacement corresponding to a specific phonon mode are extracted from time-resolved X-ray diffraction data, while the coherent phonon-induced oscillations in the energy of specific electronic

states are measured by time-resolved ARPES. Quantitative combination of the diffraction and spectroscopy results provides a remarkably precise value for the phonon mode–specific and electronic state–specific deformation potential. In practice, however, the approach faces the challenge of providing similar sample and excitation conditions for separate experiments. Complete time-resolved ARPES will allow to track the pathways of quasiparticle scattering throughout energy-momentum space and measure quasiparticle lifetimes and non-equilibrium electron temperature. In combination with XPS and XPD, it will allow measuring electron–phonon coupling using a single photon probe.

2.1.2 Understanding the ultrafast dynamics of phase transitions

Many materials undergo phase transitions involving charge, spin, orbital, or lattice degrees of freedom, as they are strongly intertwined. The delicate interplay of competing phases often manifests itself in complex phase diagrams, typically displayed as temperature versus doping or pressure plots. The driving mechanism of phase transitions is one the central topics in condensed matter physics. Besides its scientific interest, phase transitions often have technological applications. There is a wide variety of materials to investigate: colossal magnetoresistance manganites, titanates, multiferroic oxides, superconducting cuprates, etc.

Understanding phase transitions thermodynamically is often cumbersome since the phase changes are relatively slow. Femtosecond laser pulses, by contrast, can drive the transition from one phase to another on ultrafast (i.e. sub-picosecond) timescales due to the coordinated dynamics of electronic and lattice degrees of freedom, or at least lead to a rapid (partial) quenching of orders. Time-resolved pump–probe techniques are then used to measure the speed and magnitude of the changes and determine to what degree they are nonthermal, i.e. not driven by rapid lattice heating. Yet, the central theme is to apply temporal discrimination to disentangle the complex interplay of electronic (charge, spin, orbital) and lattice orders, exploiting the speed gaps in electronic and lattice motion, and gain insight into the mechanisms underlying the transformation. Such experiments would require variable polarization, resonant energy conditions (e.g. L edge of Ti, Mn, Cu), and spin-detection, in pump–probe experiments [54; 55].

One of the most extensively studied examples is the ultrafast (partial) demagnetization of ferromagnets by femtosecond laser pulses [52], where the initial observation on Ni has soon been extended to a broad range of other materials. The surprising aspect is the shortness of the quenching timescale, and the quest is still to explain how angular momentum is lost on this timescale.

Another interesting magnetic system with strong interplay among the electronic density, lattice structure, and spin interactions and potential applications is FeRh. This metallic alloy is particularly interesting because of a first-order phase transition from an antiferromagnetic to a ferromagnetic state happening at about 400 K [56]. It has been shown that changes in the electronic properties induced by a short laser pulse play a major role in triggering the first-order phase transition in FeRh [57]. More recent experiments at the MHz repetition rate FLASH FEL have allowed to observe a change from a antiferromagnetic to a ferromagnetic band structure within ~300 fs [58]. The experimental observations are supported by theoretical calculations. While this new information sheds new light on the nature of this order phase transition, the complete understanding will be realized when the changes in the electronic band structure are measured simultaneously with those of the atomic structure. This could be easily realized by simultaneously measuring photoemission of the valence band and photoelectron diffraction.

The soft X-ray photon energy range enables to access the details of the electronic structure of 3D materials, such as perovskites, and other transition metal oxides. These systems host many interesting physical properties, ranging from superconductivity to colossal magneto-resistance as well as many phase spin and metal-to-insulator transitions (MIT), which are poorly understood theoretically. One canonical transition is that observed in VO_2 [59]. This model transition represents a broad class of transformations in which an electronic phase change is accompanied by a lattice distortion (e.g. [60]). In these cases, the goal of time-resolved experiments is often twofold. The first goal is to uncover the mechanism of the photoinduced phase transition, which tends to be a complex multi-step process involving coherent displacive and incoherent disorder-driven dynamics [61]. The second goal aim is to identify the dominant interaction in the ground state and thus clarify its nature, e.g. whether it is dominated by electron–electron or electron–phonon interaction, as in a Mott or Peierls insulator, respectively [42]. Another well-known example is V_2O_3, the prototypical Mott insulator. At around 160 K, it undergoes a structural transformation from paramagnetic metal to antiferromagnetic insulator [62]. The reason the insulating state presents a frustrated antiferromagnetic ordering with a non-negligible contribution from orbital moment, rather than a conventional Neèl order, is still an open issue. Spectroscopic tools able to selectively probe specific orbitals and follow their time-evolution will allow to improve our understanding on this phenomenon.

Spectroscopic studies with soft X-rays have shown the interplay of the different degrees of freedom in the system and the important role of oxygen in the evolution of their properties [63]. Particularly interesting are materials hosting several concurring phase transitions, such as an MIT occurring at the same temperature as the appearance of magnetic moment ordering. In most of these materials (with

small band gap in the insulating phase), an impulsive laser excitation is enough to destroy the magnetic ordering. An interesting point to ascertain is how the electronic structure of the material is modified by the laser excitation and how the magnetic order parameter and the atomic structure are linked with such modification [64].

A central capability of complete time-resolved PES is to perform inherently synchronous photoelectron spectroscopy and diffraction measurements from the same sample region under identical excitation conditions. This enables simultaneous recording of the electronic, magnetic, chemical, and geometric structure, while they evolve interdependently, and it permits to temporally separate electronic, i.e. functional changes from lattice structural changes. Such unprecedented probing of dynamic structure–function relationships will contribute significantly to our mechanistic understanding of ordering phenomena and ultrafast phase transitions in materials.

The technical characteristics of SXP at SASE3 are well tailored to provide the experimental tools for a deeper understanding of electrons, spins, and lattice dynamics in physical systems with different phase transitions. Additionally, using a state-of-the-art delay-line detectors in combination with momentum microscopes provides us with a highly-efficient short-to-short detection scheme, which gives a possibility to fully utilize and accommodate a high number of FEL pulses, up to full bunch train at the maximum possible repetition rate of the European XFEL. The flexible laser setup, which is foreseen to provide the optical excitation, will also allow investigating the dynamics under a wide range of excitations.

2.1.3 Charge, spin, and heat flow at their fundamental dimensions and across interfaces in quantum materials

As introduced above, quantum materials are *solids with exotic physical properties, arising from the quantum mechanical properties of their constituent electrons* [19]. This broad class of materials includes strongly correlated, topological, spin, and 2D materials, as well as nanostructures and heterostructures made from these. Classical manifestations of electronic quantum effects in materials are ferromagnetism, ferroelectricity, and superconductivity. More *exotic* examples include quantum Hall effect, high-temperature superconductivity, colossal magneto-resistance, metal-insulator transitions, topologically protected states, and spin liquids and ices, as well as emergent electronic properties at heterojunctions and interfaces. All these intriguing phenomena directly result from a complex interplay of many-body interactions and various factors such as symmetry, topology, dimensionality, disorder, fluctuations, and confinement. A common characteristic is that the elementary excitations of quantum materials can be very different from the individual electrons

and atoms that constitute the material. In particular, the particle-like excitations can mimic and transcend the behaviours of the particles found in high-energy physics. Examples here are massless Dirac and Weyl fermions, Majorana fermions that are their own antiparticles, quasiparticles with fractional charge and statistics, and magnetic monopoles. Moreover, quantum materials with strong electronic correlations are often characterized by a delicate balance between competing or intertwined phases, so their properties are highly tunable by e.g. strain, doping, nanostructuring and heterostructuring, or electrostatic gating. Importantly, in quantum materials on the brink of instability, weak stimuli can cause anomalously strong responses. Quantum materials thus provide some of the most productive platforms for discovering fundamentally new physical phenomena and phases of matter, solving fundamental problems in physics, and realizing entirely new concepts and devices in energy and quantum information technologies (see e.g. [65; 66; 67; 68; 69]).

The study of the directed flows of charge, spin, heat, and the more exotic excitations of quantum materials, in response to electric and electromagnetic fields or thermal gradients, offers a rich scientific playground with close connection to applications.

Renowned examples are Mottronics, spintronics, and valleytronics:

- **Mottronics** aims at utilizing electronic correlation effects, specifically Mott-type metal-insulator transitions, for novel device functionalities and response characteristics. A concrete, envisioned device is the **MottFET**, a transistor that realizes high-speed, low-power, sub-thermal switching beyond the Boltzmann limit through voltage control of electronic phase change [70].

- **Spintronics** refers to the exploitation of electron spins in electronic devices, where pure spin motion avoids the heating associated with charge scattering. While spintronics has long focused on passing charge currents through ferromagnets, it has only recently been discovered that strong spin-orbit coupling in non-magnetic materials and topological insulators provides efficient ways of generating and converting spin currents [71; 72]. The underlying effects are the spin Hall effect and the spin-momentum locking in topological surface states, respectively.

- **Valleytronics**, finally, is a new class of transport phenomena that is based on the valley degree of freedom of semiconductor band structures [73]. Instead of spin polarization as in spintronics, the idea is to use valley polarization for information storage and processing, i.e. to localize electrons in inequivalent conduction-band valleys in energy-momentum space. Electrons residing in these valleys e.g. experience opposite effective magnetic fields and will therefore move in opposite

directions under electrical bias [74].

A common trait of all three examples is that the functionality in device-like structures is typically studied by electrical bulk transport measurements only, which cannot provide mechanistic insights. The detection and control of nanoscale currents of charges, spins, valley polarizations, or collective excitations is a grand challenge that requires novel advanced characterization techniques.

Complete time-resolved PES will enable us to look into device-like structures and real devices made from novel materials, while they operate, and probe interfacial electronic structure changes under gate bias as well as the fundamental dynamics of electron and spin populations in energy-momentum space and the charge-state response at atomic sites. Exploiting bulk and interface sensitivity, spin resolution, and polarization control, we will be able to track ballistic and drift-diffusion charge currents across interfaces as well as spin- and valley-polarized currents, reveal the accumulation of spins and valley polarization at surfaces and interfaces, directly observe spin and valley Hall effects, and also follow the propagation of elementary excitations such as phonons (heat) or excitons and their transfer across interfaces.

2.1.4 Qualitative creation, probing, and control of new quantum states

Beyond a new view on thermally accessible phases and phase transitions, time-resolved pump–probe methods offer the unique opportunity to create and study new phases of matter under non-equilibrium conditions by driving materials at their characteristic low-energy scales or by inducing light–matter mixed states. Selective excitation of specific collective modes and electronic resonances permits us to selectively and coherently manipulate lattice and electronic structures and induce new states and phenomena that do not exist in equilibrium. A specific and intriguing example is light-induced superconductivity. In recent experimental demonstrations on cuprates and the molecular solid K_3C_{60}, intense mid-infrared pulses were used to resonantly drive large-amplitude oscillations of selected lattice vibrational modes, resulting in the transient emergence of superconducting-like states in a non-superconducting system or at temperatures far above the equilibrium superconducting transition temperature [75; 76; 77]. These remarkable observations have been associated with the suppression of a competing charge-ordered state, the redistribution of coherence in interlayer coupling, or the modulation and enhancement of the Cooper pairing strength, respectively. But a detailed understanding of how long-range quantum coherence is established in these experiments is still lacking. The approach and problem readily extend to the light-induced enhancement and

creation of other forms of electronic order, such as charge- and spin-density waves or Mott insulators.

Another rapidly growing field in which ultrashort light pulses are used to engineer novel quantum phases is light-induced topology. In pioneering experiments, it was demonstrated that short-pulsed excitation of a topological insulator with a photon energy lower than the bulk band gap can imprint the coherence of the light field on the Dirac surface states, resulting in the formation of hybrid photon–electron states, so-called Floquet states [78; 79]. It was also shown how the Floquet band structure, specifically its Dirac crossings, can be manipulated in a highly controlled fashion using circularly polarized pump pulses. In the meantime, various time-dependent protocols for inducing topological phenomena by tailored light pulses have been predicted and are pending experimental verification. These include the transformation of conventional materials into topological insulators and chiral spin liquids, the switching between topological insulator and (Dirac and Weyl) semimetal states, and the creation of topologically protected edge states and quantum Hall phases without external magnetic field. In a recent representative first experiment along these lines, THz pulses have been used to drive a large-amplitude shear lattice deformation in a Weyl semimetal, switching the system to a topologically distinct transient phase with higher symmetry, albeit without a direct proof of the topological changes in the electronic structure [80].

Direct information on the transient electronic structure is crucial for the design of a desired state of quantum matter and to prove its existence. Complete time-resolved PES is therefore the primary tool for the discovery, understanding, and manipulation of new transient electronic phases of quantum materials. The technique is sensitive to the defining electronic signatures, such as superconducting gaps and topological states and their spin textures, as well as Floquet states, and it is sensitive to the bulk and surface electronic structure that is so intimately linked in topological materials. Complete time-resolved PES can follow how transient states emerge and disappear directly in the electronic structure and in the population of electronic states, it can track the relaxation of energy and coherence, and it can correlate the electronic structure dynamics with simultaneous changes in the lattice structure. The method thus provides a comprehensive view of the transitions from *conventional* equilibrium phases to new non-equilibrium states and of the dynamic properties of these new states. A key experimental requirement, however, is to have available fully tunable ultrashort excitation (pump) pulses across a broad spectral range. From the probe side the extended energy available SXP, reaching up to tender X-rays, would allow studying the surface versus bulk dynamics. It will also allow extending the technique to the study of buried interfaces, heterostructures, and devices. The implementation of SW-PES, whenever possible, will greatly contribute to the understanding of these

systems.

2.1.5 Multiple electronic excitations in 2D and 3D electron systems

Most measured photoemission spectra consist of quasi-particle peaks and additional structures, often called satellites. They correspond to multiple electronic or lattice excitations due to interactions, including e.g. a collective response of the electron gas to the creation of a hole (missing electron). Their characteristic energy and intensity are strongly related to charge dynamics. They have been understood with simple models of electron–boson coupling, which predict that these structures disperse in energy like replica of the valence bands. Well-studied cases include plasmon satellites in bulk Si, Graphite, Na, and Al [81; 82; 83; 84].

When the dimension of a system is lowered, screening is weaker and effective interactions stronger. Therefore, low-dimensional systems are particularly interesting for the study of phenomena that can only be explained by interaction effects, such as satellites.

Two-dimensional electron gases (2DEGs) are at the basis of current nanoelectronics because of their exceptional mobilities. They have been clearly identified at surfaces and interfaces of several materials and combine fundamental interest with established technological applications to field effect transistors (FETs) with high-κ dielectric gates, van der Waals heterostructures, and metallic interfaces between insulating oxides.

A high-quality 2D electron gas has been measured in a few-layer InSe encapsulated in hexagonal boron nitride under an inert atmosphere. The dynamics of hot carriers can be monitored by means of two-photon photoelectron spectroscopy [85]. In similar systems, the bandgap in few-layer black phosphorus, doped with potassium, can be widely tuned by using an in-situ surface doping technique [86]. The 2D electron gas observed at the $LaAlO_3/SrTiO_3$ interface exhibits simultaneous ferromagnetism and superconductivity [87]. Furthermore, Polarons at this interface [88] and on the surface of $SrTiO_3$ [89] have been also observed. In both systems, the electron density can be controlled by oxygen vacancies [90; 91] and, therefore, also the electron-lattice interactions and the polarons.

Theoretical prediction of satellites in bulk systems are well reproducing the measured lineshapes and shading light on the multiple excitations as well as on the photoemission process itself. Less is known in 2D materials, besides studies on graphene that have been subject to ongoing discussions [92]. Open questions include the dependence of satellite position, shape and intensity on the initial density and the

time-dependent density of carriers after excitation, the strength of intrinsic satellites in lower dimensions, or an effect of the substrate.

Photoemission experiments at the Soft X-Ray Port (SXP) at SASE3 are well-suited for a better description and a deeper understanding of multiple electronic excitations. The high repetition rate makes photoelectron spectroscopy experiments meaningful by giving access to an acceptable signal-to-noise ratio. The soft X-ray photons, by increasing the electron mean-free path, give access to 2DEGs electronic structure at buried interfaces. Thanks to these tools, pump–probe experiments performed with the European XFEL short timescale would give a complete description of electron dynamics after laser excitations. The laser-induced modification of the local charge distribution will induce predictable modifications in the satellite (plasmon, polarons, etc.) structure.

2.1.6 Low-dimensional silicon systems

Low-dimensional nanomaterials development represents one of the main routes in modern technology. The reduction of dimensionality often results in new exotic properties, like topological protected phases or increased spin-orbit effects based on quantum size effects. One system of particular interest is the case of silicon (Si) low-dimensional nanomaterials. They would allow realizing nanoelectronics compatible with the existing silicon microelectronic technology. Numerous systems have been realized to date with different dimensionality: 2D silicene [93], 1D silicon nanotubes [94] and nanowires [95], silicon nanorods [96], silicon nanoribbons (SNR) [97], and finally Si quantum dots [98]. Applications of the realized structures can be foreseen, either based on their intrinsic electronic properties or by using them as one of the building blocks in heterostructures. In the latter case, it has been shown that SNR can be used as a template to realize 1D Co or Mn structures that can be used to investigate magnetism in low dimensional nanostructures as well as opening new avenues to realize nanometric devices for spintronic applications [99]. Moreover, SNRs on their own have been used to realized FET biosensors for organic molecules with applications in life science and diagnosis [100]. They have also been used to develop multiplexed pH measurements [101].

The lowest dimensionality systems, from the quantum dot to multilayers of 1D nanoribbons, have been best realized via bottom-up approaches using metallic surfaces as templates. These systems have been shown to grow nicely on the (110) surface termination of metallic surfaces: Ag, Au, Pt, or Al. All these surfaces have a tendency to stabilize with a missing row reconstruction that serves as a template for the growth of the Si nanostructures. The best template found so far is Ag(110) [102].

This surface does not exhibit a missing row spontaneously, but it develops it upon deposition of adsorbates, like Si. A variety of different Si nanostructures has been realized on Ag(110) using a bottom-up approach and classical surface preparation methods in ultrahigh vacuum conditions. The characterization of the synthesized structures is done using a combination of surface techniques: LEED, Auger, XPS, ARPES, and STM. Moreover, STM has also been used to manipulate the nanoribbons and measure their transport properties [103].

XPS measurements of the Si 2*p* core level have been decisive to understand the structure of Si nanoribbons. In combination with STM and theoretical DFT calculations, it has been shown that the Si nanoribbons arrange in a pentagonal configuration. This is so far their most outstanding property [104]. One reason is that pentagonal Si motifs are hardly found in nature. On the other hand, the pentagonal arrangement may explain why the realization of silicene, the Si analogue of graphene, has been so elusive. Furthermore, pentagonal structures, like penta-graphene, have been proposed as structures with outstanding properties competing with that of graphene.

This application concentrates on the use of TR-XPES to investigate low-dimensional systems made out of Si or where Si is one of the building blocks. Time-resolved soft X-ray XPS and XPD will be used as a new tool to help in the cumbersome problem of solving Si nanostructures. Furthermore, the technique will be used to understand the interaction mechanism with biomolecules like carcinoembryonic antigen solutions, in view of improving the biosensor technology. The study of low dimensional structures of 3*d* transition metals (Cr, Co and Mn) based on SNRs with femtosecond resolution will be of paramount importance to understand the interplay between magnetism and structure in these system. The properties of the transient induced states will allow testing the use of these materials in ultrafast spintronics applications.

2.1.7 Probe and manipulation of topological phases

Magnetic topological insulators permit the observation of the quantum anomalous Hall effect with topologically protected lossless edge states [105]. These promise applications in charge-based electronics as lossless interconnects and in spintronics as spin-polarized edge states that can form networks around magnetic domains, and for spin-charge conversion. At interfaces with superconductors, chiral Majorana fermions occur that are envisioned for braiding operations in qubits [105]. The focus is recently moving from established randomly substituted impurity systems with Cr and V in $(Bi,Sb)_2Te_3$ to intrinsic stoichiometric topological insulators, such as $MnBi_2Te_4$ as bulk compound [106] or $MnBi_2Te_4/Bi_2Te_3$ heterostructures [107]. These made the long

sought magnetic gap and the expected out-of-plane (hedgehog) spin texture of the Dirac cone accessible by ARPES [107]. The phase diagram of these systems is very rich and comprises ferromagnetic and antiferromagnetic topological insulators as well as magnetic Weyl semimetal phases, often separated by very small differences in total energy.

The spin-charge conversion is an important application of magnetic and nonmagnetic topological insulators in spintronics. Pump–probe spin-resolved ARPES experiments can be designed to directly detect spin-charge conversion at interfaces, making also use of the enhanced probing depth of soft X-rays. A peculiarity of magnetic topological insulators is that a reversed magnetization corresponds to a different topological phase and, correspondingly, a magnetization reversal goes along with a topological phase transition. Furthermore, in trilayer structures comprising two coupled magnetic topological insulators, the relative orientation of the magnetization decides between an anomalous quantum Hall insulator and an axion insulator that allows switching the topologically protected edge states on and off. Pump–probe ARPES can explore the conditions for such switching by optical means where, among others, the role of bulk versus surface transitions needs to be investigated. In this way, infrared pump pulses could drive topological phase transitions. It is not clear how this will change with magnetic topological insulators above the Curie temperature, which is currently less than 15 K and is expected to rise with different compositions and/or magnetic proximity effects.

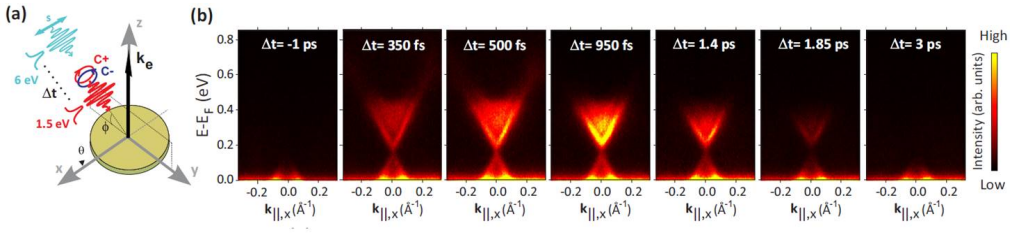

Figure 2.3: Ultrafast dynamics of Dirac fermions in a topological insulator (from [108]). (a) Experimental geometry. (b) Time-resolved ARPES with circularly polarized light.

For nonmagnetic topological insulators, pump–probe spin-resolved ARPES can be used not only to probe the influence of spin-forbidden transitions in the decay of excited electrons [109] but also to control the spin texture in the excited state via circularly polarized pump pulses [109]. It is not clear how this polarization will interact with a ferromagnetic spin texture and whether it will facilitate magnetic switching. At high fluences of circularly polarized infrared light, a magnetic gap is expected and has been reported at the Dirac point for Bi_2Se_3 [110]. An observation of the expected hedgehog spin texture and its decay in the time domain would give valuable insights into transient topological magnetic states. This requires a highly

efficient detection scheme for complex spin textures. Of particular interest in this context is the relation between the transient spin splitting of bulk bands and the timescale of ultrafast demagnetization, along with the ability to control the efficiency of the microscopic processes that would allow switching on and off the hedgehog spin texture in the time domain. Circularly polarized infrared light has been reported to generate spin-polarized currents at the surface of topological insulators [110]. However, in time-resolved ARPES (Figure 2.3 on the preceding page), it is not clear so far whether such unidirectional currents observed in the Dirac cone [108; 111] cancel out completely when all directions in momentum space are considered [111].

Another example of topological phase transitions that are likely to be driven by optical excitations is found in topological crystalline insulators. These are protected by specific crystal symmetries and display an even number of Dirac cones in the Brillouin zone. These occur consequently away from the zone centre, which requires larger photon energies to provide the necessary electron momentum. When $Pb_{1-x}Sn_xSe(111)$ is doped with small amounts of Bi, a topological phase transition occurs to a state with an odd number of gapless Dirac cones, bringing it into the same topological class as Bi_2Se_3 [112]. It is believed that this is due to a ferroelectric distortion and could be driven by laser excitation. Finally, if these materials are magnetically doped, they will follow other constraints concerning the magnetic anisotropy and permit different topological phases and spin textures [105]. A study of varying pump energy, fluence, photon energy, helicity, charge doping, and magnetic doping of these phenomena will give insights into fundamental phenomena and pave the way for future applications in spintronics and quantum computing.

2.1.8 Transient electronic states for quantum computation with topological matter

De-coherence represents a major obstacle along the path towards the fabrication of scalable quantum computers. Topological quantum computation may provide an elegant way around the problem of de-coherence. The idea is that one can encode by optical means non-local quantum information in the surface and/or interface states of hetero-structures consisting of topological materials. These transiently populated states display three distinctive properties at once: they are topologically protected against corruption by the environment; they present lifetimes exceeding 10 ps [113] and reaching several microseconds in specific materials [114]; and their spin character can be defined by selective excitation of one of the spin-polarized branches of the Dirac cone, even with linearly polarized light [115]. Therefore, the optical control of the surface and interface currents of topological matter opens novel perspectives for opto-spintronic applications and will be another fundamental ingredient within the

general concept of all-optical switching. The unique combination of the European XFEL source and the spin-resolving ToF k-microscope is suitable to shed light on the dynamical processes occurring in hetero-structures consisting of topological materials. The extended photon energy range of the European XFEL can be used to probe their electronic states by time-resolved photoemission spectroscopy at variable depths, thus providing information from the surface as well as from buried interfaces. The ultrashort pulses allow to determine the characteristic timescales of the transient population and de-population of the topological states upon laser excitation, also as a function of the polarization of the pump and probe pulses. Finally, tiny details of the electronic structure, such as the coupling of spin-polarized surface and interface states with bulk bands, will be pointed out thanks to the time-, energy-, spin-, and momentum-resolved capabilities and the highest detection efficiency of the momentum microscope.

2.1.9 Ultrafast dynamics of topologically protected magnetic nanostructures

Time-resolved magnetic imaging using XPEEM has been mostly focused to processes occurring in the GHz regime, such as spin precession, domain wall motion, and magnetization reversal. The technique has found applications in studies on spin-torque–induced domain wall motion in racetrack magnetic memory design [116]. Topologically protected domain structures, such as skyrmions, recently observed in static measurements at room temperature and zero field [117], are also at the centre of current scientific attention. Another synchrotron-based microscopy, namely STXM, demonstrated that dynamic excitations in skyrmions are controlled by the spin–orbit torque and occur on the nanosecond timescale [118]. Pump–probe imaging (Figure 2.4 on the next page) also revealed the theoretically predicted “Skyrmion Hall effect”, in which current-driven skyrmions acquire a transverse velocity [119]. Whereas domain wall motion takes place at around the nanosecond timescale, ultrafast spin dynamics require femtosecond resolution and thus remain out of reach at synchrotrons.

Indeed, recent studies at FEL sources revealed spin switching and magnetization/demagnetization down to the femtosecond regime [120; 121; 122]. Similarly, laser-induced generation of skyrmion bubbles, demonstrated in ultrathin ferromagnetic layers [123], and laser induced skyrmion nucleation observed with soft X-ray scattering at the SCS experiment of the European XFEL [124], are interesting subjects for ultrafast microscopy studies using optical excitations. Moreover, implementing skyrmions in antiferromagnetic/ferrimagnetic alloys, a very recent topic of interest, promises yet another route in dynamic microscopy studies,

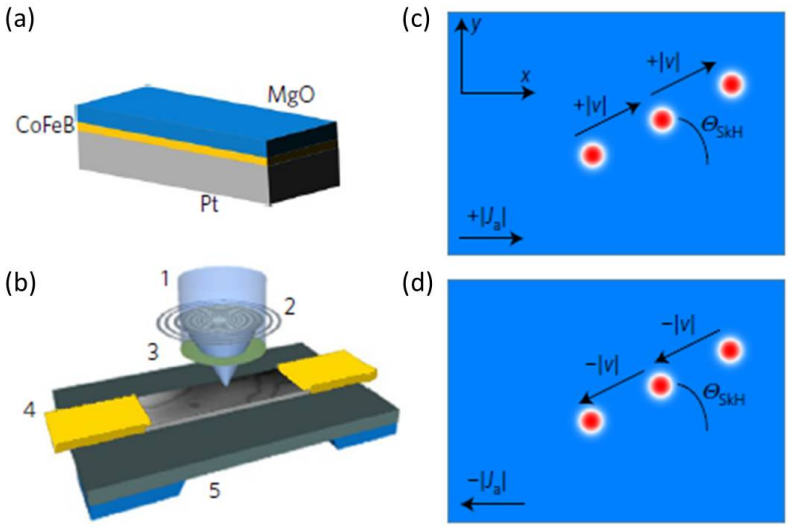

Figure 2.4: Schematic of the technique to measure Skyrmion Hall effect [119]. (a) Scheme of the multilayer sample. (b) Scheme of the measurement setup using a nano X-ray beam passing through the sample. (c, d) Movement of Skyrmions after excitation with an alternating current. The ultrafast dynamics is not accessible due to the limited time resolution of synchrotrons.

as antiferromagnets are in general expected to display faster dynamics compared to their ferromagnetic counterparts [125]. Clearly, in aiming at understanding dynamic phenomena in these and similar systems, the combination of PEEM with FELs may provide a unique investigation tool. Momentum microscopes will allow performing these experiments when used in spatially resolved mode.

2.1.10 Charge transfer processes at organic interfaces and in solar cells

Singlet fission (SF) is a photophysical process in which an optically excited singlet exciton (S1) in an organic chromophore is converted into two triplet excitons (T1). The advantage of such process is that, with one photon, two excited electrons can be generated and, by an appropriate choice of light-harvesting materials, a solar cell efficiency of 44.4 % can theoretically be achieved [126]. In the last decade, several SF organic chromophores, such as polyacenes (tetracene, pentacene, hexacene) or isolated polymers (poly- or oligoenes) have been studied by combined experimental and theoretical approaches [127; 128], but there is no consensus on the fundamental description of SF to date [129; 130].

The decay dynamics of triplets formed by singlet fission in pentacene thick films have been recently studied at the Elettra synchrotron by means of time-resolved

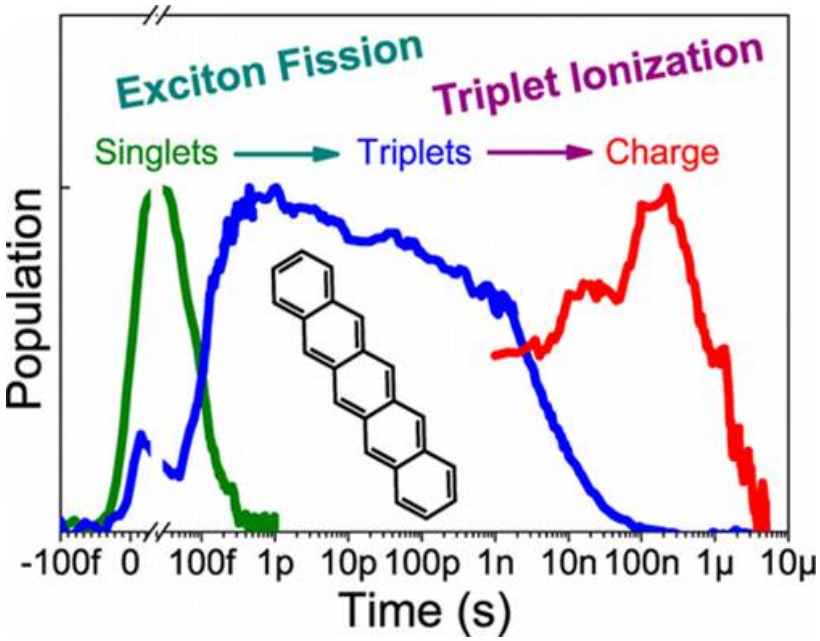

Figure 2.5: Exciton dynamics in pentancene as a function of delay time. The population of the different excited states between the femtosecond and the microsecond timescales is displayed.

carbon K-edge XAS [131]. For the first time, the Carbon K-edge XAS spectrum of the molecules in the triplet state was measured. However, the 100 ps pulse length available at the synchrotron did not allow to monitor the fission process that takes place in less than 100 fs. At the European XFEL, by exploiting the fs pulse duration, the full study of the fission process could be accomplished. In particular, the satellite structures in C 1*s* photoemission of pentacene in a pump–probe experiment could be measured. Satellites in core level photoemission are a consequence of the relaxation of the electronic system following a core-hole formation. The shake-up satellites, which are observed on the higher binding energy side of the main photoemission line, can be explained in a simplified picture as additional valence excitations accompanying the core ionization event. A time-dependent study of the satellite spectra will provide information on the reorganization of the molecular electronic system. We expect intensity changes in such distributions due to the dark states that have been populated by the pump pulse.

2.1.11 Time-domain in-situ X-ray studies of interfacial charge transfer

At the heart of many emerging energy harvesting concepts are interfacial processes that require an optimized, concerted generation and flow of charge on the molecular level or across interfaces. Energy harvesting includes both direct photovoltaic light

to charge conversion as well as photochemical reactions such as the splitting of water or “sunlight to fuel” applications. Processes evolving on spatial and temporal scales spanning orders of magnitudes have to be connected to gain a comprehensive understanding of the fundamental dynamics and processes in order to optimize the molecular, interfacial, and macroscopic charge and energy transport. Femtosecond TR-XPES is particularly well-suited to monitor electronic and chemical states of matter with the elemental site-specificity and chemical sensitivity that is required to test and improve our fundamental understanding of interfacial chemistry and photophysics in complex systems. Self-assembled donor-acceptor nanostructures based on organic molecules are one example of photoactive materials that continue to inspire high hopes for cheap, sustainable energy solutions. Organic chemistry offers a huge amount of molecules or compounds to choose from in order to design a system tailored to the specific application. Preferential conductivity for electrons or holes in organic electronics is usually achieved by mixing molecular compounds with different electronic functionalities. The charge transfer process between the (typically organic) chromophore and the electron acceptor is central to understand and control the functionality of organic photoreceptor systems. This applies to organic photovoltaics, organic photoconductors, and even photosynthesis in biological systems.

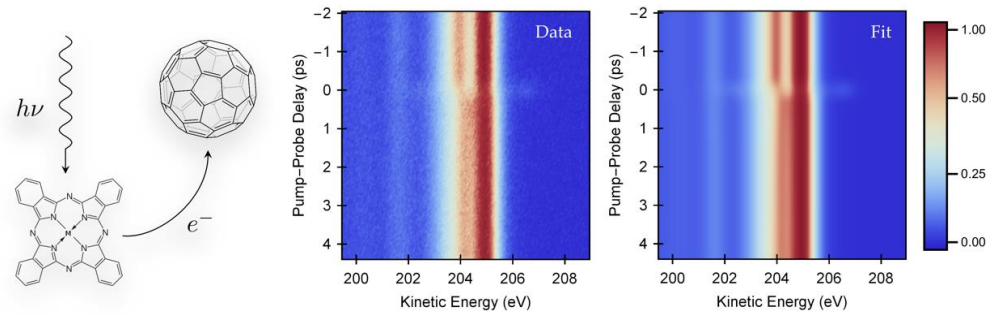

Figure 2.6: Measured femtosecond time-resolved C 1*s* XPS spectra of the CuPc-C60 heterojunction as a function of time delay (vertical) and kinetic energy (horizontal) as well as the result of a global fit procedure that decomposes the heterojunction spectra into contributions associated with the two separate components CuPc and C60

Recently, we established the first femtosecond tr-XPS measurement of charge transfer dynamics in a CuPc/C60 bi-layer system using FLASH at DESY. TR-XPES offers the unique opportunity to investigate the dynamics underlying the charge transfer process with exquisite site-specificity by monitoring the time-resolved C 1*s* XPS from the CuPc/C60 system following optical excitation of the chromophore (Pc). We observe an energy-shifted C 1*s* XPS line of the C60 electron acceptor after optical excitation, which can be seen as a direct indicator for the electron transfer to the C60 (cf. Figure 2.6). A previously unobserved channel for exciton dissociation into mobile charge carried is identified, providing real time characterization of the time

scale and efficiency of charge generation from lower-energy charge transfer in an organic heterojunction. These results open new options for light harvesting in organic heterojunctions [40].

2.1.12 Ultrafast photoemission spectroscopy study of nanostructured systems: Inorganic nanoparticles embedded into an organic matrix

Nowadays, when information technology has become an important part of our lives and the complexity of the mobile gadgets increases, attention is paid to more efficient and faster memory structures. Super miniaturization with extremely small bit cell size from microscale to nanoscale and data storage become important issues. There are tremendous worldwide efforts to develop new memory devices for long-term storage of information [132; 133; 134]. The new kind of memory based on switchable resistive materials is commonly ranked as resistive random-access memory (RRAM). Hybrid systems, mainly consisting of inorganic nanoparticles (NP) blended into an organic matrix, have been proposed as one type of RRAM [135; 136; 137; 138]. Possible memory architecture is obtained if an organic thin film containing inorganic nanoparticles is sandwiched between the “cross-point” arrays of electrodes that consist of narrow metal stripes, running in perpendicular directions above and below the film, as sketched in Figure 2.7(a). When a threshold voltage, suitable to write or erase, is overcome the device switches from a high-impedance state to a low-impedance state and remains in that state even when the power is off. The changes in resistivity in the high and low conductivity state can differ by 6–8 orders of magnitude [139; 140], thus allowing to define the “1” and “0” states required to realize a digital memory.

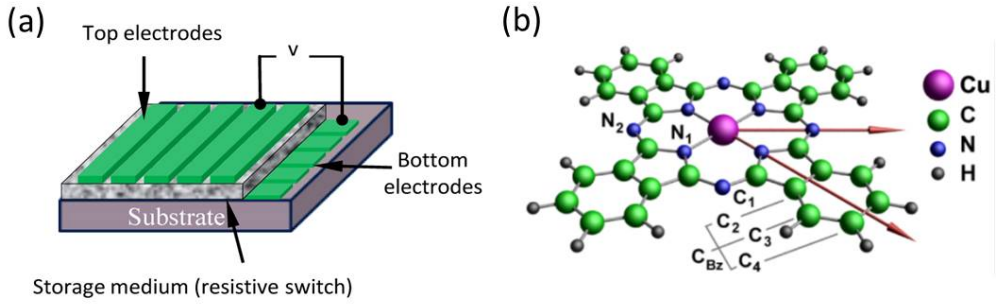

Figure 2.7: (a) Scheme of a crosspoint memory architecture. (b) Representation of the molecular structure of the CoPc molecule.

Despite the rapid development in this area many questions are still unanswered [141; 137], the most relevant one being the large resistivity difference between the high

and low conductivity states. The most fertile model to explain these differences is based on charge accumulation on the NP, which leads to strong modifications of the properties of the organic matrix material [140]. Charge accumulation depends on the specific electron structure and interface interactions between the NPs and the thin organic film matrix. It has been postulated to occur whenever the NP energy levels lie within the energy gap of the organic molecules [133; 134]. However, this assumption has to be confirmed experimentally.

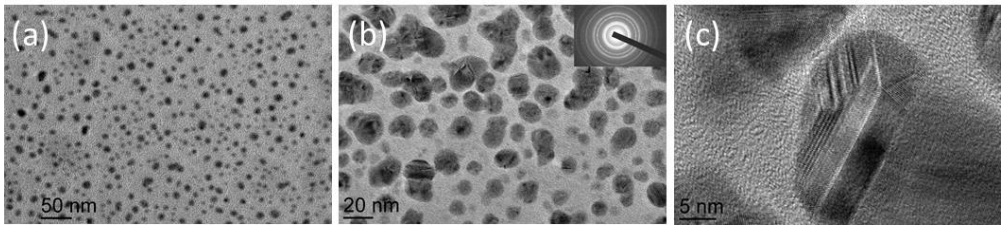

Figure 2.8: Microstructure of nanocomposite thin films made of Ag nanoparticles embedded in a matrix of CuPc. The TEM pictures show: (a) Structure after 0.4 nm Ag deposition with 50 nm resolution. (b,c) Display the nanostructures after 5.7 nm Ag deposition with 20 nm and 5 nm, respectively.

One study case to understand charge accumulation is that of Ag NPs embedded in a CuPc organic film. The molecule, schematically shown in Figure 2.7(b), has a planar structure with D_{4h} point symmetry and it consists of a central Cu atom surrounded by four nitrogen atoms–pyrrole (N_1); four other nitrogen atoms–bridging aza (N_2); 32 carbon atoms–pyrrole (C_1); and the benzene ones (C_2, C_3 and C_4). Figure 2.8 shows some results of silver deposition on the outer surface of the organic film. Due to surface and bulk diffusion of deposited Ag atoms, the embedded silver nanoparticles were self-assembled, forming a 3D Ag NP distribution in the bulk of the organic semiconductor. The size, concentration, size distribution, and shape of the resulting nanoparticles were studied using transmission electron microscopy (TEM) JEOL JEM-2100 operated at 200 kV. Therefore, the microstructure and evolution of the morphology of the nanocomposite films as a function of nominal silver coverage can be studied on atomic and nanoscale levels.

In order to understand the mechanism of charge accumulation in this and similar compounds, *in operando* time-resolved XPS studies will be performed during excitation with voltages and/or optical and THz laser pulses. The evolution of the core levels as a function of the time delay between pump and pulse will make it possible to understand the dynamic modifications at the interface between NPs and the organic matrix as well as the energy level alignment and electronic structure of the system. The energy range and time resolution available at SXP will give unique opportunities to associate the contributions of different atomic sites (bulk, steps, twines, facets,

corners) of the highly ordered nanoclusters (Figure 2.8 on the facing page) to the CL spectra and electronic DOS. In other words, we will achieve a qualitative assignment of different features of VB and CL structures. Similar studies should be done for the organic matrix: to associate the contributions of different atomic species as well as sites of the organic molecules to the electronic DOS and CL spectra. The studies will also provide information on the diffusion dynamics and/or cluster formation of inorganic spices in organic matrix. Furthermore, they will make it possible to understand the chemical reactions between deposited spices and/or clusters and organic matrix by means of watching particular sites of clusters (steps, corners, etc.) and specific atoms and sites of organic molecules taking place in the reaction. We believe that such measurements will elucidate the mechanism of realization of non-volatile electrical memory. The use of optical and THz excitations may open new routes to operate these devices.

2.1.13 Spin-resolved and ultrafast photoemission spectroscopy study of single molecular magnets

Recently, single molecular magnets (SMM) have attracted huge interest because of their spectacular magnetic properties. The theoretical and experimental communities pay enormous attention to the fascinating possibility to control the magnetic states of the molecules through manipulation of the spin of the electrons via applied current or magnetic field. High chemical stability, spin degree of freedom, and the advantages of nanosized systems make them promising materials for high-density storage elements or for future electronics with higher and new performance or functionality. Of paramount importance for the utilization of the spin degree of freedom of SMM is a clear understanding of how spin-dynamical processes influence the structure and reconfiguration on the magnetic state, etc.

Among all molecular magnets, we concentrate our attention on two classes of complexes. The first includes spin-crossover (SCO) systems [142] containing a ligand part and transition metal ion/ions that can be switched between a low-spin (LS) and a high-spin (HS) states by external influence like temperature, light, pressure, magnetic or electric fields, or charge flow [143; 144; 145; 146; 147; 148; 149]. The SCO properties are related to coexistence of both spin states close in energy and to conformational stabilization of one of the spin states during the LS–HS transition. For example, an LS (S=0) to HS (S=2) transition [150] occurs in Fe-phen molecule [142] (Fe(1,10-phenanthroline)$_2$(NCS)$_2$) at high temperature. It leads to a change in the Fe-N bond distances and angles [10], resulting to a reduction in the ligand fields around the Fe site. The second class of systems contains magnetic molecules with high-spin magnetic configuration in the ground state. Star-shaped

molecules [151; 152], polyoxometaletes [153], cubates [154], or other molecules like manganese-12-acetate [155] belong to this category. These SMM are interesting because of the possibility to reverse the total spin from S to -S. Molecular magnets from both classes can drastically change the magnetization, electronic structure, and conformation. Performing TR-XPES experiments at the European XFEL will contribute to the understanding of the dynamical changes in magnetization, electronic structure, and conformation of molecular magnets upon selective excitation in view of develop new spintronic devices.

2.1.14 Orbital tomography

Understanding and control of photon-induced dynamics of molecules on solid surfaces, including charge transfer and ultrafast atomic dynamics, are of essential importance for surface chemistry but also for novel devices. In the last decade, the so-called orbital tomography technique has emerged as an exciting tool for imaging localized electronic wave functions of molecules in thin films [156; 157]. Two decades ago, it was realized that the excited photoelectron of molecular systems can be well approximated by the independent atomic center (IAC) approximation [158]. This allows interpreting the measured angle-resolved photoelectron signal as the density distribution of individual molecular orbitals. The initial state is determined by a DFT-calculated orbital of an isolated molecule. The final state is constructed from a coherent superposition of partial final states at each atomic site with spherical Bessel functions and by considering the inelastic damping and phase shift from the potential of the emitting atom [159]. Recently, this technique was propelled into the time domain by exploring ultrafast processes of excited wave packets and charge transfer dynamics in molecular thin films [160]. In combination with X-ray photoelectron diffraction (XPD), a well-established technique for obtaining local structural information of adsorbed atoms or molecules on surfaces [161; 162; 163; 164], one can directly correlate the electronic response with the nuclear dynamics upon excitation. Such a combined experiment will significantly advance the understanding of the dynamic evolution of electronic and structural interplay.

2.1.15 Surface chemistry and catalysis

The investigation of surface chemistry and catalysis using photoemission has been one of the central topic of the technique since its origins. The potentiality has been largely extended thank to the development of the NAPP technique allowing to study in-operando systems in realistic conditions. The ultimate understanding of chemical reactions and catalytic processes rely strongly on the successful implementation of

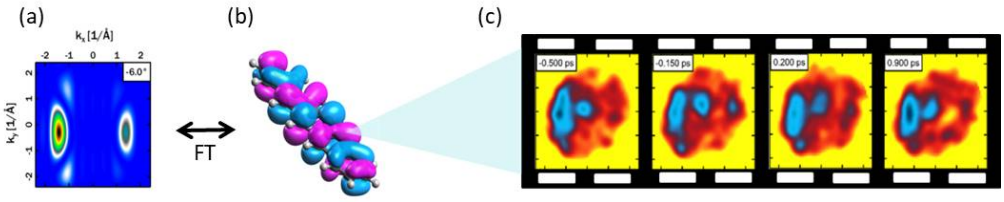

Figure 2.9: (a) Calculated photoelectron momentum maps of a LUMO orbital. (b) Real space DFT-calculated LUMO orbital of pentacene. (c) Measured time-dependent photoelectron momentum map of LUMO. The dynamic evolution in photoemission intensity for pump–probe delays. The observed distortion and complicated dynamics of the wavepacket can be explained in the framework of energy transfer between neighbouring molecules and between molecule and substrate.

time-resolved photoemission experiments. FELs are currently the ideal tool since they allow extending the energy range of the HHG sources into the soft X-ray regime and therefore the realization of XPS and XPD experiments.

In last years, a few time-resolved core level PES experiments on surface adsorbates have been performed at FELs to study their feasibility. In a TR-XPES experiment at FLASH, photo-induced changes in the top-most layer of an iridium single crystal were successfully measured. The surface core level shift of 550 meV of the Ir 4*f* levels allowed to distinguish between photo-induced changes of the bulk and surface core level. It was observed that the photo-induced change in the local charge distribution around the iridium atoms induced by an 800 nm laser pulse is concentrated in the surface layer, while the bulk signal shows no significant changes. At LCLS, a feasibility study of time-resolved core-level PES for femto-chemistry experiments has been performed [38]. Strong effects on the measured core level lines due to vacuum space charge effects caused by the 400 nm, 10 Hz pump employed for activating absorbed oxygen on Ru(0001) sample were observed and modelled. Such pump conditions necessary to have a good yield of the reactions are the ones employed for the catalysis experiments at LCLS [165]. They cause strong effects that obscure the chemical shifts due to the reaction, showing that different excitations are necessary to perform this class of experiments. One option could be to tune the pump to near- or mid-infrared, where only less likely multi-photon processes can cause emission of photoelectrons or to use THz radiation, which has been shown to be able to trigger reactions [166].

Recent developments of the TR-PES at FLASH, the increased understanding of space charge effects and the use of third harmonic photon energies, have paved the way to study catalytic reactions with femtosecond resolution. One of the first examples has been focussed in the efficient degradation of pollutants [39]. In particular, the

reaction dynamics of the photooxidation of CO on the anatase TiO_2(101) surface, an important reaction for air purification. Time-resolved XPS with soft X-ray photon probe pulses, hν= 647.9 eV has been used to understand the photooxidation with hν= 1.6 eV near infrared pulses. The experiments have shown that the oxidation to form CO_2 from CO and O_2 precursors at $3{\cdot}10^{-7}$ mbar takes place between 1.2 and 2.8 (± 0.2) ps after irradiation with no intermediate species. Theoretical calculations predict the formation of intragap unoccupied O_2 levels after irradiation which lead to the formation of a charge-transfer complex. The subsequent oxidation is realized via a mechanism involving the direct transfer of electrons from TiO_2 to physisorbed O_2.

Another research field of high interest in this domain is the investigation of electron dynamics of light harvesting systems. The need to reduce CO_2 emissions is driving the search for efficient alternative energy sources, with solar power being an attractive option. Despite spectacular advances in efficiency through materials development, further improvements are necessary to provide sustainable solutions. A key to achieving this goal is measurement of the element and state specific carrier dynamics on the femtosecond timescale. Together with the results of experiments to monitor bond-breaking and bond-making in photocatalysis, this will provide design criteria for new materials.

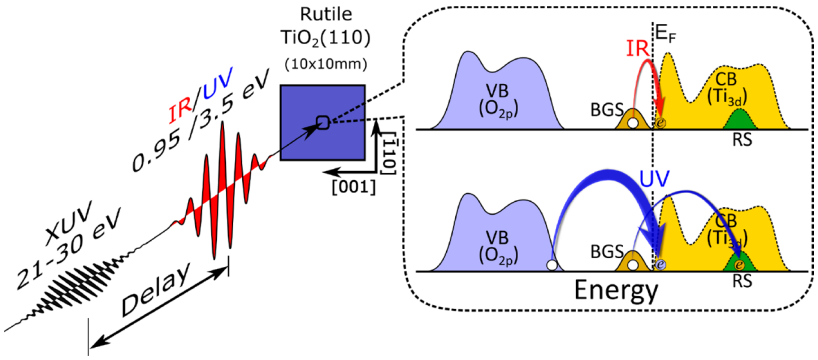

Figure 2.10: Scattering geometry of the pump–probe experiments, with light incident at 45° to the surface normal in the [001] azimuth. The pump electric field of the incident light is parallel to the [1̄10] azimuth. The dashed box shows the excitation routes for IR- and UV-pumped experiments. IR can excite electrons from the band-gap states (BGSs) to the bottom of the conduction band (CB), whereas UV can excite electrons both from the BGS to a resonance state (RS) in the CB (small arrow) and from the valence band (VB) to the CB (large arrow)

Recent feasibility studies of TR-PES using conventional lasers on light harvesting systems have been successfully conducted in a variety of systems: TiO_2 [167] (see 2.10), dye-sensitized metal oxides [168], and hybrid perovskites [169]. They provide state-selective measures of recombination dynamics following excitation with visible or UV excitation. Furthermore, this work has provided valuable insights into the photophysics of several energy dissipation processes, although it has so

far been restricted to low binding energy states. The highest probe photon energy used in this work is 30 eV [167]. Measurements in the soft X-ray region using SXP at SASE3 will allow pump–probe time-resolved photoemission on the femtosecond timescale that will enable carrier driven chemical reactions and recombination processes to be followed in real time using valence band changes and core level shifts. Moreover, photoelectron diffraction will be used to monitor the geometry of transient intermediates. This will make use of a wide range of pump energies up to the UV from conventional lasers, which are necessary to investigate light harvesting photo-physics and chemistry.

The studies carried out so far have been performed in UHV conditions, which are quite distant from the pertinent technological environment. Investigation in more realistic conditions require the implementation of time-resolved NAPP experiments. One interesting study case to realize TR-NAPP would be the investigation of water chemistry on anatase TiO_2(001):(1x4). The process of water splitting by titania was discovered by Fujishima and Honda in 1972 [170]. Since then, there has been an immense drive to enhance the photo-stimulated activity of TiO_2. Such studies, typically carried out on single crystal TiO_2 substrates, have already resulted in a considerable archive of nanoscale information [171; 172; 173]. Furthermore, it has been shown that the anatase-TiO_2 polymorph is often more photo-active [174; 175] than the rutile phase. Moreover, anatase-TiO_2(001) has been reported to be highly photoactive for water dissociation [176]. The reason is related to the fact that UHV-prepared anatase-TiO_2(001) invariably exhibits a (1 x 4) reconstruction, which displays ridges consisting of twofold coordinated O (O2c) and fourfold coordinated Ti atoms (Ti4c) which drive water dissociation [176]. The role of point defects remains so far uncertain, in particular when operating near atmospheric pressure s[177]. Performing time-resolved NAPP experiments at different pressures at SXP will allow a detailed understanding of the water dissociation process under UV irradiation. In particular, the identification of weakly bound intermediates will shed further light of the mechanism of water dissociation. The study of samples with controlled level of oxygen vacancy defects will allow disentangling the role of the O_2-vacancies as hole traps to promote charge transfer to the conduction band. The energy range of SXP will allow performing XPS and XPD experiments at the O 1*s* and Ti 2*p*. From the O 1*s* studies, an accurate identification of the oxygen oxidation state will allow following the evolution of the different species appearing on the surface of the catalyst (OHtop, OHbridge, Ti-OH, Ti-O, peroxides, superoxide radicals, etc.). The Ti 2*p* spectra will also be monitored to investigate the chemical states and electronic structure of Ti^{2+}, Ti^{3+}, Ti^{4+} as well as chemical shifts due to the presence of oxidation states on the surface. The observation of chemical shifts to higher/lower binding energies than nominal Ti^{n+} (n integer) states would indicate the presence of hole/electron traps that would be enhanced in the anatase-TiO_2(001) film with oxygen vacancies. These

energies would permit to get information on the type of mechanisms coexisting at the surface of the catalyst: charge transport, trapping, and reaction of the photo-generated electrons/holes on the photo-excited TiO_2. Besides the intrinsic water splitting dynamics, the evolution of the C 1*s* will be measured during the reaction process to check the possible evolution of carbon growth contaminants on the surface as well as CO/CO_2 formation and its interplay with the water splitting efficiency.

The extended energy range at SXP will allow extending conventional soft X-rays NAPP studies into the NAPP-HAXPES regime. This implementation will facilitate to increase the pressure at which the experiments are performed, on the one hand, and to understand the role of the different layers in heterogenous samples [178] as well as to address interface electrochemistry at working electrodes, on the other hand.

2.2 Experimental setups

The proposed experiments will benefit from two systems developed to perform spin- and time-resolved photoelectron spectroscopy: a wide angle electron spectrometer (*WESPE*) equipped with commercial ToF detectors (University of Hamburg) and a home-built spin-filtered high-energy ToF momentum microscope (Johannes Gutenberg University Mainz) described in Section 2.2.2 on page 60. These two setups will allow performing most of the science applications discussed above at day one. The momentum microscope allows also for spatially resolved measurements. Other user groups have expressed their interest in bringing experiment stations optimized for PEEM microscopy, high temperature ARPES, etc. Special developments to realize NAPP experiments will be also studied and implemented.

2.2.1 Wide-angle electron spectrometer: WESPE

The wide-angle electron spectrometer (WESPE) is an ideal tool for time-resolved electron spectroscopy at high repetition rate FEL sources. In its final version, depicted in Figure 2.11 on the facing page, the WESPE experiment station will be equipped with two ToF spectrometers. This configuration will allow coincidence measurements of bulk- and surface-related electron dynamics and it will increase the overall signal intensity for some sample systems.

Currently, WESPE is equipped with only one ToF analyser (SPECS, model Themis 1000) with a segmented, position-sensitive delay-line detector (Surface Concept, 3D-DLD-4Q). The segmented DLD detector provides high detection efficiency with

single event detection capability. The spectrometer benefits from the wide detection angle and a good energy resolution (approx. 200 meV) within large energy windows (up to 18 eV width). The spectrometer is mounted to a µ-metal experiment chamber, which houses beam diagnostic tools and is connected to a further recipient for sample preparation. The preparation chamber is equipped with standard sample preparation tools, such as a sputter gun, a mass spectrometer, and a LEED/Auger system. Depending on the needs of the users, adding evaporators, a quartz crystal balance, a gas-inlet system, or a cleaving tool can extend the UHV system. The flexible sample holder system allows for variety of different sample materials, sizes, shapes, and preparation conditions to be transferred into the X-ray beam. The manipulator is equipped with a continuous-flow He cryostat and reaches temperatures of 25 K at the sample position. Experiments in UHV as well as in gas atmospheres are possible due to a gas-inlet system installed at the main chamber.

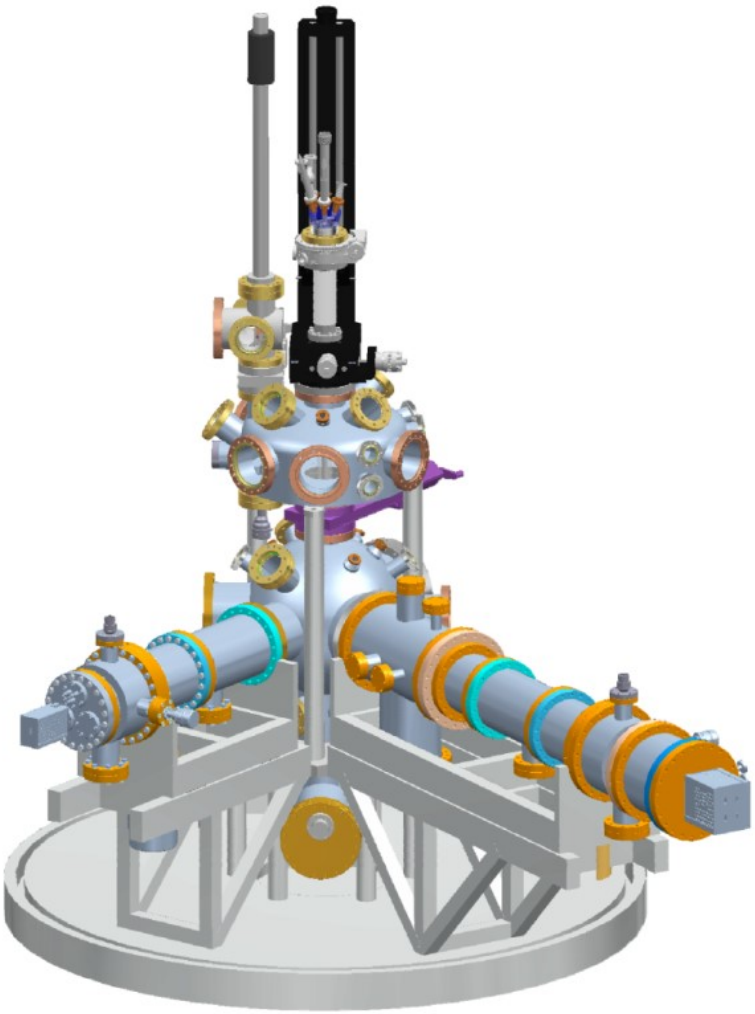

Figure 2.11: CAD model of the WESPE experiment station

2.2.2 Spin-filtered high-energy ToF *k-microscope*

In close cooperation with MPI Halle, the Mainz group has established ***ToF k-microscopy*** as a new "approach to ARPES" with the highest degree of parallelization [179]. The method has been patented [180]. This development adopted techniques from the earlier achievements of ToF-PEEM [181] and dynamic aberration correction [182]. The underlying idea of *k* space microscopy makes use of a basic concept of optics: in imaging systems, the reciprocal image represents the distribution of the transversal momentum components. (In mathematical language, it is also termed the Fourier image.) Owing to $k_{\parallel}$ conservation in the photoemission process, the reciprocal image formed in the backfocal plane of a cathode lens directly shows the transversal momentum distribution of the valence electrons inside the crystal. The intriguing advantage is that this method yields the (k_x, k_y) distribution in a very large region. For the high-energy instrument described below, half-space above the sample surface is covered for initial kinetic energies above >400 eV. Energy recording via ToF bears the advantage that many energy surfaces are acquired simultaneously. The measurements shown below employed the 40 bunch mode of the PETRA III storage ring with a pulse period of 192 ns. In an experiment at the MAX II storage ring, the full 100 MHz filling pattern could be used, i.e. 10 ns pulse period, which still provides sufficient time slices for core level XPD studies.

After just five years of development, the novel method has reached a high standard in terms of data acquisition speed due to the advent of delay line detectors with high count rate capabilities (~10^7 counts per second), developed by the spin-off company Surface Concept GmbH (Mainz). The combination of the Halle "microscope column" [183] with the "imaging time-of-flight technology" developed in Mainz provides a very high data acquisition rate: up to 10^7 (E_B, k_x, k_y) data *voxels* are acquired in parallel (E_B being the binding energy and k_x, k_y the transversal components of the photoelectron momentum vector). Using this first-generation ToF *k* microscope, comprehensive electronic structure analyses in many relevant systems have been performed at synchrotrons [179; 184; 185; 186; 187; 188; 189; 190; 191; 192]. In October 2017, in cooperation with the groups of the University of Hamburg – DESY, ETH Zürich, and Aarhus University, a first time-resolved pump–probe experiment at FLASH was carried out.

In order to extend the "*k*-microscope" applicability to the soft X-ray domain and pave the way to efficient time-resolved band mapping of large *k* fields and to ultrafast full field XPD, a new electron optics has been designed. The new lens accepts the full half-space above the surface up to initial kinetic energies of more than 500 eV, which corresponds to an increase of the maximum *k* field radius by a factor of ~3 compared to the low-energy design. Figure 2.12 on the next page shows the result of a ray

tracing calculation for the high-energy optics with the settings used in the experiments shown below. The three lens groups are schematically indicated by ellipses; Gaussian and reciprocal planes are denoted. A special objective lens designed for minimum spherical aberration forms the first *k* image in its backfocal plane (BFP). The electron beam is transformed to the scattering energy of the spin filter (not shown here) by zoom lens 1 and to the desired drift energy in the imaging ToF column by zoom lens 2. Photoelectron momentum maps (i.e. the E_B vs. *k* spectral function) are taken simultaneously in an energy interval of several electronvolts (typically 6 eV) width, limited by the photon footprint on the sample and the chromatic aberration of the instrument. Time markers with 10 ns spacing (dots) reveal planar isochrones, an essential precondition for good energy resolution and negligible "crosstalk" between longitudinal and transversal momentum components. The latter feature distinguishes this instrument from existing commercial TOF spectrometers.

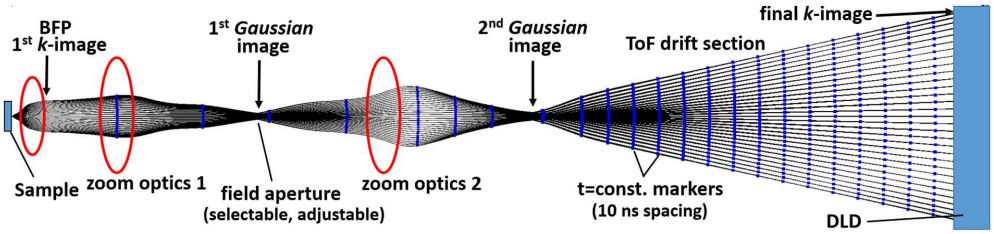

Figure 2.12: Simulated trajectories (program code *SIMION*) for the electron optics of the high energy *k*-microscope imaging a large momentum range. Here, a field of 16 $Å^{-1}$ diameter is focused to a delay line detector (DLD) of 80 mm diameter (rays for initial kinetic energy 3600 eV). Given an effective pixel resolution of 80 µm, the DLD records ~1 megapixel (Mpx) at a time resolution of 150 ps.

The key features of the soft X-ray "*k*-microscope" are summarized in the following.

Lens system: The new lens system has a large acceptance field, as already explained. Indeed the transforming the soft X-ray performance into real space coordinates allows a full image of half-space above the sample surface up to initial kinetic energies of >400 eV. For a kinetic energy of 3600 eV (simulation of Figure 2.12), 20 $Å^{-1}$ corresponds to a 2D angular range (full 360° azimuth) with 70° cone angle. The larger acceptance angle results in a gain of an order of magnitude in total intensity compared to the low-energy ToF *k*-microscope [179]. The larger *k* range increases the information content by imaging many BZs simultaneously. The recording of photoelectron diffraction patterns when measuring core level photoelectrons also becomes possible. Furthermore, it has also been shown to reduce space charge effects. Recent studies have shown they are produced by slow electrons [193]. The strong extractor field of the lens systems allows us to collect the

slow electrons into the lens column, thereby reducing the worsening of resolution induced by space charge effects. Since slow electrons travel essentially along the optical axis, due to their low transversal momentum, they will have almost no effect in the recorded momentum maps.

Energy resolution: The energy resolution derives from the energy dispersion: ΔE [meV] = 0.255 (E_d [eV])$^{3/2}$. It is defined by the length of the drift section, 900 mm, and a time resolution of the detector system of 150 ps. For drift energies E_d between 60 and 10 eV, the expected energy resolutions are ΔE = 70 meV down to 8 meV, respectively.

At a given voltage setting of the drift tube U_{drift}, only electrons within a certain energy interval can pass the ToF section. For example, with the sample bias set to the kinetic energy of the electrons at the Fermi edge ($U_{sa} = E_{kin}^{Fermi}/e$), an electron band between the Fermi energy and E_B is transmitted. Being a high pass filter, a ToF also transmits contributions of higher orders (2 $h\nu$, 3 $h\nu$) of the monochromator/undulator. These higher-order electrons are much faster and thus have a shorter time of flight. Due to their high energies, the higher-order electrons are essentially unfocused and pass the microscope column as a pencil beam, confined by the apertures in the ray path.

Detector: It is a delay-line detector (DLD). It has a diameter of 80 mm and a spatial resolution of 80 µm. This allows resolving almost 1 Mpx of image points, which is more than the resolution of the electron optics. The 150 ps time resolution allows a maximum integral count rate of 8 Mcps [194]. The DLD records all counting events in the selected E-$k_{\parallel}$ region confined by the constant energy surface at the Fermi energy E_F and the diameter of the k region of interest. The binding energy (with respect to E_F) is determined like in classical photoemission (E_B = hν- E_{kin} - Φ; Φ being the work function), utilizing the relation E_{kin} = (1/2) m_e(L/τ)^2 (L, τ, and m_e being the length of the drift section, the time of flight, and the electron mass, respectively). The events are accumulated in the (E_B, k_x, k_y) voxels of a 3D data array. For visualization, either the full 3D object is displayed or sections can be cut in any plane.

The operation of the spectrometer has been tested at the P22 beamtime of the PETRA storage ring. Experiments were performed on single crystals of Re (hcp metal). The full field observation of many repeated BZs and a core-level X-ray photoelectron diffraction (XPD) pattern on exactly the same k scale establishes a new type of photoemission experiment, which was impossible with conventional spectrometers and low-energy k-microscopes (imaging typically one BZ). The final state in photoemission is a “time-reversed LEED state” [16], since it contains

the contribution of all scattering paths experienced by the outgoing electron wave. Figure 2.13 shows large area k space patterns taken at $h\nu$ = 4800 eV for the d bands of Re at $T \approx 20$ K (cut through the Fermi surface (a)) and for the Re $4f_{7/2}$ core level at the same energy, showing the (pure) photoelectron diffraction (XPD) pattern (b). At such high energies, the valence band pattern (a) contains substantial contributions from XPD. This is evident from the diffraction signature (b) being superimposed on the band features in (a). Moreover, the final state energy isosphere is displaced by more than 1 BZ by the transfer of the photon momentum to the photoelectron. Combining the information on all the possible scattering paths for localized initial states and the momentum distributions for itinerant d electrons allows us to identify and eliminate the scattering contribution from the valence band pattern. The result is shown in (c), revealing the full k patterns of the central, first and second ring of repeated BZs (in total 19 BZs). The results confirm our new model of XPD on the basis of the Laue equations [195]. The high count rates pave the way towards spin-resolved HAXPES using an imaging spin filter as described below.

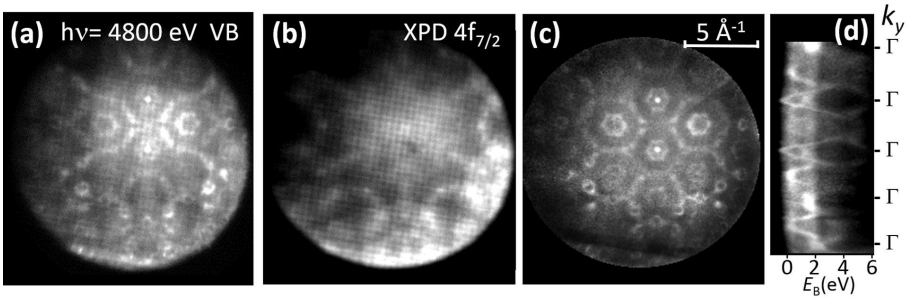

Figure 2.13: Large area momentum patterns of rhenium taken at hν = 4800 eV using the high energy microscope at Beamline P22 (PETRA III). k space maps shown for d band features (a) and 4f core-level photoelectron diffraction (b). Combining all information, the diffraction contribution in (a) can be eliminated, yielding the true band pattern (c) and corresponding band dispersions (d).

Spin detection: The momentum microscope can be used to perform spin-dependent measurement when inserting a spin filter in the electron optics. A spin filter crystal has been favoured over other possibilities, like conventional Mott detectors, because it allows us to perform vectorial spin detection. The total electron optical layout, including the imaging spin filter, is shown in Figure 2.14 on the following page. The rays have been calculated for the true geometry and for realistic settings. In the plot, the radial distance in both branches has been exaggerated by a factor 6 in order to show the details. In the (spin integral) lower branch, data arrays $I(k_x, k_y, \tau)$ (with τ being time of flight) are recorded by the first delay line detector (DLD 1). Depending on the energy bandwidth of the radiation, up to several hundred time slices are recorded simultaneously. For each counting event, the DLD records the three

coordinates (k_x, k_y, τ) and feeds them in real time into the data acquisition (DAQ), where the data are labeled with the corresponding individual microbunch number with its relevant parameters (like pulse intensity and true time).

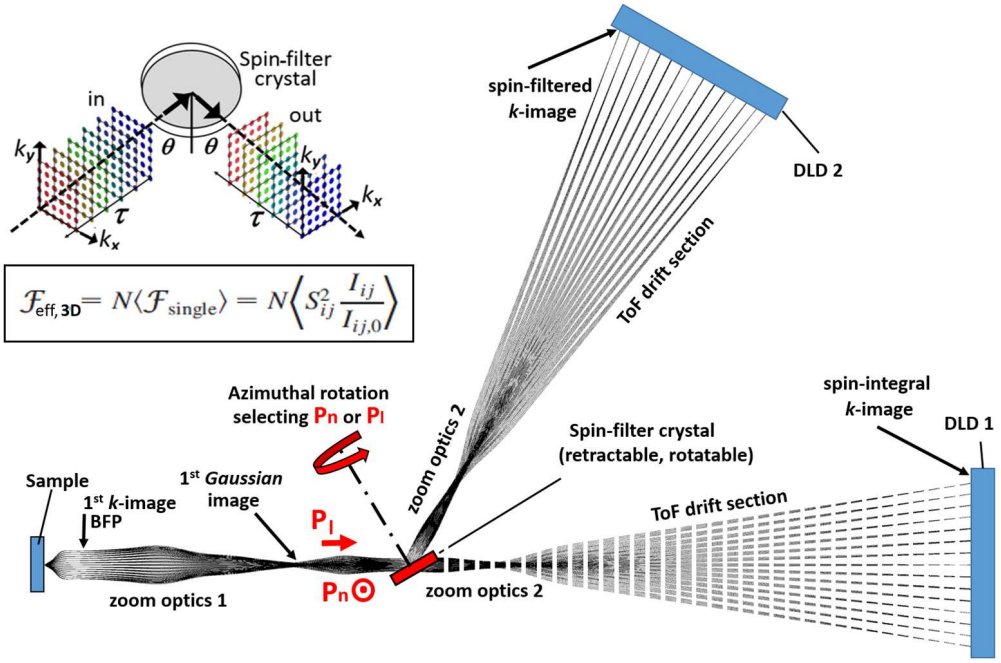

Figure 2.14: Ray-tracing calculation of the full electron-optical system of the high energy ToF momentum microscope, including spin filter. The retractable spin-filter crystal allows for a rapid change between spin-integral (straight branch, delay-line detector DLD 1) and spin-filtered imaging (upper branch, DLD 2). Azimuthal rotation allows us to switch from the transversal (Mott) component P_n to the in-plane spin component P_l. The electron-optical column consists of cathode lens (forming a *k*-image in the backfocal plane BFP), zoom optics 1 focusing a parallel beam on the spin-filter, zoom optics 2 (both in the lower and the upper branch) focusing a *k*-image on the DLD, and field-free ToF drift sections. Trajectories shown for 3000 eV initial energy (radial coordinate of the rays stretched by a factor 6). *Top-left inset:* Scheme of simultaneous detection of spin-polarization distribution $P(k_x, k_y, \tau)$ with τbeing the time of flight.

For spin-resolved imaging, the spin filter crystal is shifted into the beam in the field free space behind the lens column. This crystal acts as a spin mirror for the specular beam, which is imaged in the upper ToF branch (DLD 2), yielding spin-filtered data arrays. The top-left inset illustrates the principle of multichannel spin detection, resolving (k_x, k_y, τ) simultaneously. The figure of merit $F_{eff,3D}$ is defined by the equation in Figure 2.14 (with N being the number of resolved data points, S_{ij} the asymmetry function, and $I_{ij}/I_{ij,0}$ the reflectivity, both dependent on coordinates i, j). Besides the higher figure of merit, the ToF discrimination bears the additional advantage that inelastic electrons created in the spin-filter crystal are completely suppressed in the spin-filtered image (later arrival time τ). Moreover, the scattering

energy of the spin filter (typically in the range of 10–12 eV) sets a high pass cutoff for the recorded spectra, suppressing undesired low-energy background (and it allows for small detection periods as described in [191]).

Vectorial detection is achieved by azimuthal rotation of the spin filter. The component perpendicular to the scattering plane P_n (Mott component, perpendicular arrow in Figure 2.14 on the preceding page) is measured using the non chiral diffraction geometry, whereas the longitudinal component P_l (arrow pointing to the right) is recorded in the chiral geometry. The latter case bears the additional advantage that the asymmetry can be easily reversed by opposite sense of azimuthal rotation of the spin filter crystal.

Owing to its large acceptance range, the high-energy ToF *k*-microscope is ideally suited to measure the texture of the linear and circular dichroism in the angular distributions (LDAD, CDAD). These quantities originate from the orbital wavefunctions and are thus complementary to measurements of the spin texture, probing the spinor functions. Measurements in all different spectral ranges allowed observing pronounced dichroism textures that yield valuable information on orbital alignment in the initial state and orbital composition of the final photoemission states.

In Figure 2.15 on the following page, examples of spin-dependent measurements are displayed. In Figure 2.15(a), a cut through the surface and Brillouin zone of the ferroelectric α-GeTe is shown. Its spin texture is displayed in Figure 2.15(b). In Figure 2.15(c), a recent example for the CDAD texture in the Brillouin zone of tungsten is shown. Here, the CDAD was measured in 4D parameter space comprising the entire *d* band complex and full bulk Brillouin zone, quantified by the asymmetry $A_{CDAD}(E_B,k)$. Note that the figure shows only one of many energy isosurfaces. The dichroism in the *k* pattern provides an important quantity on the quest to the complete photoemission experiment (further details on this issue can be found in [185]).

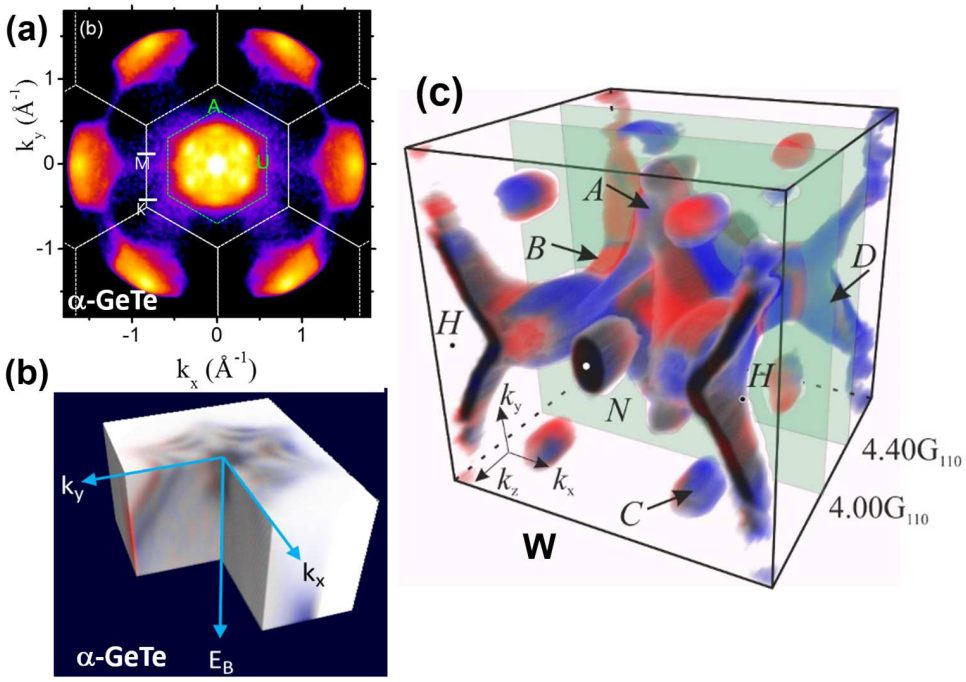

Figure 2.15: (a) k_x-k_y cut through the surface and bulk Brillouin zones in the ZAU plane at E_F. (b) Spin polarization texture of the ferroelectric bulk Rashba semiconductor α-GeTe. The spin measurement revealed Rashba split bulk and surface states (from [188]). (c) Circular dichroism texture of tungsten at E_F measured in the soft X-ray range at beamline P04 (from [196]).

3 Soft X-ray spectroscopy of high-valent metal intermediates in biological and inorganic catalysts for chemical bond activation

Jan Kern, Vittal Yachandra, Junko Yano
Molecular Biophysics and Integrated Bioimaging Division, Lawrence Berkeley National Laboratory, Berkeley, USA

Uwe Bergmann
Stanford PULSE Institute, SLAC National Accelerator Laboratory, Menlo Park, USA

Marcus Lundberg
Department of Chemistry, Ångström Laboratory, Theoretical Chemistry, Uppsala University, Sweden

Johannes Messinger
Department of Chemistry, Ångström Laboratory, Molecular Biomimetics, Uppsala University, Sweden

Michael Odelius
Department of Physics, Stockholm University, Sweden

Rolf Mitzner
Institute for Methods and Instrumentation for Synchrotron Radiation Research, Helmholtz-Zentrum Berlin für Materialien und Energie GmbH, Berlin, Germany

Philippe Wernet
Department of Physics and Astronomy, Uppsala University, Sweden

Biological and inorganic catalysts activate chemical bonds in a number of important reactions. Prominent examples in nature are the light-induced oxygen generation by water oxidation in photosystem II (PSII), hydrogen atom abstraction with P450 proteins, and the catalytic hydroxylation of C-H bonds with monooxygenase proteins.

The essential reaction intermediates in these processes are often oxo or oxyl radical species bound to high-valent first-row transition metal atoms. One key to understanding the reactivity of these species is to probe their electronic structure [197]. Soft X-ray spectroscopy at the metal *L*-edges is ideally suited for this and the soft X-ray port at SASE3 at the European XFEL uniquely enables such experiments.

3.1 Science case

The aim of this application is to understand bond activation with biological and inorganic catalysts in solution by probing the electronic structure of high-valent metal intermediates with soft X-ray spectroscopy. The plan is to investigate a series of bond-activating metalloproteins and inorganic complexes with metal *L*-edge absorption spectroscopy. The focus of the project will be water oxidation with PSII, hydrogen atom abstraction reactions and C-H bond hydroxylation. For each case, the idea is to perform a series of steady-state and time-resolved measurements on corresponding metalloproteins, their model complexes, and inorganic complexes that catalyze related reactions. The femtosecond duration of the X-ray pulses from European XFEL will be essential for these measurements.

In a number of the catalytic reactions to be studied, the important reactive intermediates are metal oxo M=O and M-O oxyl radical species, where M is the 3*d* transition metal and O is an oxygen ligand atom. They arise in a number of different oxidation states, and bonding configurations exist during the reactions and empirical correlations between catalytic activity and the electronic structure at the active metal center. Mechanistic understanding with simple rules that relate the electronic structure of the metal and the reactivity of a species, however, are largely missing. Metal *L*-edge absorption spectroscopy gives direct access to the metal-derived frontier orbitals. Oxidation states, charge and spin density distributions, “metal-ligand bonding” and coordination, and metal spin states become directly accessible. Combined with electronic-structure calculations, our measurements will provide unprecedented mechanistic insight into chemical bond activation. Such information could build the basis for the directed design of new artificial catalysts.

The proposed experiments require highly brilliant tunable soft X-ray radiation with pulse durations in the femtosecond range. High average brilliance is needed to detect the dilute species under *in operando* conditions at room temperature in solution in the mmol/l regime. Compared to X-ray FELs with repetition rates in the Hz regime, the higher repetition rate of the European XFEL is essential because it guarantees high enough average photon flux for the planned experiments. This is critical as we propose to use fluorescence detection for X-ray absorption spectroscopy to

discriminate the solute signals from solvent background. Due to the low fluorescence yield of 3*d* transition-metal atoms in the soft X-ray range, the achievable count rates even with high-throughput soft X-ray spectrometers and detectors are notoriously low.

The femtosecond duration of the X-ray pulses from the European XFEL is essential in two ways. First, as our previous work on PSII with Mn *L*-edge absorption spectroscopy showed [198], it enables probing the high-valent metal species in metalloproteins before X-ray-induced sample damage sets in. The critical damage mechanism for the high-valent species we plan to study is photo-reduction by electrons created by soft X-ray absorption in the sample, and this can be outrun with femtosecond pulses. The planned experiments are not possible at synchrotron radiation sources because the X-ray pulses are too long and, in addition, the repetition rates are too high to allow for the necessary sample replenishment between consecutive X-ray pulses. This has been the primary reason that soft X-ray spectroscopy has been underutilized for the study of biological systems and molecular catalysts in solution, despite its potential to reveal the electronic structures.

Second, the femtosecond X-ray pulse duration enables corresponding temporal resolution in optical pump and X-ray probe experiments of inorganic metal complexes where photo-excitation will be used to create short-lived transient intermediates of high-valence metal oxo and oxyl species.

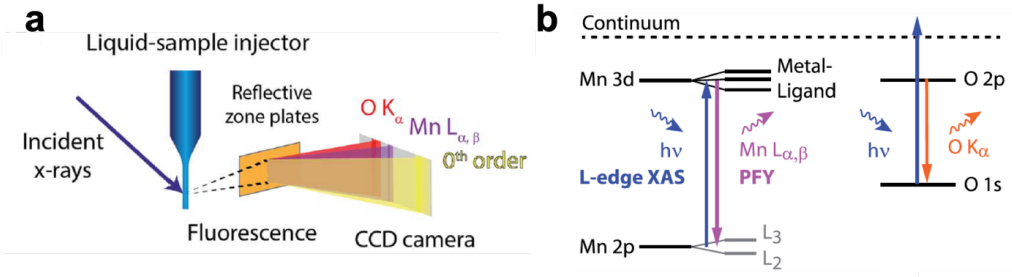

Figure 3.1: (a) Schematic of the experimental setup for fluorescence-detected X-ray absorption spectroscopy with the liquid-jet injector, the incident X-ray beam, and the soft X-ray spectrometer with reflective zone plates that disperse the fluorescence emitted from the sample into its various contributions. Shown here is the exemplary case of probing PSII with Mn *L*-edge absorption spectroscopy with O K_α fluorescence, mainly due to the solvent, and Mn $L_{\alpha,\beta}$ fluorescence from the oxygen evolving complex, Mn_4CaO_5, in PSII (adapted from [199]). (b) Scheme of partial-fluorescence yield (PFY) X-ray absorption spectroscopy (XAS). The provided example corresponds to the Mn *L*-edge absorption with dominating one-electron transitions for absorption and fluorescence at the Mn *L* and O *K*-edges (adapted from [198]).

3.2 Theoretical support

Ab-initio theoretical approaches have been developed to calculate X-ray spectra of comparably small inorganic complexes from first principles [199; 200]. Developments to enable calculations of X-ray spectra of larger systems including inorganic and biological catalysts in solution are ongoing. In parallel, a continuously improvement of the models is undergoing in order to accurately describe the solvation of the studied systems to effectively account for the active role of the solvent in the studied reactions and the effect the solute–solvent interactions have on the X-ray spectroscopic observable. Such developments are important to enable meaningful interpretation of the data we expect to acquire at the soft X-ray port at SASE3 of the European XFEL. Future developments with increased efficiency of the described soft X-ray spectrometer and with optimized combinations of jet flow rates and X-ray repetition rates could allow measuring metal *L*-edge spectra at concentrations below 1 mmol/l. Our planned systematic studies with partial-fluorescence yield X-ray absorption spectroscopy at the SXP experiment will finally help designing future metal 2*p*3*d* RIXS (resonant inelastic X-ray scattering) experiments of inorganic and biological catalysts under *in operando* conditions.

3.3 Experimental setup

The experimental technique used for this project is to perform partial-fluorescence yield X-ray absorption spectroscopy at the 3*d* transition-metal *L*-edges. The experimental setup is sketched in Figure 3.1 on the previous page. It uses a liquid-jet injector for sample delivery. The samples, upon interaction with the incident X-ray beam, will produce soft X-ray fluorescence that will be analysed using a spectrometer with reflective zone plates. In order to illustrate the process, the example of probing the fluorescence of PSII upon excitation at the Mn *L*-edge absorption edge is displayed. Two fluorescence regions will be observed: (i) one at the O K_α, mainly due to the solvent, and (ii) another at the Mn $L_{\alpha,\beta}$, coming from the oxygen evolving complex, Mn_4CaO_5, as seen in Figure 3.1(a) adapted from [198].

In Figure 3.1(b), a detailed scheme of the partial-fluorescence yield (PFY) X-ray absorption spectroscopy XAS is shown for Mn *L*-edge absorption edge. The dominating one-electron transitions for absorption and fluorescence at the Mn *L* and O *K*-edges are indicated. The soft X-ray spectrometer allows discriminating the weak metal fluorescence signal from the concurrent O K_α fluorescence (O 2*p* to 1*s* transitions), resulting from unavoidable 1*s* ionization of O in the sample, mostly from the solvent. The metal fluorescence signal $L_{\alpha,\beta}$ corresponding to 3*d* to 2*p* transitions

is measured as a function of incident photon energy across the metal $L_{3,2}$ absorption edges, resonant metal 2*p* to 3*d* transitions.

In order to realize these experiments, a setup, displayed in Figure 3.2(a), has been developed in recent years for experiments at BESSY II and LCLS [201; 198]. It includes a liquid-sample injector, shown in Figure 3.2(b), and an X-ray spectrometer using reflective zone plates as shown in Figure 3.2(c). The system is easily movable and would be connected to SXP at SASE3 of the European XFEL.

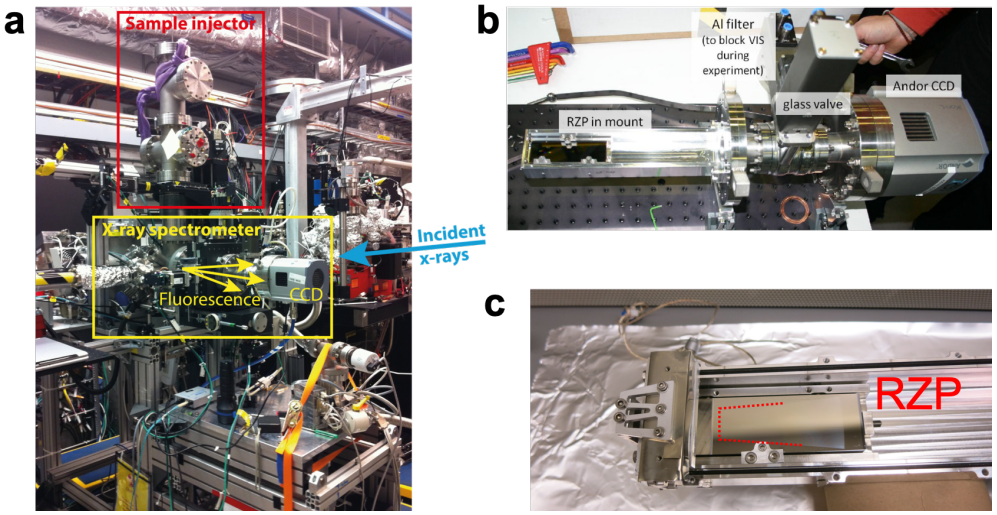

Figure 3.2: Setup for partial-fluorescence yield X-ray absorption spectroscopy of dilute metalloproteins and inorganic metal complexes in solution. (a) Overview of the setup (as installed at the SXR instrument of the LCLS X-ray FEL). (b) The high-throughput soft X-ray spectrometer with reflection zone plates (RZP) and CCD detector. (c) Close-up of the RZP with diffractive RZP patterns on the substrate.

The liquid-sample injector, shown in Figure 3.2(b), has been developed with the aim of hitting a given sample volume only once to avoid X-ray–induced sample damage. Depending on the flow speed of the liquid jet and the X-ray spot size, the repetition rate could be optimized to reach 1 MHz. Depending on the sample, the diameters of the jets will be in the range of 5–20 µm. This determines the optimal horizontal X-ray spot size from below 5 µm to approximately 10 µm. Ideally, the vertical X-ray spot size could be set independently from the horizontal dimension to 100 µm or above to control X-ray photon density on the sample and avoid non-linearities in the signal, if necessary.

With the existing setup, a rate of 5 counts/s for Mn *L*-edge absorption spectroscopy of PSII at a Mn concentration of 0.8 mmol/l has been achieved. The described method allowed the realization of experiments at LCLS with 120 Hz, which is at the limit of

experiment feasibility [198]. With typical concentrations in the low mmol/l regime for metalloproteins and catalytically active inorganic complexes in solution, a higher repetition rate in the range of kHz–MHz will improve the signal, as any increase in repetition rate directly translates to a higher count rate in our approach. SXP at SASE3 at the European XFEL with corresponding repetition rates and tunable spot size will therefore enable systematic studies of the described soft X-ray spectroscopic technique.

4 Laboratory astrophysics, atomic physics, and fundamental research with highly charged ions

José R. Crespo López-Urrutia, Chintan Shah, Steffen Kühn, Moto Togawa, Zoltan Harman, Natalia S. Oreshkina, Adriana Pálffy, Christoph H. Keitel, Thomas Pfeifer
Max-Planck-Institut für Kernphysik, Heidelberg, Germany

Sven Bernitt, Thomas Stöhlker
Helmholtz-Institut, Jena, Germany

Natalie Hell, Gregory V. Brown
Physics Division, Lawrence Livermore National Laboratory, Livermore, California, USA

Thomas M. Baumann, Michael Meyer
European XFEL GmbH, Schenefeld, Germany

René Steinbrügge, Günter Brenner, Ivan A. Vartaniants
Deutsches Elektronen-Synchrotron DESY, Hamburg, Germany

Renata S. Cumbee, Makoto Sawada, Maurice A. Leutenegger
NASA Goddard Space Flight Center, Greenbelt, Maryland, USA

Randall K. Smith ***Center for Astrophysics, Harvard and Smithsonian, Cambridge Massachusetts, USA***

Jakob Stierhof, Jörn Wilms
Dr. Karl Remeis-Observatory and ECAP, University of Erlangen-Nuremberg, Bamberg, Germany

Gabriele Betancourt-Martinez
Institut de Recherche en Astrophysique et Planétologie (IRAP), CNRS, Toulouse, France

Matteo Guainazzi
ESA-European Space Agency, Directorate of Science, ESTEC, Noordwijk, The Netherlands

Peter Kretschmar
European Space Astronomy Centre (ESA/ESAC), Villanueva de la Cañada, Madrid, Spain

Ehud Behar, Itay Gissis
Department of Physics, Technion, Haifa, Israel

Andrey Surzhykov
Technische Universität Braunschweig, Braunschweig and Physikalisch-Technische Bundesanstalt, Braunschweig, Germany

Julian Berengut,Victor V. Flambaum*
School of Physics, University of New South Wales, Sydney, Australia
*** also Johannes Gutenberg-Universität, Mainz, Germany***

Marianna Safronova
Department of Physics and Astronomy, University of Delaware, Newark, USA and Joint Quantum Institute, National Institute of Standards and Technology and the University of Maryland, College Park, Maryland, USA

At the SASE3 beamline of the European XFEL, the brightest beams in the soft X-ray domain will become available, with pulse durations down to a few femtoseconds and maximum intensities up to 10^{18} W/cm^2, and highly monochromatic beams with energy resolution up to 40 000 at high flux. The ultimate resolution will become available with the foreseen installation of the long high-resolution grating. Furthermore, self-seeded beam and split-and-delay optics with up to 40 ps range are envisioned. Generation of circularly polarized radiation is also planned. With these capabilities, new scientific frontiers can be pursued. In particular, it is an excellent platform for extending the current research with highly charged ions (HCI) to intensities and fluxes that will enable novel studies of fundamental and applied nature.

We propose the use of a **miniature electron beam ion trap** (EBIT) [202] of the Polar-X type (shown in Figure 4.1 on the facing page) at SXP in order to provide a transparent target of HCI for the X-ray photon beam (see Figure 4.2 on page 76). This apparatus can be combined with spectral diagnostics, such as grating spectrometers, single-photon detectors, and ion detectors. Pump–probe experiments using the split-and-delay unit or pulsed IR lasers are also envisioned. A unique feature is the fact that the photon beam can pass the EBIT and reach other experiments downstream for simultaneous photon energy as well as pulse intensity calibration.

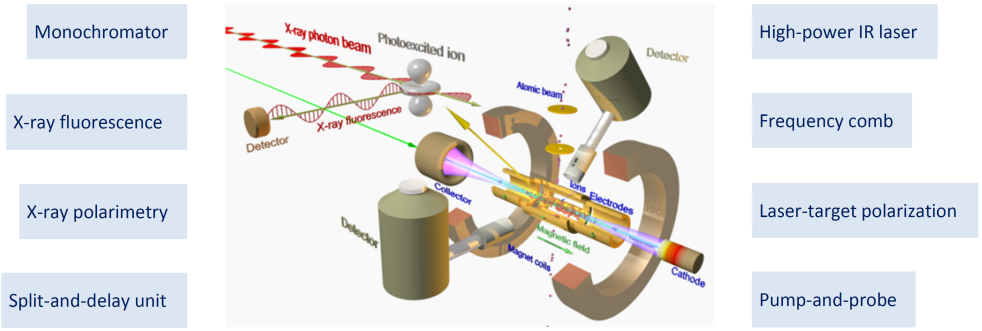

Figure 4.1: Principle of X-ray excitation of highly charged ions in an electron beam ion trap. Fluorescence from the trapping region from resonantly excited ions is registered as a function of the monochromator settings. Additionally, photoions produced in the trap beam can be extracted and diagnosed. Other various techniques can be additionally applied.

4.1 Scientific rationale

At soft X-ray energies, free atoms and molecules are photoionized, and the number of bound electrons and electronic structures changes dynamically. This time evolution is difficult to measure and to reproduce by theory. Testing atomic or molecular structure theory at such high fluxes is therefore very challenging. Since FELs are now routinely accessing this range of fluxes, numerous applications depend on a detailed understanding of the time evolution of microscopic processes. X-ray imaging and diffraction studies, high-energy density physics, and many experiments in atomic, molecular, and cluster science at X-ray FELs encounter HCI at some point in the time evolution of the systems. Studying and understanding them is, therefore, crucial.

From the point of view of quantum science, HCIs are perfectly reproducible systems of bound fermions that mutually interact with a scale length ($\sim 1/Z$) given by the nuclear charge Z. The electromagnetic interaction strength results from the product of Z and the fine-structure constant α. While binding energies depend on $(Z\alpha)^2$, relativistic and quantum-electrodynamic effects grow with $(Z\alpha)^4$, and certain nuclear-size contributions to the binding energy are proportional to even higher powers of this coupling parameter. As an example, the hyperfine interaction of the $1s$ electron with the nucleus of a heavy HCI is on the order of 10^{-4} times the total binding energy, and in terms relative to the neutral H atom, a million times larger. HCI studies have been the realm of precision atomic structure experiment and theory, and excellent experiments as well as advanced codes have been developed over the last three decades. Recently, cooling of HCIs after their preparation down to mK-level temperatures has been achieved at the Max-Planck-Institute für Kernphysik (MPIK) [203], and an experiment achieving a relative energy resolution of 10^{-15} akin to

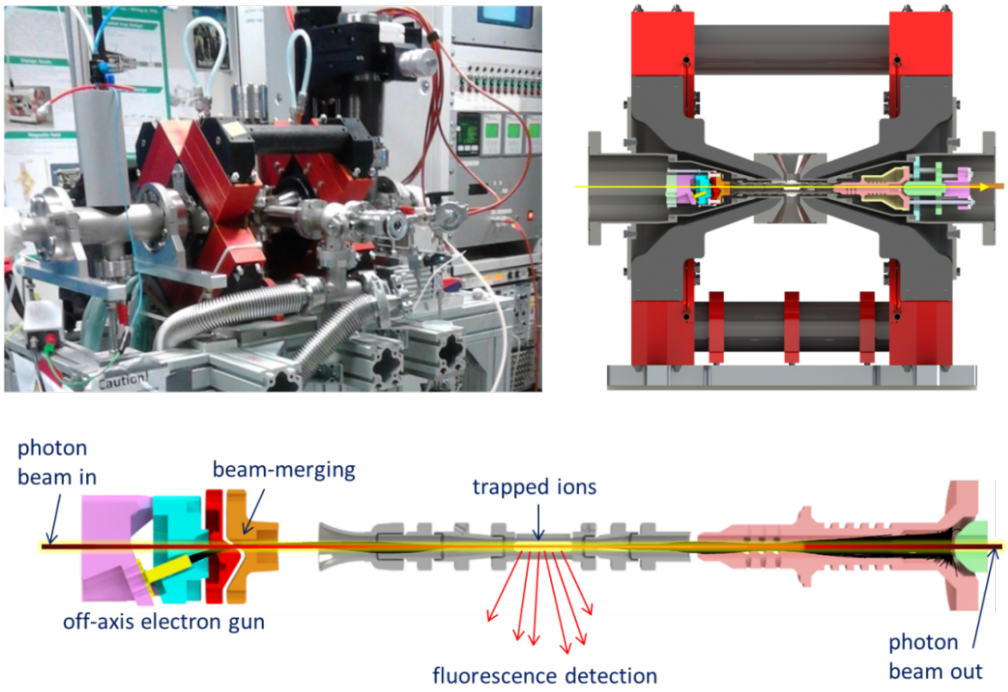

Figure 4.2: Electron beam ion trap (EBIT) with an off-axis electron gun. The device allows the beam to pass through, and only photons that have interacted with the trapped highly charged ions (HCIs) are absorbed. The areal density of the HCI target is on the order of 10^{10} ions/cm^2. *Top left:* Photograph of Polar-X EBIT [202], the prototype for these applications, at PETRA III. *Top right:* Section through the apparatus. *Bottom:* Principle of the arrangement. Photon beams are transmitted unhindered but excite HCI trapped in the central drift tube. Subsequent fluorescence photons are detected through side ports. In this type of setup, photoions can be extracted and analysed as well.

that of high-precision atomic clocks has been just reported by the collaboration Physikalisch-Technische Bundesanstalt (PTB)-MPIK (P.O. Schmidt and JRCLU) [204]. With this demonstration, it has been shown that all the laser spectroscopic and frequency metrology methods can be applied to HCI, thereby expanding the range of precision physics into the “third dimension” of the periodic table, the “charge coordinate”. This is particularly interesting since HCI in appropriate charge states are impervious to X-ray irradiation, and can act as probes for extremely strong electromagnetic fields. Novel physics studies are possible in this way (see Review [205]). HCI can be prepared and stored in well-defined charge states using EBITs [206; 207; 208]. Within the electron beam interaction zone, where the HCI are confined, target densities up to 10^{10} ions/cm^2 can be reached. The charge states of choice are produced by the interaction of a dense electron beam with neutrals. A mono-energetic electron beam generated by a small gun allows selecting the desired charge state. High-energy EBITs can produce up to naked U^{92+}, more common

low-energy devices fully strip ions up to Z=36, and work with few-electron HCI all the way to the end of the periodic table. This capability is particularly interesting for the investigation of iso-electronic sequences, in which a fixed number of bound electrons is prepared with a variable nuclear charge [209; 210].

Under the conditions of electron-beam excitation, the trapped HCI copiously emit radiation. Spectroscopic studies from the optical to the X-ray region have been carried out with trapped HCI since the late 1980s [206; 207; 208]. Starting in 2006, the MPIK group demonstrated soft X-ray laser spectroscopy at FLASH (50 eV)[211], then at LCLS (800 eV) [212], and since then the energy range has grown from there to more than 14 keV. Work with EBITs on photoionization [213; 214; 215] and X-ray resonant fluorescence spectroscopy [216; 217] also at storage ring facilities has benefited from the high-resolution monochromators available there. Recent examples of Polar-X EBIT campaigns at PETRA III are shown in Figure 4.3 and Figure 4.4 on page 79, covering the energy range from 0.5 to 7 keV. However, non-linear photonic studies with HCI in the X-ray region at resolving power beyond 1000 have not yet been possible at X-ray FELs. A high-flux, high-power density beamline such as SASE3 at the European XFEL, in combination with an EBIT, offers therefore new and unique possibilities for research in fundamental atomic physics and laboratory astrophysics, and can also serve as a perfect photon-energy calibration and reference outperforming Bragg-reflection, crystal-based systems.

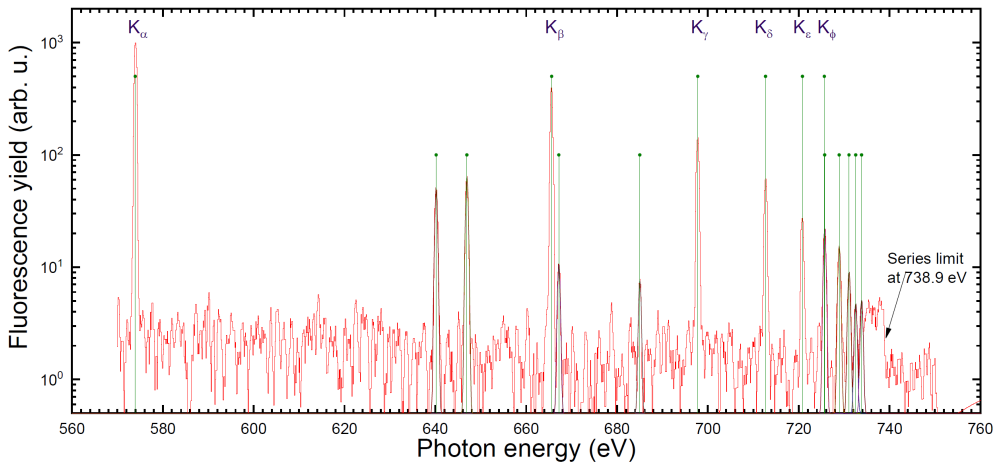

Figure 4.3: Example of a low-resolution excitation spectrum of helium-like O^{6+} ions obtained at PETRA III, Beamline P04, with Polar-X EBIT. In line narrow scans, the experiment reached a resolving power up to E/ΔE±30000. Ultrashort pulses at the European XFEL SASE3 beamline will offer unique possibilities for multi-photon and high-resolution investigations of such ions.

In the short term, the most important scientific goals of HCI research at SXP are:

- Study of **non-linear multiphoton processes** with selected isoelectronic sequences in order to test theoretical models of those interactions (e.g. see [218; 219]). Both photoexcitation and photoionization studies with the EBIT will test advanced time-dependent quantum dynamics theory. Such benchmarked theories are needed for modeling more complex systems, such as photoionized and other high-temperature plasmas found both in astrophysics and high-energy density (HED) physics, for modelling opacity studies [220], and for treating the response of molecules as well as condensed matter in the presence of ultrabrilliant radiation fields.

- Determination of **upper-state lifetimes for soft X-ray transitions** of mid-heavy to heavy elements (O, Ne, Mg, Si, S, Fe, Ni) in the range of few fs to 40 ps. These transitions are essential for energy transfer in the radiative and convective zones of stellar cores, and determine their X-ray opacity, an active research field with many open questions ([220] and references therein). Lifetimes are also essential for the diagnostics of astrophysical plasmas. For lifetimes in the picosecond range, a split-and-delay unit will be needed, since the natural linewidths used to extract femtosecond lifetimes (e.g. in [213; 216]) cannot be resolved with the monochromator, and will require a pump–probe scheme for their measurement in the time domain. Such a unit would also have other various uses, e.g. studies of population transfer between excited states as well as electronic wave-package formation and evolution, and become a key tool for quantum-dynamics studies.

- **High-resolution investigations of astrophysical processes** occurring in hot plasmas in the laboratory. Upcoming novel space observatories (XRISM, Athena) equipped with high-resolution X-ray microcalorimeter arrays will provide revolutionary results, as shown by the X-ray space observatory Hitomi [221; 222] before its unfortunate demise. With large light collection areas, they will deliver high statistics imaging spectroscopic data with hitherto unreached resolution. Its analysis will require significant improvements of models for both collisionally ionized and photoionized plasmas[223; 224]. This task involves atomic and plasma theory, as well as the corresponding laboratory astrophysics studies.

- **Establishing state-of-the-art photon energy references** beyond those now available using absorption edges (10^{-4} relative accuracy), Bragg reflections, and Mössbauer spectroscopy (10^{-8} in the best case). HCI provide symmetric, perfectly reproducible electronic transitions covering from the soft X-ray energy range up to 100 keV, and with intrinsic uncertainties that are many orders of magnitude smaller than all solid-state based ones. After several

decades of theory development and stringent benchmarking through EBIT experiments, the few-electron isoelectronic sequences, such as hydrogen-like, helium-like, and lithium-like, can now be reliably calculated *ab-initio*, giving absolute X-ray references with sub-meV theoretical uncertainties. More complex isoelectronic sequences can be cross-referenced to the few-electron systems and perfectly provide narrowly spaced photon energy references.

- **Development of X-ray frequency combs** through interactions of IR frequency combs in impulsively X-ray excited systems. Such experiments have recently been proposed [225] and should use the dynamic modulation of population transfer between two X-ray FEL excited states by means of an IR frequency comb laser that imprints its time structure on the X-ray fluorescence emission. In combination with VUV frequency combs [226; 227; 228], eventually this can help extending frequency metrology from the optical to the X-ray region. A VUV frequency comb with applications to trapped HCI is currently under development at MPIK [229; 230].

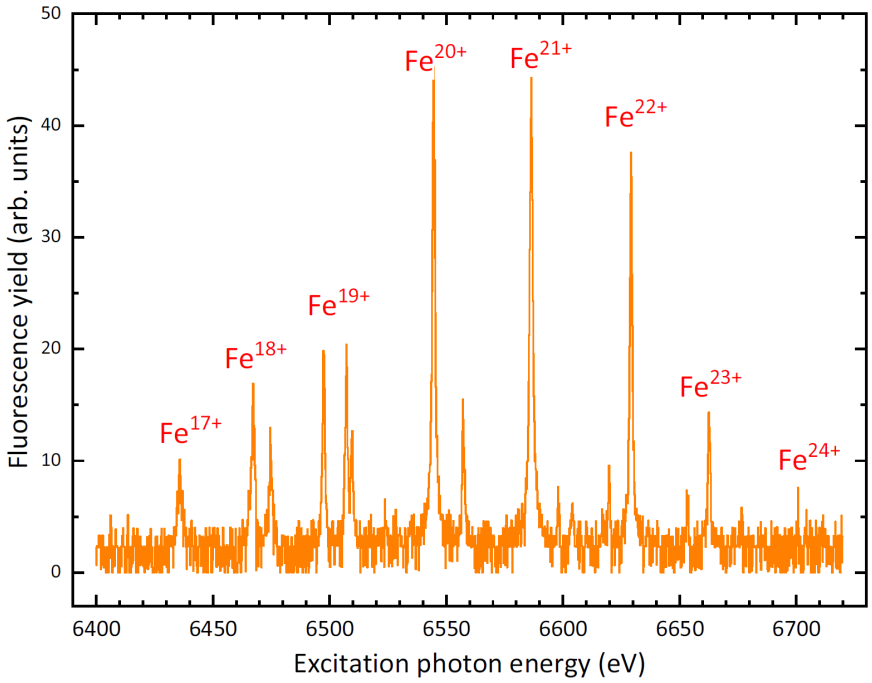

Figure 4.4: Fluorescence spectrum of highly charged iron ions obtained at the PETRA III P01 beamline in 2019 with Polar-X EBIT. The bound–bound transitions shown here are essential for radiative energy transfer in the solar core. Multi-photon excitation of these transitions will be possible at using the soft X-ray photons produced by the SASE3 undulators of the European XFEL, mimicking intra-stellar processes.

For these purposes, the setup would, in its basic configuration, include a miniature

EBIT [202] and X-ray fluorescence diagnostics, including a microcalorimeter [231; 232] and photo-ion diagnostics with extracted ions, and, in a planned upgrade, an additional cryogenic radio-frequency ion trap [233; 234] in which HCIs extracted from the EBIT can be prepared in well-defined quantum states at microkelvin temperatures and stored for periods of time of up to one hour. The proposed arrangement would require approximately 10 m^2 floor space, as shown in Figure 4.5, and can take different positions in order to use the photon–HCI interaction zone inside the EBIT or the RF trap. In both cases, the photon beam can pass through the setup and be used for a subsequent experiment downstream.

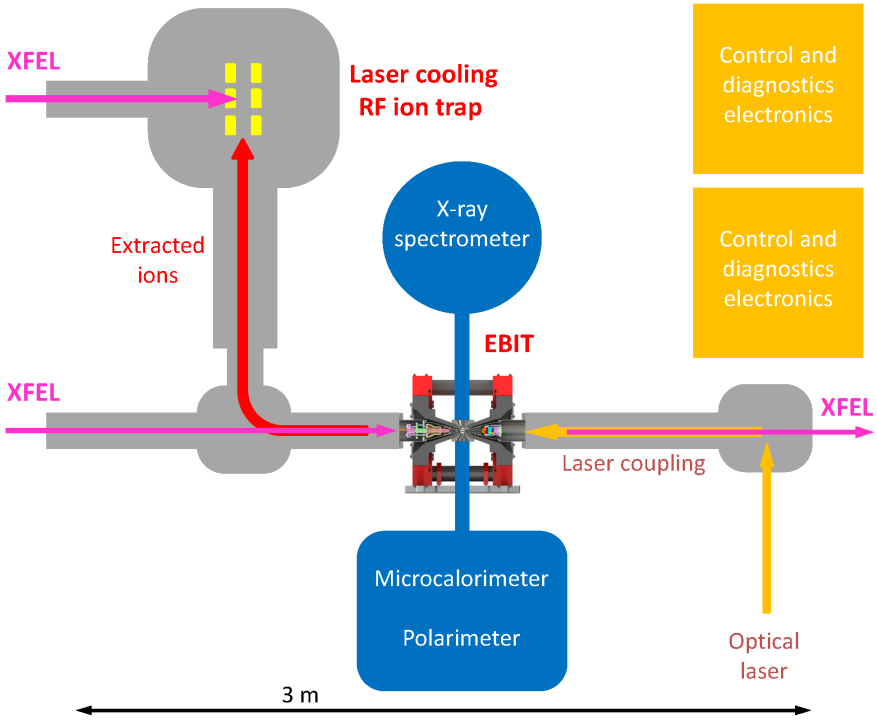

Figure 4.5: Arrangement of a miniature EBIT and laser cooling RF ion trap with X-ray fluorescence and polarimetry diagnostics. By moving the apparatus, either the HCI ensemble trapped inside the EBIT or the RF ion trap after sympathetic laser cooling can be exposed to the X-ray FEL beam. The use of an X-ray microcalorimeter [231; 232] and an X-ray polarimeter provides excellent diagnostic opportunities for the X-ray fluorescence generated through X-ray FEL excitation. Additionally, optical lasers can be used to prepare the target HCIs both metastable or polarized states, and for quantum interrogation of the HCIs. In combination with the X-ray FEL monochromator and split-and-delay unit, this setup opens the possibility to generate frequency combs in the soft X-ray regime, investigate photon–HCI interactions at extremely high energy resolution, and monitor the time evolution of metastable as well as polarized states.

4.2 Additional scientific perspectives

Novel, and in the mid-term as well as long-term, extremely interesting scientific perspectives of research are enabled by the soft X-rays at the SASE3 beamline. Foremost is the investigation of fundamental physics interactions making use of circularly polarized X-rays and HCI: parity violation (PV), nuclear-size effects (NSE), isotopic shifts (IS), and electron electric dipole moments (eEDM). The underlying processes have already been studied with very high accuracy in atomic physics experiments and are the subject of intense research effort (see Review [235]). The eEDM results (Review [236]) are already providing strong boundaries for the validity of the largest group of super-symmetric theories (SUSY), which predict the existence of eEDM values that those experiments have excluded in recent years. At their current level, the eEDM experiments test physics at higher energies than LHC through the exclusion of hypothetical particles, which would have measurable effects on the atomic processes. Future experiments in this field aim at higher sensitivities to the sought-after particles and basically plan to use the heaviest available nuclei that provide usable laser-excitable transitions. In contrast, PV (also called parity non-conservation, PNC) experiments, actually measure the interaction of a heavy elementary particle, namely the Z0 boson, with the bound electron, yielding the Weinberg angle with an accuracy that has been competitive to the high-energy experiments [235]. Improved PV studies will continue testing the low-momentum exchange regime of the unified electroweak interaction, and could soon surpass the high-energy counterparts. Regarding NSE, the paradigmatic example is the proton-radius puzzle: spectroscopic experiments with muonic hydrogen and hydrogen atoms [236] give more accurate results for this essential quantity than decades of high-energy electron-scattering experiments had achieved, in part due to the extreme spectral resolution of the former, but also due to unrecognized uncertainties in the complex scattering form factors in the latter. Similarly, NSE in HCI were already used to determine nuclear charge as well as magnetization distributions of heavy nuclei [237; 238; 239; 240] and provided data for nuclear physics and QED tests [241; 242].

Such experiments can be extended to higher photon energies in heavy atomic systems, now accessible by the combination of ultrabrilliant, circularly polarized, high flux sources such as SASE3 and traps containing HCI with “engineered” sensitivities to NSE, IS, PV, and potentially to eEDM. The expanded photon energy range and the high pulse intensity allow coupling sufficiently degenerate electronic states, which can mix with opposite-parity ones, to detectable transitions, inducing circular-dichroism in the X-ray domain, and thus measurable changes of polarization and angular anisotropy. In principle, the sensitivity of ultraprecise isotopic-shift experiments to

new physics that has been theoretically identified in various recent works [243] applies even more when deeply bound electrons are investigated. PNC experiments have been proposed for decades for heavy ion storage rings, e.g. with helium-like gadolinium and europium [244], and other schemes [245; 246; 247; 248] based on polarimetry techniques, but the technical difficulties in such an environment are still daunting and have hindered realization. In contrast, HCI polarization through laser interaction in a trap can provide a perfectly defined initial state, and the photon flux and polarization of the SASE3 beamline can provide the required clean experimental conditions in the X-ray excitation and detection sector.

5 Technique development

Jan Grünert, Manuel Izquierdo
European XFEL GmbH, Schenefeld, Germany

This proposition comes from European XFEL groups. The aim is to develop new photon diagnostics tools and investigate new experimental techniques.

5.1 Development of new photon diagnostics

In the construction phase, the X-Ray Photon Diagnostics (XPD) group developed and implemented the baseline diagnostics for the facility, which was used during the facility commissioning phase and is now applied for the user programme in all beamlines.

In the operation phase, XPD continues to develop, test, and implement novel X-ray beam monitors. During this development, new instrumentation must be thoroughly tested with X-ray FEL radiation, first at the prototype stage and later as final device before integration into the beamlines in the tunnels. This is best performed at one of the scientific end stations in the experiment hall for several reasons: Instrumentation under development has to be often accessed for adjustments, e.g. when the setup is still experimental and everything is not yet fully remotely controllable as later required in the tunnels. Equipment in the tunnels is very difficult to access: no access is possible during beam operation, only very limited temporary access is granted for urgent repairs, and longer access is only possible during a few shutdown periods per year. More importantly, conclusive tests of diagnostics functionality can be performed only with the actual photon beam of the European XFEL because the beam properties of our facility in their combination are unique in the world: short wavelength in the X-ray domain at high instantaneous brilliance (10^{12} photons per pulse of fs-domain pulse duration) and high average brilliance thanks to the MHz intra-bunch train repetition rate. The range of diagnostics instrumentation that is developed and needs characterization is broad.

The following are examples of diagnostics development projects that would improve by reliable development access to European XFEL beam in the SXP experiment hutch.

5.1.1 Gas-based ToF online monitors

Due to the pulse structure of the European XFEL and the resulting high heat load during pulse-trains, any online monitor has to withstand these extreme conditions, and thus gas target are most suitable. Basic beam parameters, such as the pulse energy and the beam position, are delivered by the routine diagnostics of the European XFEL, but gas-based monitoring of advanced parameters such as temporal, spectral, and coherence properties need further investigation.

5.1.2 Solid state detector diagnostics

The idea is to use detectors based on solid state materials, such as diamond detectors for intensity and beam position monitoring. The project builds on developments done for the baseline experiments at the European XFEL [249]. In Figure 5.1, a solid state detector based on a diamond scintillator with graphite electrodes is displayed.

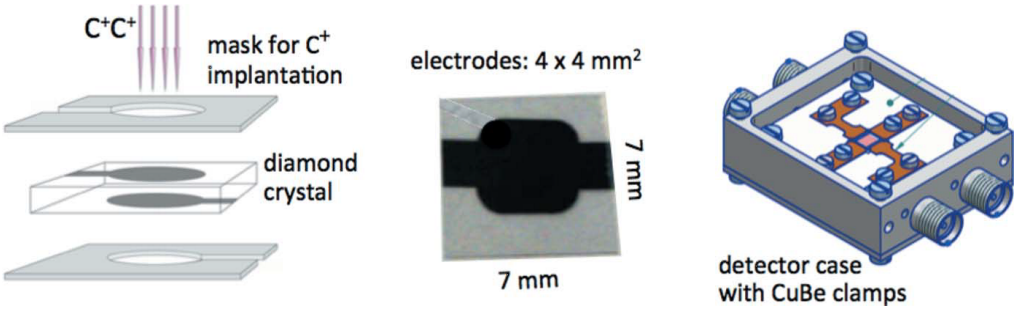

Figure 5.1: A diamond detector with graphite electrodes, as developed by XPD at the European XFEL

5.1.3 Fast imaging diagnostics with gated cameras

The idea of this project is to optimize the performance of the currently installed imagers to be able to resolved intra-pulse trains and also be able to perform pulse-resolved wavefront detection. The most promising possibility is the use of gate cameras (Figure 5.2 on the facing page).

As a part of the project, scintillator studies for high-repetition rate applications will be investigated. The idea is to realize/optimize scintillator materials with fast decay and high heat resistive load [250].

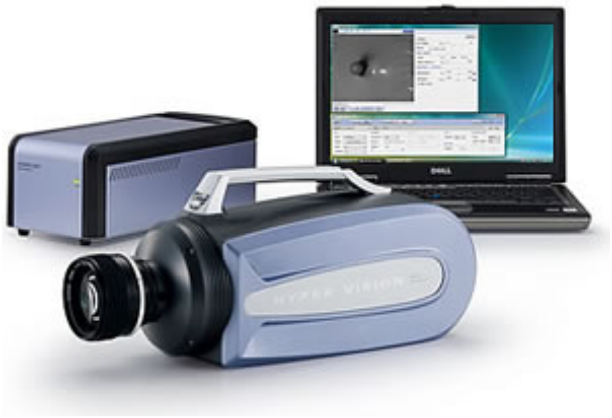

Figure 5.2: Gated camera for fast imaging detection

5.1.4 Wavefront sensing with soft X-rays

The idea of the project is to use the soft X-rays at SXP to characterize the performance of a wavefront sensor. The development aims at both the optimization of Hartmann plates and/or phase gratings. They will be used to characterize the source, the X-ray optics, and focus at selected positions as indicated in on the next page.

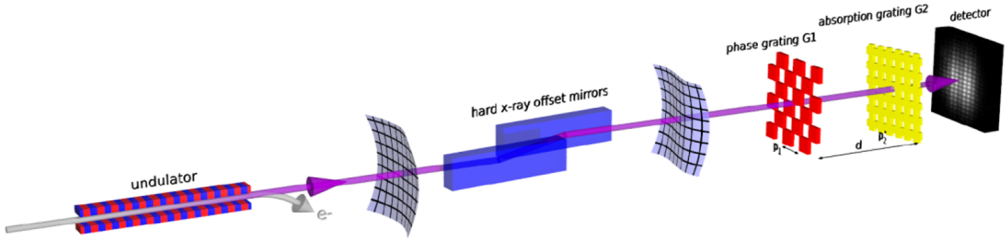

Figure 5.3: Sketch of a wavefront sensing phase grating

5.1.5 Diagnostics for temporal properties of ultrashort pulses

This project aims to use the attosecond streaking techniques using interaction of polarized optical laser beams with X-ray ionized gas ensembles and detection via momentum-resolving imaging or ToF spectroscopy. These studies could be carried out at the PES diagnostics tool (Cookie Box) that has been considered as one of the SXP permanent beamline components.

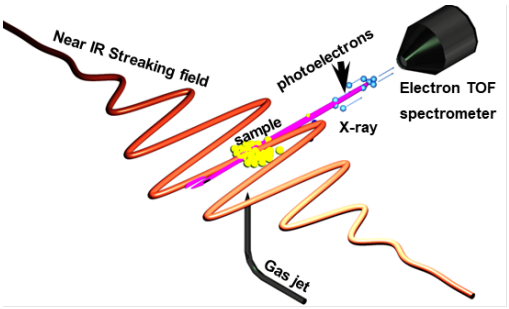

Figure 5.4: Sketch of attosecond streaking using THz excitation

5.2 Photoemission for analysis of X-rays: PAX

This technique uses photoelectron spectroscopy as a way to analyse the scattered X-rays produced by a sample excited with X-rays. The technique is sensitive to both elastic and inelastic scattered radiation. Therefore, the analysis of the data will produce resonant inelastic X-ray scattering (RIXS) spectra.

Initially proposed in the 1960s, it has been tested at LCLS [251]. It proposes an alternative to the standard RIXS configuration that uses a grating to do the energy analysis of the scattered light. The principle of the technique is sketched in Figure 5.5 on the facing page. X-rays shine on the sample under study from which one part is reflected, one part is absorbed, and the rest is scattered. When soft X-rays are used, the reflected contribution will be very weak for large angles between the incoming X-rays and the scattered light. The absorbed radiation will produce photoelectrons, Auger electrons, and fluorescence. The scattered radiation will contain both elastic and inelastic contributions. To isolate the scattered radiation a filter will be placed between the sample and the converter to absorb all electrons produced in the sample.

In order to obtain the inelastic X-ray spectrum, the scattered radiation is sent into a converter sample with well-known properties. The interaction with the scattered radiation will produce photoelectrons that are analysed with an angle-resolved photoelectron (ARPES) spectrometer. A feature of the converter, either a core level or the Fermi level, will be measured with the ARPES analyser. The presence of inelastic scattered light will induce modifications in the spectrum with respect to the direct photoemission measurement of the same feature. The deconvolution of the spectra will provide the desired RIXS spectra. Alternatively, a fit with the number of components can be performed. However, this requires some preliminary information regarding the sample. A combination of the two with a well-known sample can be used to define the deconvolution strategy.

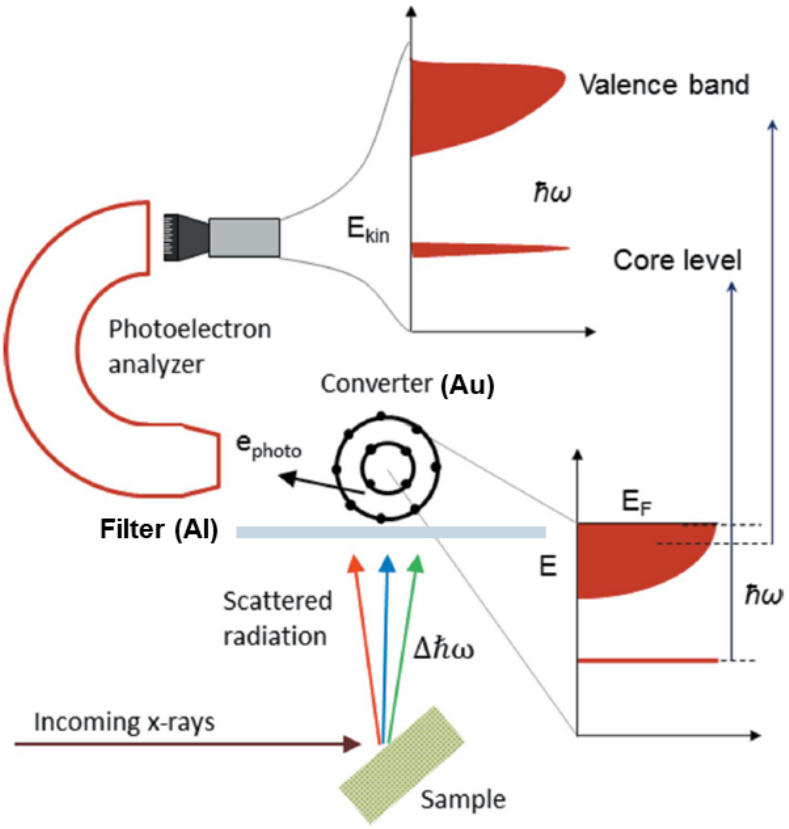

Figure 5.5: Sketch of the PAX experimental configuration. A converter sample in focus with a photoelectron analyser is placed in front of the sample under investigation. The scattered radiation will modify the photoemission spectra. Using a deconvolution process, the RIXS spectra can be obtained.

In Figure 5.6 on the next page, the results obtained at the SXR experiment of LCLS for a CoO sample are reported. The measurements were done at the Co L_3 resonance at 778 eV with a bandwidth of 260 meV provided by the beamline monochromator with a resolving power around 3000. A VG Scienta R3000 ARPES spectrometer was used to measure the PES spectra of the Au converter. The changes in the photoemission spectra in the Au 4*f* region were used to determine the RIXS spectra. Prior to the PAX experiment, the direct photoemission of the Au 4*f* levels at different pulse energies was measured in order to determine the fluence range in which no distortion of the spectra would occur, Figure 5.6 on the following page(a). A curve fitting of the 4*f* spectrum was done that served to confirm the bandwith. After this determination, the PAX experiment was carried out by placing the CoO sample under the X-rays and subsequently measure the spectra of the core level produced by the scattering radiation on the Au 4*f* being used a sample target. The photon energy was changed across the L_3 resonance to be able to construct the RIXS spectra as a function of the photon energy. In Figure 5.6 on the next page(b) and (c),

examples at two different excitation energies showing the modifications induced due to the inelastic wavelengths is displayed. Finally, in Figure 5.6(d), the RIXs spectra across the resonance are displayed. The data have been analysed using a fitting procedure with 12 components. This was possible thank to the well-known RIXS spectra of the CoO edge.

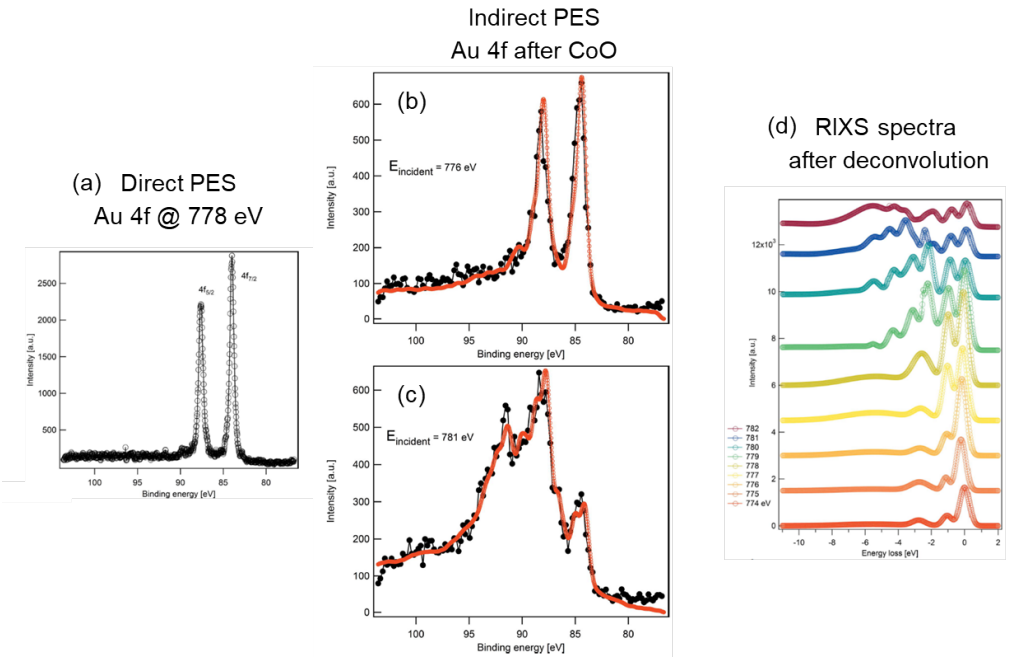

Figure 5.6: Results of a PAX experiment on a CoO sample using an Au target as converter: (a) The direct photoemission of the Au 4f is displayed. From the deconvolution the linewidth an experimental resolution can be deduced. (b)–(c) Examples of the modification of the Au 4f spectra at different excitation energies due to the inelastic scattered radiation coming from the sample. (d) RIXS spectra as a function of the photon energy resulting from the measured spectra. A fitting with 12 components was done. Alternatively a deconvolution can be realized.

In order to justify the development of the technique, a comparison was made with data measured with a conventional RIXS spectrometer that uses a grating to do the energy analysis. The main advantage of PAX with respect to conventional RIXS is that the spot size can be made larger. Typical values with a grating spectrometer are 15 x 500 μm^2. The asymmetric beam size is required for energy resolution purposes. In the case of PAX, the beamsize can be relaxed to 900 x 900 μm^2, yielding results with the same resolution. This size is more than 100 times larger, which results in a effective reduction of the fluence that will be beneficial for many samples. Other advantage arises from the more compact experimental setup required.

The proof of principle done at LCLS has demonstrated the interest in developing the technique further. It would also be ideally exploited at the European XFEL due

to the MHz repetition rates. Improvements of the initial proposition could be done in many directions: (i) Use an optimized photoelectron spectrometer. (ii) Replace the electron filter by a grid with a potential to repel electrons, etc. The development of the technique would benefit from the SXP access that could eventually done parasitically to other experiment preparation.

A SASE3 source parametrization

Table A.1 on page 137 lists the source parametrization coefficients for the updated electron energies. The new working points of the SASE radiators compensate for the changes in the undulator K parameter. The source parametrization is defined as follows.

The source size, pulse energy, and bandwidth (full width at half maximum, FWHM) are empirically given by

$$\begin{aligned} S_{\mathrm{FWHM}} &= s_1 \cdot \ln(s_2 \cdot \lambda[\mathrm{nm}]) \\ E_{\mathrm{pulse}} &= e_1 \cdot \ln(e_2 \cdot \lambda[\mathrm{nm}]) \\ (\Delta\omega/\omega)_{\mathrm{FWHM}} &= w_1 \cdot \ln(w_2 \cdot \lambda[\mathrm{nm}]), \end{aligned} \tag{A.1}$$

where the dependence of the coefficients on the bunch charge is modeled according to

$$\begin{aligned} s_1 &= s_{10} + s_{11} \cdot c[\mathrm{nC}] \quad \text{and} \quad s_2 = s_{20} \cdot \exp\left[(\,] - s_{21} \cdot c[\mathrm{nC}]\right) \\ e_1 &= e_{10} + e_{11} \cdot c[\mathrm{nC}] \quad \text{and} \quad e_2 = e_{20} \cdot \exp\left[(\,] - e_{21} \cdot c[\mathrm{nC}]\right) \\ w_1 &= w_{10} \approx \text{const.} \quad \text{and} \quad w_2 = w_{20} \cdot \exp\left[(\,] - w_{21} \cdot c[\mathrm{nC}]\right). \end{aligned} \tag{A.2}$$

The source divergence (FWHM) is fitted using

$$\delta\theta = \theta_0 + \theta_1 \cdot \lambda^{2/3}, \tag{A.3}$$

where the dependence of the coefficients on the bunch charge is modeled according to

$$\theta_0 = \theta_{00} \approx \text{const.} \quad \text{and} \quad \theta_1 = \theta_{10} - \theta_{11} \cdot (c[\mathrm{nC}])^{1/3}. \tag{A.4}$$

Table A.1: SASE3 source parametrization coefficients. The 8.5 and 12 GeV SASE3 operation modes are added to the other two baseline operation modes (14 and 17.5 GeV).

Operation mode	**8.5 GeV**	**12.0 GeV**	**14.0 GeV**	**17.5 GeV**
s_{10}	3.7	3.5	3.8	3.5
s_{11}	5.0	4.2	3.4	2.9
s_{20}	1.87×10^4	3.67×10^4	4.562×10^4	6.151×10^4
s_{21}	-1.36	-1.84	-2.09	-1.90
e_{10}	-0.04	-0.14	0.00	-0.01
e_{11}	2.1	3.1	2.5	3.0
e_{20}	15.80	28.49	34.84	45.60
e_{21}	-0.40	-1.16	-1.31	-1.54
w_1	0.12	0.10	0.09	0.09
w_{20}	30.1	51.8	65.1	68.0
w_{21}	-0.764	-0.616	-0.542	-0.360
θ_0	-3.2	-2.3	-2.1	-1.3
θ_{10}	14.6	14.9	15.0	14.6
θ_{11}	-3.96	-4.37	-4.42	-4.36

B Operation modes

B.1 European XFEL accelerator operation modes

The operation modes of the SXP instrument will derive from the injection modes available at the machine modes. Due to the double modulation frequency of the pulses with 4.5 MHz bursts and a maximum of 2700 pulses running at 10 Hz, four operation modes are foreseen, as indicated in Table B.1 on page 138. They differ in the maximum number of pulses allowed, which will depend on the bunch current.

Table B.1: Definition of the proposed beam modes. The numbers indicate the maximum number of allowed pulses within one pulse train. Modes highlighted in green were proposed for the accelerator, while the others are additionally proposed for the X-ray beamlines. The current use of the accelerator does not foresee the use of bunch charges larger than 0.5 nC.

Mode/charge	0.1 nC	0.25 nC	0.5 nC	> 1 nC
Mode 1	1	1	1	1
Mode S	600	200	30	1
Mode M	2700	1350	200	10
Mode F	2700	2700	< 2700	< 2700

The foreseen operation modes have been proposed either by the “accelerator team”, the “X-ray optics and beam transport group”, or the “instruments”, aiming the commissioning in the first case and the possibility to access particular types of experiments.

The intended use of each mode is described below:

- **Mode 1**
  Basic commissioning mode of the accelerator, beam transport, and experiments. With one pulse per pulse train (10 Hz operation), even a miss-steered beam should not be able to destroy components of the beam transport.

- **Mode S**
  Basic commissioning mode of the accelerator with pulse trains (30 pulses). For the beam transport, it has been proposed to make

this mode charge-dependent, so it can be used to run experiments with a diamond window in air at the Femtosecond X-Ray Experiments (FXE) instrument and the Materials Imaging and Dynamics (MID) instrument.

- **Mode M**
  This mode is requested from the optics and beam transport group. It is essentially defined by the number of pulses that a water-cooled piece of B_4C can absorb without being damaged. Also, the hard X-ray monochromator and beryllium lenses work only up to Mode M.

- **Mode F**
  Full beam. The beam power is limited only by the performance of the accelerator and the electron beam dumps. Typically, only the total reflecting mirrors can handle this beam power. X-ray beam loss monitors have to be operational and fully commissioned to reach this mode.

C SASE3 upgrades under study

C.0.1 Self-seeding

The SASE FEL radiation is characterized by a relatively large bandwidth. As discussed in Section 1.2.1 on page 13, the bandwidth of the radiation is proportional to Pierce parameter $\rho \sim \Delta\lambda/\lambda$. Its typical value in the soft X-ray regime is $\sim 10^{-3}$. In order to reduce the bandwidth without reducing the radiated power, several strategies have been developed. Besides the harmonic lasing self-seeding (HLSS, see Section 1.2.1 on page 13), other strategies have been developed over the years [252; 253; 254]. From all the them, self-seeding will be implemented at the European XFEL: hard X-ray self-seeding is currently being implemented in the SASE2 undulator system. Soft X-ray self-seeding in the SASE3 undulator system is currently not funded. A possible way to implement the project could be to couple it with the two-colour pulse generation project described in Section 1.2.3 on page 18. Some technical challenges regarding the installation of the monochromating grating in the delay mirror unit would need to be solved.

In the following, the implementation of soft X-ray self-seeding at SASE3 is discussed based on the successful implementation at the SXR instrument at LCLS [255]. The concept follows the initial theoretical proposition [256] and detailed study for LCLS [257]. The European XFEL implementation could be realized by removing one undulator section, U7, and two quadrupoles of the FODO lattice, total length 7.2 m, and installing in their place an electron chicane and a soft X-ray monochromatic system [258]. The scheme within the SASE3 undulator system is shown at the top of Figure C.1 on page 141, and the detailed configuration of the electron chicane and the monochromating system is shown in the enlarged inset at the bottom of Figure C.1 on page 141. The displayed configuration has been designed taking into account acceleration operation at energies up to 12 GeV and self-seeding operation between 0.3 and 1.2 KeV. The undulator section, U7, and the idea of keeping U6 open have been done to optimize the mentioned conditions. In particular, the selection will ensure the covering of the full photon energy range, ensure the optimal refocusing of the source, and ensure that the monochromating system will not be over-illuminated, which could result in a degradation of performance.

The monochromating system is made of five elements: a variable line spacing (VLS) toroidal grating, three mirrors, and an exit slit. In contrast to a classical monochromating system, no entrance slit is required due to the coherence properties

of the beam. The first element will be the grating with a resolving power 7000–9400 between 600 and 1200 eV, followed by a plane mirror that will reflect the desired wavelength on the exit slit. The latter is followed by a toroidal mirror to refocus the monochromatic beam. The last mirror will be used to reflect the beam into the seeded undulator system and will dispose of the degrees of freedom to make a good overlap with the electron beam propagating in the electron chicane. The introduction of the monochromating system will result in a wavelength-dependent time delay. This delay will be compensated by the electron magnetic chicane. Besides this time compensation, required to overlap electron and monochromatic photons, the chicane will wash out the micro-bunching consequence of the lasing in the first undulator section, create a transverse offset to introduce the monochromating system, and compensate for the electron phase mismatch due to the absence of one undulator section.

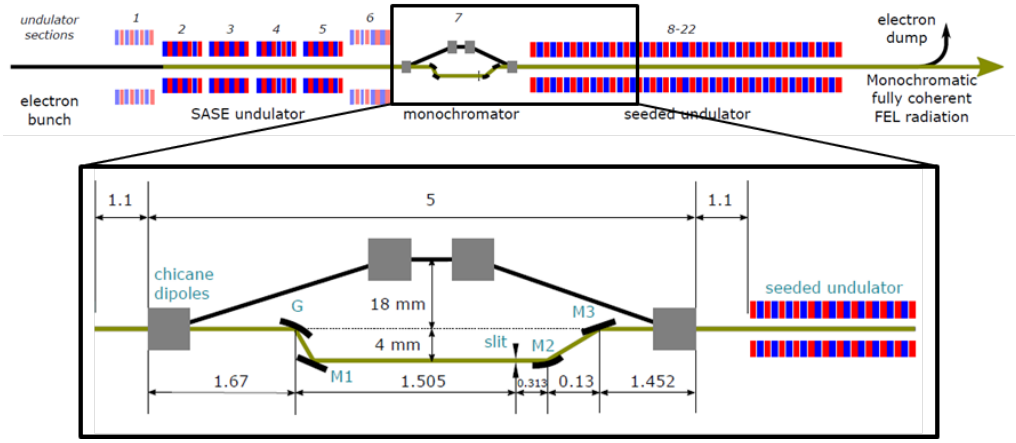

Figure C.1: Soft X-ray self-seeding scheme to be implemented at the SASE3 undulator system. The geometrical distance of the different components is indicated.

The described implementation of self-seeding is expected to result in at least a factor of 20 bandwidth reduction, as observed at the SXR experiment at LCLS. The output power can be optimized using tapering techniques [258].

C.0.2 Attosecond pulse generation

One more project under development, in particular at SASE3, is the generation of attosecond pulses. The motivation derives from the recent achievements obtained with optical laser high harmonic generation. At FELs, several propositions have been made in order to produce the attosecond pulses. They use a combination of spoiler foil, optical lasers, and magnetic chicanes. The most efficient technique proposed

is “X-ray laser enhanced attosecond pulse generation” (XLEAP) and uses the three mentioned elements [259]. Simulations for SASE3 at the European XFEL have been recently performed [260]. A sketch of the implementation is provided in Figure C.2 on page 142. A fraction of the electron bunch of a few micrometers produced in the injector is selected from the original bunch with an emittance spoiler film placed in the second bunch compressor, BC2. At the exit of the linear accelerator (LINAC), the electrons enter an undulator section (modulator), where they interact with a picosecond optical laser with the same wavelength as the undulator period length. The electrons experience a sinusoidal energy modulation, $\Delta\gamma \sim 1 \cdot 10^{-4} \cdot \sqrt{(2P_{las}N_m)}$, where P_{las} is the laser power and N_m the number of undulator periods. At the exit of the modulator, they enter a magnetic chicane, where dispersion transforms the energy modulation into a density modulation. The initial electron distribution will be seen in the undulator as a series of sub-femtosecond spikes separated by the wavelength of the optical laser. The number of spikes will depend on the length of the electron beam after the spoiler. They will lase attosecond pulses with a wavelength defined by the undulator parameters.

The generation of attosecond pulses at the European XFEL has been studied assuming an electron acceleration energy of 8.5 GeV and an electron charge of 500 pC. The electron acceleration energy has been chosen to be the lowest operating point in order to get the most efficient energy modulation possible. A pulse duration between 300 and 500 attoseconds is expected in the photon energy range from 2.3 to 0.6 KeV. The repetition rate will be limited to the repetition rate of the optical laser used, currently limited to the kHz regime. An alternative possibility to produce attosecond pulses instead of using an optical laser is to employ the coherent infrared radiation emitted by the tail of the electron beam in the wiggler. This improved XLEAP technique has been successfully implemented at LCLS [261].

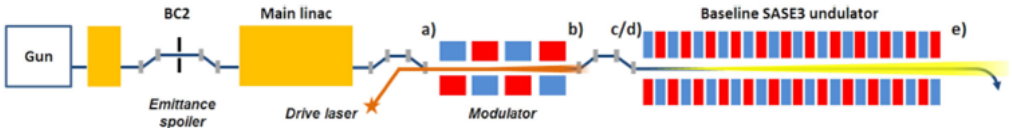

Figure C.2: Scheme of the XLEAP implementation at the European XFEL. Attosecond pulses below 0.5 fs will be produced.

C.0.3 X-ray beam split and delay unit

In order to extend the capabilities of X-ray pump and X-ray probe experiments at the European XFEL, an X-ray beam split and delay (XBSD) unit will be installed in the X-ray optics transport system. The optical system will be able to operate with

SASE mode or in combination with any of the other schemes previously described. Besides them, the possibility of combining the zero order and the first order of the monochromator has been studied. The conceptual design has been developed by the Spectroscopy and Coherent Scattering (SCS) group [262]. It is based on an wavefront division beam splitter with asymmetric geometry using a fixed and a variable delay in different mirror planes.

The position of the XBSD has been defined, based on the position of the soft X-ray monochromator and the position and spacing between the beam stops of the diffraction orders not used by the experiment (normally the first one). It will be placed in between beam dumps of the third and fourth order, at a distance of 8 m from the monochromator. The maximum length for the XBSD tank will be 8 m and is defined by the space between the third and fourth diffraction order beam dumps.

The scheme of the optical system is displayed in Figure C.3 on page 144. The location, space constraints, and footprint of the beam at this position has shaped the geometrical configuration. The mirrors will be made of B_4C and will work with an 20 mrad incidence angle to clip the beam as little as possible. In order to cover the whole energy range, a stripe with metallic coating will be used. The incident X-ray beam will be split by mirror SM1 in two halves: one part will be deflected downwards, following the optical path defined by SM1–SM2–SM3–SM4. This path will propagate in the vertical direction and will be fixed. The second half of the beam will be horizontally deflected and will propagate through DM1–DM2–DM3–DM4. The change in the optical path and therefore the time delay will be done by moving mirrors DM2 and DM3. The two mirrors, independently movable, will be mounted on a movable stage. This will allow both longitudinal and transversal movement. The first one, ensured by the mirror movement, will serve to change the delay range. The transversal movement, affecting the whole stage, will be used to select a given delay within the allowed range. The conceptual designs foresees that a combination of the two motions will allow a 12–13 ps delay range.

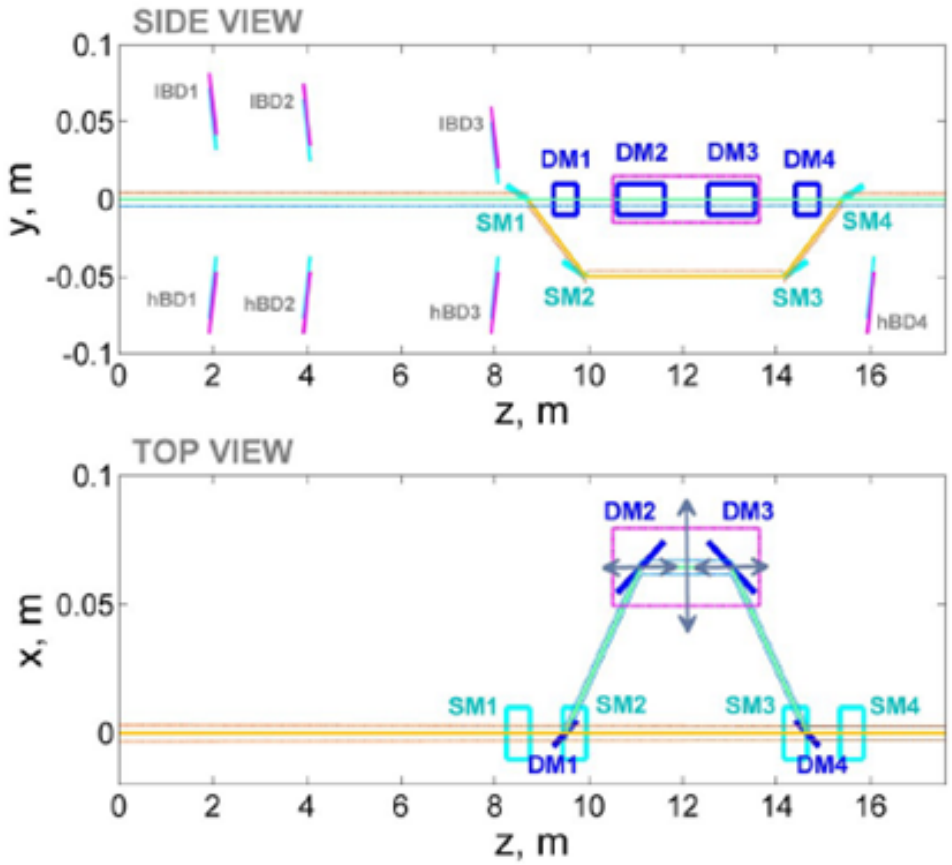

Figure C.3: Scheme of the XBSD unit implementation in the SASE3 X-ray optics tunnel

D Note on contributions

Besides the authors of the different chapters and/or sections included in this report, we would like to outline the contribution of many experts of the European XFEL. These are:

- **Chapter 1, "Introduction"**
  To Evgeny A. Shneydmiller and Mikhail. V. Yurkov for their calculation of the source parameters, developing and testing high harmonics laser self-seeded FEL strategy, reverse tapering, etc. To Joachim Pflueger, Suren Karabekyan, and Yuhui Li for the baseline undulator system and their work on the Apple X undulator for variable polarization. To Gianluca Geloni and Svitozar Serkez for their work on self-seeding, two-coloru experiments, and attosecond generation. To A. Yaroslatsev and A. Scherz from the Spectroscopy and Coherent Scattering (SCS) experiment for the design of a versatile X-ray beam split and delay line that will allow using the full potential of the SASE3 radiation.

- **Whole report**
  To Kurt Ament, whose editing precision and skills have significantly improve the quality of this document.

E Acknowledgements

This report could not have been possible without the European XFEL collaboration that has built the most sophisticated FEL there is. It builds on the technical developments and achievements realized in the facility so far. For this reason, the SXP group would like to thank European and all colleagues for providing a very interesting and motivating working environment. We would also like to thank the already identified SXP scientific community for supporting the project with their contributions. We would also like to thank very many interesting discussions with E.A. Schneidmiller, M. Yurkov, G. Geloni, and S. Serkez for the interesting discussions in the various new schemes they have developed for SASE3. We also thank Harald Sinn, Liubov Samoyloba, Maurizio Vannoni, and Daniele La Civita for many discussions on X-ray optics and mechanics, for SXP but not only that. To T. Mazza for sharing his OASYS code of the SASE3 X-ray optics transport and the KB mirror parameters. To Kurt Ament for the discussions on editing, publication policies, and strategies. I would like to thank Michael Meyer and Andreas Scherz, leading scientists of SQS and SCS, for the interesting discussions on the project. Finally, I would like to thank the European XFEL management board: N. Elleuche, R. Feindhans'l, T. Tschentcher, S. Pascarelli and S. Molodtsov, for their support to the SXP project.

Bibliography

[1] T. Tschentscher, C. Bressler, J. Grünert, et al.: “Photon Beam Transport and Scientific Instruments at the European XFEL”, Applied Sciences **7** (2017) doi:10.3390/app7060592

[2] S. Liu, R. Boll, F. Brinker, et al.: “Parallel Operation of SASE1 and SASE3 at the European XFEL”, Hamburg, Germany, Proc. FEL’19, Free Electron Laser Conference 39, 25–28 (JACoW Publishing, Geneva, Switzerland 2019) doi:10.18429/JACoW-FEL2019-TUA01

[3] L. Fröhlich, A. Aghababyan, V. Balandin, et al.: “Multi-Beamline Operation at the European XFEL”, Hamburg, Germany, Proc. FEL’19, Free Electron Laser Conference 39, 335–338 (JACoW Publishing, Geneva, Switzerland 2019) doi:10.18429/JACoW-FEL2019-WEP008

[4] E. A. Schneidmiller, M. V. Yurkov: “Photon beam properties at the European XFEL”, Technical Report (2011) doi:10.3204/DESY11-152

[5] A. Scherz, O. Krupin, J. Buck, et al.: “Conceptual Design Report: Scientific Instrument Spectroscopy and Coherent Scattering (SCS)”, XFEL.EU TR-2013-006 (2013), pp. 1–147 doi:10.3204/XFEL.EU/TR-2013-006

[6] B. W. J. McNeil, G. R. M. Robb, M. W. Poole, et al.: “Harmonic Lasing in a Free-Electron-Laser Amplifier”, Phys. Rev. Lett. **96**, 084801 (2006) doi:10.1103/PhysRevLett.96.084801

[7] E. A. Schneidmiller, M. V. Yurkov: “Harmonic lasing in x-ray free electron lasers”, Phys. Rev. ST Accel. Beams **15**, 080702 (2012) doi:10.1103/PhysRevSTAB.15.080702

[8] E. A. Schneidmiller, B. Faatz, M. Kuhlmann, et al.: “First operation of a harmonic lasing self-seeded free electron laser”, Phys. Rev. Accel. Beams **20**, 020705 (2017) doi:10.1103/PhysRevAccelBeams.20.020705

[9] E. L. Saldin, E. A. Schneidmiller, M. V. Yurkov: “Properties of the third harmonic of the radiation from self-amplified spontaneous emission free electron laser”, Phys. Rev. ST Accel. Beams **9**, 030702 (2006) doi:10.1103/PhysRevSTAB.9.030702

[10] E. A. Schneidmiller, F. Brinker, W. Decking, et al.: “Observation of harmonic lasing in the Angstrom regime at European X-ray Free Electron Laser”, Phys. Rev. Accel. Beams **24**, 030701 (2021) doi:10.1103/PhysRevAccelBeams.24.030701

[11] A. A. Lutman, J. P. MacArthur, M. Ilchen, et al.: “Polarization control in an X-ray free-electron laser”, Nature Photonics **10**, 468 (2016) doi:10.1038/nphoton.2016.79

[12] T. Wei, P. Li, Y. Li, et al.: “The Apple-X undulator for the European XFEL SASE3 afterburner” (2017)

[13] T. Wei, P. Li, Y. Li, et al.: “Radiation properties of the SASE3 afterburner for European XFEL” (2017)

[14] E. A. Schneidmiller, M. V. Yurkov: “Obtaining high degree of circular polarization at x-ray free electron lasers via a reverse undulator taper”, Phys. Rev. ST Accel. Beams **16**, 110702 (2013) doi:10.1103/PhysRevSTAB.16.110702

[15] G. Geloni, V. Kocharyan, T. Mazza, et al.: “Opportunities for Two-color Experiments at the SASE3 undulator line of the European XFEL”, arxiv:1706.00423 (2017)

[16] S. Hüfner: *Photoelectron Spectroscopy: Principles and Applications* (Springer 2003)

[17] C. Fadley: “X-ray photoelectron spectroscopy: Progress and perspectives”, Journal of Electron Spectroscopy and Related Phenomena **178-179**, 2–32 (2010) doi:10.1016/j.elspec.2010.01.006

[18] J. Feng, A. Scholl: “Photoemission Electron Microscopy”, in: P. W. Hawkes, J. C. H. Spence (eds.): *Springer Handbook of Microscopy*, 2–2 (Springer International Publishing, Cham 2019) doi:10.1007/978-3-030-00069-1_10

[19] C. Broholm, *et al.*: “Basic Research Needs Workshop on Quantum Materials for Energy Relevant Technology” (2016)

[20] N. Gedik, I. Vishik: “Photoemission of quantum materials”, Nature Physics **13**, 1029 (2017) doi:10.1038/nphys4273

[21] M. Salmeron, R. Schlögl: “Ambient pressure photoelectron spectroscopy: A new tool for surface science and nanotechnology”, Surface Science Reports **63**, 169–199 (2008) doi:https://doi.org/10.1016/j.surfrep.2008.01.001

[22] J. Fujii, M. Sperl, S. Ueda, et al.: “Identification of Different Electron Screening Behavior Between the Bulk and Surface of (Ga,Mn)As”, Phys. Rev. Lett. **107**, 4 (2011) doi:10.1103/PhysRevLett.107.187203

[23] T. Pincelli, V. Lollobrigida, F. Borgatti, et al.: “Quantifying the critical thickness of electron hybridization in spintronics materials”, Nat. Commun. **8** (2017) doi:10.1038/ncomms16051

[24] M. Izquierdo, M. E. Dávila, J. Avila, et al.: “Epitaxy and Magnetic Properties of Surfactant-Mediated Growth of bcc Cobalt”, Phys. Rev. Lett. **94**, 187601 (2005) doi:10.1103/PhysRevLett.94.187601

[25] O. Fedchenko, K. Medjanik, S. Chernov, et al.: “4D texture of circular dichroism in soft-x-ray photoemission from tungsten”, New Journal of Physics **21**, 013017 (2019) doi:10.1088/1367-2630/aaf4cd

[26] E. Bauer: “LEEM, SPLEEM and SPELEEM”, in: P. W. Hawkes, J. C. H. Spence (eds.): *Springer Handbook of Microscopy*, 2–2 (Springer International Publishing, Cham 2019) doi:10.1007/978-3-030-00069-1_9

[27] X. M. Cheng, D. J. Keavney: “Studies of nanomagnetism using synchrotron-based x-ray photoemission electron microscopy (X-PEEM)”, Reports on Progress in Physics **75**, 026501 (2012) doi:10.1088/0034-4885/75/2/026501

[28] S.-H. Yang, B. Mun, A. Kay, et al.: “Depth-resolved photoemission spectroscopy from surface and buried layers with soft X-ray standing waves”, Surface Science **461**, L557–L564 (2000) doi:https://doi.org/10.1016/S0039-6028(00)00617-8

[29] A. X. Gray: “Future directions in standing-wave photoemission”, Journal of Electron Spectroscopy and Related Phenomena **195**, 399–408 (2014) doi:10.1016/j.elspec.2014.05.004

[30] S. Nemk, A. Shavorskiy, O. Karslioglu, et al.: “Concentration and chemical-state profiles at heterogeneous interfaces with sub-nm accuracy from standing-wave ambient-pressure photoemission”, Nature Communications **5** (2014) doi:10.1038/ncomms6441

[31] J. Vogel, W. Kuch, M. Bonfim, et al.: “Time-resolved magnetic domain imaging by x-ray photoemission electron microscopy”, Applied Physics Letters **82**, 2299–2301 (2003) doi:10.1063/1.1564876 eprint: https://doi.org/10.1063/1.1564876

[32] S.-B. Choe, Y. Acremann, A. Scholl, et al.: “Vortex Core-Driven Magnetization Dynamics”, Science **304**, 420–422 (2004) doi:10.1126/science.1095068 eprint: https://science.sciencemag.org/content/304/5669/420.full.pdf

[33] J. Raabe, C. Quitmann, C. H. Back, et al.: “Quantitative Analysis of Magnetic Excitations in Landau Flux-Closure Structures Using Synchrotron-Radiation Microscopy”, Phys. Rev. Lett. **94**, 217204 (2005) doi:10.1103/PhysRevLett.94.217204

[34] J. Schmidt, A. Guggenmos, S. H. Chew, et al.: “Development of a 10 kHz high harmonic source up to 140 eV photon energy for ultrafast time-, angle-, and phase-resolved photoelectron emission spectroscopy on solid targets”, Review of Scientific Instruments **88**, 083105 (2017) doi:10.1063/1.4989399 eprint: https://doi.org/10.1063/1.4989399

[35] M. Bridger, O. A. Naranjo-Montoya, A. Tarasevitch, et al.: “Towards high power broad-band OPCPA at 3000 nm”, Opt. Express **27**, 31330–31337 (2019) doi:10.1364/OE.27.031330

[36] T. Popmintchev, M.-C. Chen, D. Popmintchev, et al.: “Bright Coherent Ultrahigh Harmonics in the keV X-ray Regime from Mid-Infrared Femtosecond Lasers”, Science **336**, 1287–1291 (2012) doi:10.1126/science.1218497

[37] R. Schoenlein, T. Elsaesser, K. Holldack, et al.: “Recent advances in ultrafast X-ray sources”, Philosophical Transactions of the Royal Society A: Mathematical, Physical and Engineering Sciences **377**, 20180384 (2019) doi:10.1098/rsta.2018.0384

[38] M. Dell'Angela, T. Anniyev, M. Beye, et al.: "Vacuum space charge effects in sub-picosecond soft X-ray photoemission on a molecular adsorbate layer", Structural Dynamics **2**, 025101 (2015) doi:10.1063/1.4914892 eprint: https://doi.org/10.1063/1.4914892

[39] M. Wagstaffe, L. Wenthaus, A. Dominguez-Castro, et al.: "Ultrafast Real-Time Dynamics of CO Oxidation over an Oxide Photocatalyst", ACS Catalysis **10**, 13650–13658 (2020) doi:10.1021/acscatal.0c04098

[40] F. Roth, M. Borgwardt, L. Wenthaus, et al.: "Direct observation of charge separation in an organic light harvesting system by femtosecond time-resolved XPS", Nature Comm. **12**, 1196 (2021) doi:10.1038/s41467-021-21454-3

[41] D. Curcio, S. Pakdel, K. Volckaert, et al.: "Ultrafast electronic linewidth broadening in the C 1*s* core level of graphene", Phys. Rev. B **104**, L161104 (2021) doi:10.1103/PhysRevB.104.L161104

[42] S. Hellmann, T. Rohwer, M. Kallaene, et al.: "Time-domain classification of charge-density-wave insulators", Nat. Comm. **3**, 1069 (2012) doi:10.1038/ncomms2078

[43] S. Hellmann, M. Beye, C. Sohrt, et al.: "Ultrafast Melting of a Charge-Density Wave in the Mott Insulator $1T-TaS_2$", Phys. Rev. Lett. **105**, 187401 (2010) doi:10.1103/PhysRevLett.105.187401

[44] M. Eichberger, H. Schäfer, M. Krumova, et al.: "Snapshots of cooperative atomic motions in the optical suppression of charge density waves", Nature **468**, 799 (2010) doi:10.1038/nature09539

[45] L.-I. team: "New science oportunities enabled by LCLS-II X-ray lasers" (2015)

[46] G. Admans, P. Berkvens, A. Kaprolat, et al. (eds.): "ESRF Upgrade programme phase II" (2011)

[47] G. A. Mourou, G. Korn, W. Sandner, et al. (eds.): "Science and Technology with Ultra-Intense Lasers" (2011)

[48] D. J. Hilton, R. P. Prasankumar, S. A. Trugman, et al.: "On Photo-Induced Phenomena in Complex Materials: Probing Quasiparticle Dynamics using Infrared and Far-Infrared Pulses", Journal of the Physical Society of Japan **75**, 011006 (2006) doi:10.1143/JPSJ.75.011006

[49] R. Schoenlein, *et al.*: "New Science Opportunities Enabled by LCLS-II X-Ray Lasers" (2015)

[50] T. Heinz, *et al.*: "Opportunities for Basic Research at the Frontiers of XFEL Ultrafast Science" (2017)

[51] P. B. Allen: "Theory of thermal relaxation of electrons in metals", Phys. Rev. Lett. **59**, 1460–1463 (1987) doi:10.1103/PhysRevLett.59.1460

[52] E. Beaurepaire, J.-C. Merle, A. Daunois, et al.: "Ultrafast Spin Dynamics in Ferromagnetic Nickel", Phys. Rev. Lett. **76**, 4250–4253 (1996) doi:10.1103/PhysRevLett.76.4250

[53] S. Gerber, S.-L. Yang, D. Zhu, et al.: “Femtosecond electron-phonon lock-in by photoemission and x-ray free-electron laser”, Science **357**, 71–75 (2017) doi:10.1126/science.aak9946

[54] L. H. Tjeng, B. Sinkovic, N. B. Brookes, et al.: “Spin-Resolved Photoemission on Anti-Ferromagnets: Direct Observation of Zhang-Rice Singlets in CuO”, Phys. Rev. Lett. **78**, 1126–1129 (1997) doi:10.1103/PhysRevLett.78.1126

[55] B. Sinkovic, L. H. Tjeng, N. B. Brookes, et al.: “Local Electronic and Magnetic Structure of Ni below and above T_C: A Spin-Resolved Circularly Polarized Resonant Photoemission Study”, Phys. Rev. Lett. **79**, 3510–3513 (1997) doi:10.1103/PhysRevLett.79.3510

[56] C. Stamm, J. U. Thiele, T. Kachel, et al.: “Antiferromagnetic-ferromagnetic phase transition in FeRh probed by x-ray magnetic circular dichroism”, Phys. Rev. B **77**, 184401 (2008) doi:10.1103/PhysRevB.77.184401

[57] F. Pressacco, V. Uhlír, M. Gatti, et al.: “Laser induced phase transition in epitaxial FeRh layers studied by pump-probe valence band photoemission”, Structural Dynamics **5**, 034501 (2018) doi:10.1063/1.5027809 eprint: https://doi.org/10.1063/1.5027809

[58] F. Pressacco, D. Sangalli, V. Uhlír, et al.: “Subpicosecond metamagnetic phase transition in FeRh driven by non-equilibrium electron dynamics”, Nature Comm. **12**, 5088 (2011) doi:10.1038/s41467-021-25347-3 eprint: https://doi.org/10.1038/s41467-021-25347-3

[59] A. Cavalleri, C. Tóth, C. W. Siders, et al.: “Femtosecond Structural Dynamics in VO_2 during an Ultrafast Solid-Solid Phase Transition”, Phys. Rev. Lett. **87**, 237401 (2001) doi:10.1103/PhysRevLett.87.237401

[60] C. W. Nicholson, A. Lücke, W. G. Schmidt, et al.: “Beyond the molecular movie: Dynamics of bands and bonds during a photoinduced phase transition”, Science **362**, 821–825 (2018) doi:10.1126/science.aar4183

[61] S. Wall, S. Yang, L. Vidas, et al.: “Ultrafast disordering of vanadium dimers in photoexcited VO2”, Science **362**, 572–576 (2018) doi:10.1126/science.aau3873

[62] P. Hansmann, A. Toschi, G. Sangiovanni, et al.: “Mott–Hubbard transition in V2O3 revisited”, physica status solidi (b) **250**, 1251–1264 (2013) doi:10.1002/pssb.201248476 eprint: https://onlinelibrary.wiley.com/doi/pdf/10.1002/pssb.201248476

[63] M. Izquierdo, M. Karolak, D. Prabhakaran, et al.: “Monitoring ultrafast metallization in $LaCoO_3$ with femtosecond soft x-ray spectroscopy”, Communications Physics **2**, 8 (2019) doi:10.1038/s42005-019-0109-9

[64] M. P. M. Dean, Y. Cao, X. Liu, et al.: “Ultrafast energy- and momentum-resolved dynamics of magnetic correlations in the photo-doped Mott insulator Sr_2IrO_4”, Nature Mater. **15**, 601 (2016) doi:/10.1038/nmat4641

[65] B. Keimer, J. E. Moore: “The physics of quantum materials”, Nature Physics **13**, 1045 (2017) doi:10.1038/nphys4302

[66] N. Samarth: “Quantum materials discovery from a synthesis perspective”, Nature Materials **16**, 1068–1076 (2017) doi:10.1038/nmat5010

[67] D. N. Basov, R. D. Averitt, D. Hsieh: “Towards properties on demand in quantum materials”, Nat. Mater. **16**, 1077 (2017) doi:10.1038/nmat5017

[68] Y. Tokura, M. Kawasaki, N. Nagaosa: “Emergent functions of quantum materials”, Nat. Phys. **13**, 1056 (2017) doi:10.1038/nphys4274

[69] J. Wang, S.-C. Zhang: “Topological states of condensed matter”, Nat. Mat. **16**, 1062 (2017) doi:10.1038/nmat5012

[70] Z. Yang, C. Ko, S. Ramanathan: “Oxide Electronics Utilizing Ultrafast Metal-Insulator Transitions”, Annual Review of Materials Research **41**, 337–367 (2011) doi:10.1146/annurev-matsci-062910-100347

[71] T. Kimura, Y. Otani, T. Sato, et al.: “Room-Temperature Reversible Spin Hall Effect”, Phys. Rev. Lett. **98**, 156601 (2007) doi:10.1103/PhysRevLett.98.156601

[72] K. Kondou, R. Yoshimi, A. Tsukazaki, et al.: “Fermi-level-dependent charge-to-spin current conversion by Dirac surface states of topological insulators”, Nat. Phys. **12**, 1027 (2016) doi:10.1038/nphys3833

[73] D. Xiao, G.-B. Liu, W. Feng, et al.: “Coupled Spin and Valley Physics in Monolayers of MoS_2 and Other Group-VI Dichalcogenides”, Phys. Rev. Lett. **108**, 196802 (2012) doi:10.1103/PhysRevLett.108.196802

[74] K. F. Mak, K. L. McGill, J. Park, et al.: “The valley Hall effect in MoS_2 transistors”, Science **344**, 1489–1492 (2014) doi:10.1126/science.1250140

[75] D. Fausti, R. I. Tobey, N. Dean, et al.: “Light-Induced Superconductivity in a Stripe-Ordered Cuprate”, Science **331**, 189–191 (2011) doi:10.1126/science.1197294

[76] W. Hu, S. Kaiser, D. Nicoletti, et al.: “Optically enhanced coherent transport in $YBa_2Cu_3O_{6.5}$ by ultrafast redistribution of interlayer coupling”, Nat. Mat. **13**, 705 (2014) doi:10.1038/nmat3963

[77] M. Mitrano, A. Cantaluppi, D. Nicoletti, et al.: “Possible light-induced superconductivity in K_3C_{60} at high temperature”, Nature **530**, 461 (2016) doi:10.1038/nature16522

[78] Y. H. Wang, H. Steinberg, P. Jarillo-Herrero, et al.: “Observation of Floquet-Bloch States on the Surface of a Topological Insulator”, Science **342**, 453–457 (2013) doi:10.1126/science.1239834

[79] F. Mahmood, C.-K. Chan, Z. Alpichshev, et al.: “Selective scattering between Floquet-Bloch and Volkov states in a topological insulator”, Nat. Phys. **12**, 306 (2016) doi:10.1038/nphys3609

[80] E. J. Sie, C. M. Nyby, C. D. Pemmaraju, et al.: “An ultrafast symmetry switch in a Weyl semimetal”, Nature **565**, 61 (2019) doi:10.1038/s41586-018-0809-4

[81] F. Aryasetiawan, L. Hedin, K. Karlsson: “Multiple Plasmon Satellites in Na and Al Spectral Functions from Ab Initio Cumulant Expansion”, Phys. Rev. Lett. **77**, 2268–2271 (1996) doi:10.1103/PhysRevLett.77.2268

[82] M. Guzzo, G. Lani, F. Sottile, et al.: “Valence Electron Photoemission Spectrum of Semiconductors: Ab Initio Description of Multiple Satellites”, Phys. Rev. Lett. **107**, 166401 (2011) doi:10.1103/PhysRevLett.107.166401

[83] M. Guzzo, J. J. Kas, L. Sponza, et al.: “Multiple satellites in materials with complex plasmon spectra: From graphite to graphene”, Phys. Rev. B **89**, 085425 (2014) doi:10.1103/PhysRevB.89.085425

[84] J. S. Zhou, M. Gatti, J. J. Kas, et al.: “Cumulant Green’s function calculations of plasmon satellites in bulk sodium: Influence of screening and the crystal environment”, Phys. Rev. B **97**, 035137 (2018) doi:10.1103/PhysRevB.97.035137

[85] Z. Chen, C. Giorgetti, J. Sjakste, et al.: “Ultrafast electron dynamics reveal the high potential of InSe for hot-carrier optoelectronics”, Phys. Rev. B **97**, 241201 (2018) doi:10.1103/PhysRevB.97.241201

[86] Z. Chen, J. Dong, E. Papalazarou, et al.: “Band Gap Renormalization, Carrier Multiplication, and Stark Broadening in Photoexcited Black Phosphorus”, Nano Letters **19**, 488–493 (2019) doi:10.1021/acs.nanolett.8b04344 eprint: https://doi.org/10.1021/acs.nanolett.8b04344

[87] J. Bert, B. Kalisky, C. Bell, et al.: “Direct imaging of the coexistence of ferromagnetism and superconductivity at the $LaAlO_3/SrTiO_3$ interface”, Nature Physics **7**, 767 (2011) doi:10.1038/nphys2079

[88] C. Cancellieri, A. Mishchenko, U. Aschauer, et al.: “Polaronic metal state at the $LaAlO_3/SrTiO_3$ interface”, Nat. Commun. **7** (2016) doi:10.1038/ncomms10386

[89] Z. Wang, S. M. Walker, A. Tamai, et al.: “Tailoring the nature and strength ofelectron–phonon interactions in the $SrTiO_3$(001)2D electron liquid”, Nature Materials **15**, 835–839 (2016) doi:10.1038/NMAT4623

[90] L. Dudy, M. Sing, P. Scheiderer, et al.: “In Situ Control of Separate Electronic Phases on $SrTiO_3$ Surfaces by Oxygen Dosing”, Advanced Materials **28**, 7443–7449 (2016) doi:10.1002/adma.201600046 eprint: https://onlinelibrary.wiley.com/doi/pdf/10.1002/adma.201600046

[91] J. Gabel, M. Zapf, P. Scheiderer, et al.: “Disentangling specific versus generic doping mechanisms in oxide heterointerfaces”, Phys. Rev. B **95**, 195109 (2017) doi:10.1103/PhysRevB.95.195109

[92] J. Lischner, D. Vigil-Fowler, S. G. Louie: “Physical Origin of Satellites in Photoemission of Doped Graphene: An Ab Initio *GW* Plus Cumulant Study”, Phys. Rev. Lett. **110**, 146801 (2013) doi:10.1103/PhysRevLett.110.146801

[93] P. Vogt, P. De Padova, C. Quaresima, et al.: “Silicene: Compelling Experimental Evidence for Graphenelike Two-Dimensional Silicon”, Phys. Rev. Lett. **108**, 155501 (2012) doi:10.1103/PhysRevLett.108.155501

[94] J. Sha, J. Niu, X. Ma, et al.: “Silicon Nanotubes”, Advanced Materials **14**, 1219–1221 (2002) doi:10.1002/1521-4095(20020903)14:17<1219::AID-ADMA1219>3.0.CO;2-T eprint: https://onlinelibrary.wiley.com/doi/pdf/10.1002/1521-4095282002090329143A173C12193A3AAID-ADMA12193E3.0.CO3B2-T

[95] A. I. Hochbaum, R. Chen, R. D. Delgado, et al.: “Enhanced thermoelectric performance of rough silicon nanowires”, Nature **451**, 163 (2008) doi:10.1038/nature06381

[96] D. Zschech, D. H. Kim, A. P. Milenin, et al.: “Ordered Arrays of 100-Oriented Silicon Nanorods by CMOS-Compatible Block Copolymer Lithography”, Nano Lett. **7**, 1516 (2007) doi:10.1021/nl070275d

[97] B. Aufray, A. Kara, S. Vizzini, et al.: “Graphene-like silicon nanoribbons on Ag(110): A possible formation of silicene”, Applied Physics Letters **96**, 183102 (2010) doi:10.1063/1.3419932 eprint: https://doi.org/10.1063/1.3419932

[98] Z. Pei, H. Hwang: “Formation of silicon nano-dots in luminescent silicon nitride”, Applied Surface Science **212-213**, 760–764 (2003) doi:https://doi.org/10.1016/S0169-4332(03)00369-6

[99] C. Chen, Z. Zhu, D. Zha, et al.: “The magnetic and transport properties of edge passivated silicene nanoribbon by Mn atoms”, Chemical Physics Letters **646**, 148–152 (2016) doi:https://doi.org/10.1016/j.cplett.2016.01.027

[100] Z. Bao, J. Sun, X. Zhao, et al.: “Top-down nanofabrication of silicon nanoribbon field effect transistor (Si-NR FET) for carcinoembryonic antigen detection”, International Journal of Nanomedicine **12**, 4623–4631 (2017) doi:10.2147/IJN.S135985

[101] X. Chen, H. Zhang, R. H. Tunuguntla, et al.: “Silicon Nanoribbon pH Sensors Protected by a Barrier Membrane with Carbon Nanotube Porins”, Nano Lett. **19**, 629 (2019) doi:10.1021/acs.nanolett.8b02898

[102] D. Chi, K. Johnson, G. Andrew, et al. (eds.): *2D Semiconductor Materials and Devices, Chapter 8* (Springer 2020)

[103] R. Hiraoka, C.-L. Lin, K. Nakamura, et al.: “Transport characteristics of a silicene nanoribbon on Ag(110)”, J. Nanotechnol. **8**, 1699 (2017) doi:10.3762/bjnano.8.170

[104] J. I. Cerdá, J. Sławińska, G. L. Lay, et al.: “Unveiling the pentagonal nature of perfectly aligned single-and double-strand Si nano-ribbons on Ag(110)”, Nat. Comm. **7** (2016) doi:10.1038/ncomms13076

[105] K. Y. Yoshinori Tokura, A. Tsukazaki: “Magnetic topological insulators”, Nat Rev Phys 1, 126–143 (2019) **1**, 126 (2019) doi:10.1038/s42254-018-0011-5

[106] M. M. Otrokov, I. I. Klimovskikh, H. Bentmann, et al.: “Prediction and observation of an antiferromagnetic topological insulator”, Nature **576**, 416 (2019) doi:10.1038/s41586-019-1840-9

[107] E. D. L. Rienks, S. Wimmer, J. Sánchez-Barriga, et al.: “Large magnetic gap at the Dirac point in Bi_2Te_3/$MnBi_2Te_4$ heterostructures”, Nature **576**, 423 (2019) doi:10.1038/s41586-019-1826-7

[108] J. Sánchez-Barriga, E. Golias, A. Varykhalov, et al.: “Ultrafast spin-polarization control of Dirac fermions in topological insulators”, Phys. Rev. B **93**, 155426 (2016) doi:10.1103/PhysRevB.93.155426

[109] J. Sánchez-Barriga, M. Battiato, M. Krivenkov, et al.: “Subpicosecond spin dynamics of excited states in the topological insulator Bi_2Te_3”, Phys. Rev. B **95**, 125405 (2017) doi:10.1103/PhysRevB.95.125405

[110] J. W. McIver, D. Hsieh, H. Steinberg, et al.: “Control over topological insulator photocurrents with light polarization”, Nature Nanotec. **7**, 96 (2012) doi:10.1038/nnano.2011.214

[111] A. S. Ketterl, S. Otto, M. Bastian, et al.: “Origin of spin-polarized photocurrents in the topological surface states of Bi_2Se_3”, Phys. Rev. B **98**, 155406 (2018) doi:10.1103/PhysRevB.98.155406

[112] P. S. Mandal, G. Springholz, V. V. Volobuev, et al.: “Topological quantum phase transition from mirror to time reversal symmetry protected topological insulator”, Nat. Commun. **8**, 968 (2017) doi:0.1038/s41467-017-01204-0

[113] J. A. Sobota, S. Yang, J. G. Analytis, et al.: “Ultrafast Optical Excitation of a Persistent Surface-State Population in the Topological Insulator Bi_2Se_3”, Phys. Rev. Lett. **108**, 117403 (2012) doi:10.1103/PhysRevLett.108.117403

[114] M. Neupane, S.-Y. Xu, Y. Ishida, et al.: “Gigantic Surface Lifetime of an Intrinsic Topological Insulator”, Phys. Rev. Lett. **115**, 116801 (2015) doi:10.1103/PhysRevLett.115.116801

[115] K. Kuroda, J. Reimann, J. Güdde, et al.: “Generation of Transient Photocurrents in the Topological Surface State of Sb_2Te_3 by Direct Optical Excitation with Midinfrared Pulses”, Phys. Rev. Lett. **116**, 076801 (2016) doi:10.1103/PhysRevLett.116.076801

[116] S. S. P. Parkin, M. Hayashi, L. Thomas: “Magnetic Domain-Wall Racetrack Memory”, Science **320**, 190–194 (2008) doi:10.1126/science.1145799 eprint: https://science.sciencemag.org/content/320/5873/190.full.pdf

[117] O. Boulle, J. Vogel, H. Yang, et al.: “Room-temperature chiral magnetic skyrmions in ultrathin magnetic nanostructures”, Nature Nanotec. **11**, 449 (2016) doi:10.1038/nnano.2015.315

[118] S. Woo, K. M. Song, H.-S. Han, et al.: “Spin-orbit torque-driven skyrmion dynamics revealed by time-resolved X-ray microscopy”, Nature Comm. **8**, 15573 (2017) doi:10.1038/ncomms15573

[119] K. Litzius, I. Lemesh, B. Krüger, et al.: “Skyrmion Hall effect revealed by direct time-resolved X-ray microscopy”, Nature Phys. **13**, 170 (2017) doi:10.1038/nphys4000

[120] C. von Korff Schmising, B. Pfau, M. Schneider, et al.: “Imaging Ultrafast Demagnetization Dynamics after a Spatially Localized Optical Excitation”, Phys. Rev. Lett. **112**, 217203 (2014) doi:10.1103/PhysRevLett.112.217203

[121] S. Yamamoto, M. Taguchi, T. Someya, et al.: “Ultrafast spin-switching of a ferrimagnetic alloy at room temperature traced by resonant magneto-optical Kerr effect using a seeded free electron laser”, Review of Scientific Instruments **86**, 083901 (2015) doi:10.1063/1.4927828 eprint: https://doi.org/10.1063/1.4927828

[122] E. Jal, M. Makita, B. Rösner, et al.: “Single-shot time-resolved magnetic x-ray absorption at a free-electron laser”, Phys. Rev. B **99**, 144305 (2019) doi:10.1103/PhysRevB.99.144305

[123] S.-G. Je, P. Vallobra, T. Srivastava, et al.: “Creation of Magnetic Skyrmion Bubble Lattices by Ultrafast Laser inUltrathin Films”, Nano Lett. **18**, 7362 (2018) doi:10.1021/acs.nanolett.8b03653

[124] F. Büttner, B. Pfau, M. Böttcher, et al.: “Observation of fluctuation-mediated picosecond nucleation of a topological phase”, Nat. Mater. **20**, 30 (2021) doi:10.1038/s41563-020-00807-1

[125] V. Baltz, A. Manchon, M. Tsoi, et al.: “Antiferromagnetic spintronics”, Rev. Mod. Phys. **90**, 015005 (2018) doi:10.1103/RevModPhys.90.015005

[126] M. C. Hanna, A. J. Nozik: “Solar conversion efficiency of photovoltaic and photoelectrolysis cells with carrier multiplication absorbers”, Journal of Applied Physics **100**, 074510 (2006) doi:10.1063/1.2356795 eprint: https://doi.org/10.1063/1.2356795

[127] M. W. B. Wilson, A. Rao, B. Ehrler, et al.: “Singlet Exciton Fission in Polycrystalline Pentacene: From Photophysics toward Devices”, Acc. Chem. Res. **46**, 1330 (2013) doi:10.1021/ar300345h

[128] J. Xia, S. N. Sanders, W. Cheng, et al.: “Singlet Fission: Progress and Prospects in Solar Cells”, Advanced Materials **29**, 1601652 (2017) doi:10.1002/adma.201601652 eprint: https://onlinelibrary.wiley.com/doi/pdf/10.1002/adma.201601652

[129] P. M. Zimmerman, F. Bell, D. Casanova, et al.: “Mechanism for Singlet Fission in Pentacene and Tetracene: From Single Exciton to Two Triplets”, J. Am. Chem. Soc. **133**, 19944 (2011) doi:10.1021/ja208431r eprint: https://pubs.acs.org/doi/pdf/10.1021/ja208431r

[130] M. T. Trinh, A. Pinkard, A. B. Pun, et al.: “Distinct properties of the triplet pair state from singlet fission”, Science Advances **3** (2017) doi:10.1126/sciadv.1700241 eprint: https://advances.sciencemag.org/content/3/7/e1700241.full.pdf

[131] R. Costantini, R. Faber, A. Cossaro, et al.: “Picosecond timescale tracking of pentacene triplet excitons with chemical sensitivity”, Comm. Physics **2**, 56 (2019) doi:10.1038/s42005-019-0157-1

[132] Z. Liu, A. A. Yasseri, J. S. Lindsey, et al.: “Molecular Memories That Survive Silicon Device Processing and Real-World Operation”, Science **302**, 1543–1545 (2003) doi:10.1126/science.1090677 eprint: https://science.sciencemag.org/content/302/5650/1543.full.pdf

[133] J. C. Scott: “Is There an Immortal Memory?”, Science **304**, 62–63 (2004) doi:10.1126/science.1095520 eprint: https://science.sciencemag.org/content/304/5667/62.full.pdf

[134] J. C. Scott, L. D. Bozano: “Nonvolatile Memory Elements Based on Organic Materials”, Advanced Materials **19**, 1452–1463 (2007) doi:10.1002/adma.200602564 eprint: https://onlinelibrary.wiley.com/doi/pdf/10.1002/adma.200602564

[135] L. Bozano, B. Kean, M. Beinhoff, et al.: “Organic Materials and Thin-Film Structures for Cross-Point Memory Cells Based on Trapping in Metallic Nanoparticles”, Advanced Functional Materials **15**, 1933–1939 (2005) doi:10.1002/adfm.200500130 eprint: https://onlinelibrary.wiley.com/doi/pdf/10.1002/adfm.200500130

[136] Y. Yang, J. Ouyang, L. Ma, et al.: “Electrical Switching and Bistability in Organic/Polymeric Thin Films and Memory Devices”, Advanced Functional Materials **16**, 1001–1014 (2006) doi:10.1002/adfm.200500429 eprint: https://onlinelibrary.wiley.com/doi/pdf/10.1002/adfm.200500429

[137] D. Tondelier, K. Lmimouni, D. Vuillaume, et al.: “Metalorganicmetal bistable memory devices”, Applied Physics Letters **85**, 5763–5765 (2004) doi:10.1063/1.1829166 eprint: https://doi.org/10.1063/1.1829166

[138] L. P. Ma, J. Liu, Y. Yang: “Organic electrical bistable devices and rewritable memory cells”, Applied Physics Letters **80**, 2997–2999 (2002) doi:10.1063/1.1473234 eprint: https://doi.org/10.1063/1.1473234

[139] L. Ma, J. Liu, S. Pyo, et al.: “Organic bistable light-emitting devices”, Applied Physics Letters **80**, 362–364 (2002) doi:10.1063/1.1436274 eprint: https://doi.org/10.1063/1.1436274

[140] D. Prime, S. Paul, P. W. Josephs-Franks: “Gold nanoparticle charge trapping and relation to organic polymer memory devices”, Philosophical Transactions of the Royal Society A: Mathematical, Physical and Engineering Sciences **367**, 4215–4225 (2009) doi:10.1098/rsta.2009.0141 eprint: https://royalsocietypublishing.org/doi/pdf/10.1098/rsta.2009.0141

[141] J. Ouyang, C.-W. Chu, C. R. Szmanda, et al.: “Programmable polymer thin film and non-volatile memory device”, Nature Mater. **3**, 918 (2004) doi:/10.1038/nmat1269

[142] E. König, K. Madeja: “Unusual magnetic behaviour of some iron(II)–bis-(1,10-phenanthroline) complexes”, Chem. Commun. (London), 61–62 (1966) doi:10.1039/C19660000061

[143] P. Gütlich, Y. Garcia, H. A. Goodwin: “Spin crossover phenomena in Fe() complexes”, Chem. Soc. Rev. **29**, 419–427 (2000) doi:10.1039/B003504L

[144] A. Hauser: “Reversibility of light-induced excited spin state trapping in the Fe(ptz)6(BF4)2, and the Zn1xFex(ptz)6(BF4)2 spin-crossover systems”, Chemical Physics Letters **124**, 543–548 (1986) doi:https://doi.org/10.1016/0009-2614(86)85073-4

[145] M. Marchivie, P. Guionneau, J. A. K. Howard, et al.: “Structural Characterization of a Photoinduced Molecular Switch”, J. Am. Chem. Soc. **124**, 194 (2001) doi:10.1021/ja016980k

[146] K. Kato, M. Takata, Y. Moritomo, et al.: “On-off optical switching of the magnetic and structural properties in a spin-crossover complex”, Applied Physics Letters **90**, 201902 (2007) doi:10.1063/1.2736213 eprint: https://doi.org/10.1063/1.2736213

[147] A. Bousseksou, G. Molnár, J.-P. Tuchagues, et al.: “Triggering the spin-crossover of Fe(phen)2(NCS)2 by a pressure pulse. Pressure and magnetic field induce ‘mirror effects’”, Comptes Rendus Chimie **6**, 329–335 (2003) doi:https://doi.org/10.1016/S1631-0748(03)00042-0

[148] N. Baadji, M. Piacenza, T. Tugsuz, et al.: “Electrostatic spin crossover effect in polar magnetic molecules”, Nature Mater. **8**, 813 (2009) doi:10.1038/nmat2525

[149] V. Meded, A. Bagrets, K. Fink, et al.: “Electrical control over the Fe(II) spin crossover in a single molecule: Theory and experiment”, Phys. Rev. B **83**, 245415 (2011) doi:10.1103/PhysRevB.83.245415

[150] T. Miyamachi, M. Gruber, V. Davesne, et al.: “Robust spin crossover and memristance across a single molecule”, Nature Comm. **3**, 93 (2012) doi:10.1038/ncomms1940

[151] M. Reiher: “Theoretical Study of the $Fe(phen)_2(NCS)_2$ Spin-Crossover Complex with Reparametrized Density Functionals”, Inorg. Chem. **41**, 6928 (2002) doi:10.1021/ic025891l

[152] S. Khanra, B. Biswas, C. Golze, et al.: “A spin-frustrated star-shaped heterotetranuclear CrIIIMnII3 species and its magnetic and HF-EPR measurements”, Dalton Trans. 481–487 (2007) doi:10.1039/B613293F

[153] M. T. Pope, A. Müller: “Polyoxometalate Chemistry: An Old Field with New Dimensions in Several Disciplines”, Angewandte Chemie International Edition in English **30**, 34–48 (1991) doi:10.1002/anie.199100341 eprint: https://onlinelibrary.wiley.com/doi/pdf/10.1002/anie.199100341

[154] F. Piga, F. Moro, I. Krivokapic, et al.: “Magnetic properties of a novel family of ferrous cubanes”, Chem. Commun. **48**, 2430–2432 (2012) doi:10.1039/C2CC16853G

[155] S. Kahle, Z. Deng, N. Malinowski, et al.: “The Quantum Magnetism of Individual Manganese-12-Acetate Molecular Magnets Anchored at Surfaces”, Nano Lett. **12**, 518 (2012) doi:/10.1021/nl204141z

[156] P. Puschnig, S. Berkebile, A. J. Fleming, et al.: “Reconstruction of Molecular Orbital Densities from Photoemission Data”, Science **326**, 702–706 (2009) doi:10.1126/science.1176105 eprint: https://science.sciencemag.org/content/326/5953/702.full.pdf

[157] M. Wießner, D. Hauschild, C. Sauer, et al.: “Complete determination of molecular orbitals by measurement of phase symmetry and electron density”, Nat. Commun. **5**, 4156 (2014) doi:10.1038/ncomms5156

[158] D. Yoshimura, H. Ishii, Y. Ouchi, et al.: “Angle-resolved ultraviolet photoelectron spectroscopy and theoretical simulation of a well-ordered ultrathin film of tetratetracontane ($n - C_{44}H_{90}$) on Cu(100): Molecular orientation and intramolecular energy-band dispersion”, Phys. Rev. B **60**, 9046–9060 (1999) doi:10.1103/PhysRevB.60.9046

[159] M. Grimm, C. Metzger, M. Graus, et al.: “Molecular orbital imaging beyond the first monolayer: Insights into the pentacene/Ag(110) interface”, Phys. Rev. B **98**, 195412 (2018) doi:10.1103/PhysRevB.98.195412

[160] K. Baumgärtner, M. Reuner, C. Metzger, et al.: “Ultrafast molecular orbital tomography of a pentacene thin film using time-resolved momentum microscopy at a free-electron laser”, Nature Comm. submitted (2021)

[161] J. Osterwalder, T. Greber, P. Aebi, et al.: “Final-state scattering in angle-resolved ultraviolet photoemission from copper”, Phys. Rev. B **53**, 10209–10216 (1996) doi:10.1103/PhysRevB.53.10209

[162] P. Krüger: “Photoelectron Diffraction from Valence States of Oriented Molecules”, Journal of the Physical Society of Japan **87**, 061007 (2018) doi:10.7566/JPSJ.87.061007 eprint: https://doi.org/10.7566/JPSJ.87.061007

[163] D. Woodruff: “Photoelectron Diffraction”, in: *Encyclopedia of Materials: Science and Technology*, ed. by K. J. Buschow, R. W. Cahn, M. C. Flemings, et al. (Elsevier, Oxford 2001), pp. 6925–6929 doi:https://doi.org/10.1016/B0-08-043152-6/01227-4

[164] M. Greif, L. Kasmi, L. Castiglioni, et al.: “Access to phases of coherent phonon excitations by femtosecond ultraviolet photoelectron diffraction”, Phys. Rev. B **94**, 054309 (2016) doi:10.1103/PhysRevB.94.054309

[165] A. Nilsson, J. LaRue, H. Öberg, et al.: “Catalysis in real time using X-ray lasers”, Chemical Physics Letters **675**, 145–173 (2017) doi:https://doi.org/10.1016/j.cplett.2017.02.018

[166] J. L. LaRue, T. Katayama, A. Lindenberg, et al.: “THz-Pulse-Induced Selective Catalytic CO Oxidation on Ru”, Phys. Rev. Lett. **115**, 036103 (2015) doi:10.1103/PhysRevLett.115.036103

[167] Y. Zhang, D. Payne, C. Pang, et al.: “State-Selective Dynamics of TiO_2 Charge-Carrier Trapping and Recombination”, J. Phys Chem. Lett. **10**, 5265 (2019) doi:10.1021/acs.jpclett.9b02153

[168] M. Borgwardt, M. Wilke, T. Kampen, et al.: “Charge Transfer Dynamics at Dye-Sensitized ZnO and TiO_2 Interfaces Studied by Ultrafast XUV Photoelectron Spectroscopy”, Sci. Rep. **6**, 2422 (2016) doi:10.1038/srep24422

[169] D. Niesner, H. Zhu, K. Miyata, et al.: “Persistent Energetic Electrons in Methylammonium Lead Iodide Perovskite Thin Films”, Journal of the American Chemical Society **138**, 15717 (2016) doi:10.1021/jacs.6b08880

[170] A. FUJISHIMA, K. HONDA: “Electrochemical Photolysis of Water at a Semiconductor Electrode”, Nature **238**, 37 (1972) doi:10.1038/238037a0

[171] J. P. W. Treacy, H. Hussain, X. Torrelles, et al.: “Geometric structure of anatase $TiO_2(101)$”, Phys. Rev. B **95**, 075416 (2017) doi:10.1103/PhysRevB.95.075416

[172] H. Hussain, G. Tocci, T. Woolcot, et al.: “Structure of a model TiO_2 photocatalytic interface”, Nature Materials **16**, 461 (2017) doi:10.1038/nmat4793

[173] I. M. Nadeem, J. P. W. Treacy, S. Selcuk, et al.: “Water Dissociates at the Aqueous Interface with Reduced Anatase TiO_2 (101)”, The Journal of Physical Chemistry Letters **9**, 3131–3136 (2018) doi:10.1021/acs.jpclett.8b01182

[174] U. Diebold: “The surface science of titanium dioxide”, Surface Science Reports **48**, 53–229 (2003) doi:https://doi.org/10.1016/S0167-5729(02)00100-0

[175] H. G. Yang, C. H. Sun, S. Z. Qiao, et al.: “Anatase TiO_2 single crystals with a large percentage of reactive facets”, Nature **453**, 638 (2008) doi:10.1038/nature06964

[176] J. Blomquist, L. E. Walle, P. Uvdal, et al.: “Water Dissociation on Single Crystalline Anatase TiO_2(001) Studied by Photoelectron Spectroscopy”, The Journal of Physical Chemistry C **112**, 16616–16621 (2008) doi:10.1021/jp805664b

[177] S. Wendt, J. Matthiesen, R. Schaub, et al.: “Formation and Splitting of Paired Hydroxyl Groups on Reduced $TiO_2(110)$”, Phys. Rev. Lett. **96**, 066107 (2006) doi:10.1103/PhysRevLett.96.066107

[178] N. J. Divins, I. Angurell, C. Escudero, et al.: “Influence of the support on surface rearrangements of bimetallic nanoparticles in real catalysts”, Science **346**, 620–623 (2014) doi:10.1126/science.1258106 eprint: https://science.sciencemag.org/content/346/6209/620.full.pdf

[179] K. Medjanik, O. Fedchenko, S. Chernov, et al.: “Direct 3D mapping of the Fermi surface and Fermi velocity”, Nature Mat. **16**, 615 (2017) doi:10.1038/nmat4875

[180] J. Tusche, A. Krasyuk, J. Kirschner, et al., German Patent DE 10 2013 005 173, issued March 2015

[181] G. Schonhense, A. Oelsner, O. Schmidt, et al.: “Time-of-flight photoemission electron microscopy – a new way to chemical surface analysis”, Surface Science **480**, 180–187 (2001) doi:10.1016/S0039-6028(01)00833-0

[182] G. Schönhense, H. Spiecker, J. Vac. Sci. Technol. B **20**, 2526 (2002); US Patent 6,737,647 B2; German Patent DE 102 17 507 B4

[183] C. Tusche, A. Krasyuk, J. Kirschner: “Spin resolved bandstructure imaging with a high resolution momentum microscope”, Ultramicroscopy **159**, 520–529 (2015) doi:10.1016/j.ultramic.2015.03.020

[184] D. Kutnyakhov, S. Chernov, K. Medjanik, et al.: “Spin texture of time-reversal symmetry invariant surface states on W(110)”, Scientific Rep. **6**, 29394 (2016) doi:10.1038/srep29394

[185] G. Schönhense, K. Medjanik, S. Chernov, et al.: “Spin-filtered time-of-flight k-space microscopy of Ir – Towards the “complete” photoemission experiment”, Ultramicroscopy **183**, 19–29 (2017) doi:https://doi.org/10.1016/j.ultramic.2017.06.025

[186] H. J. Elmers, D. Kutnyakhov, S. V. Chernov, et al.: “Hosting of surface states in spin–orbit induced projected bulk band gaps of W(1 1 0) and Ir(1 1 1)”, Journal of Physics: Condensed Matter **29**, 255001 (2017) doi:10.1088/1361-648x/aa7173

[187] S. Chernov, K. Medjanik, C. Tusche, et al.: “Anomalous d-like surface resonances on Mo(110) analyzed by time-of-flight momentum microscopy”, Ultramicroscopy **159**, 453–463 (2015) doi:10.1016/j.ultramic.2015.07.008

[188] H. J. Elmers, R. Wallauer, M. Liebmann, et al.: “Spin mapping of surface and bulk Rashba states in ferroelectric α-GeTe(111) films”, Phys. Rev. B **94**, 201403 (2016) doi:10.1103/PhysRevB.94.201403

[189] A. Kronenberg, J. Braun, J. Minár, et al.: “Dirac cone and pseudogapped density of states in the topological half-Heusler compound YPtBi”, Phys. Rev. B **94**, 161108 (2016) doi:10.1103/PhysRevB.94.161108

[190] M. Jourdan, J. Minár, J. Braun, et al.: “Direct observation of half-metallicity in the Heusler compound Co_2MnSi”, Nature Commun. **5**, 3974 (2014) doi:10.1038/ncomms4974

[191] C. Tusche, P. Goslawski, D. Kutnyakhov, et al.: “Multi-MHz time-of-flight electronic bandstructure imaging of graphene on Ir(111)”, Applied Physics Letters **108**, 261602 (2016) doi:10.1063/1.4955015

[192] A. Zaporozhchenko-Zymaková, D. Kutnyakhov, K. Medjanik, et al.: “Momentum-resolved photoelectron absorption in surface barrier scattering on Ir(111) and graphene/Ir(111)”, Phys. Rev. B **96**, 155108 (2017) doi:10.1103/PhysRevB.96.155108

[193] B. Schönhense, K. Medjanik, O. Fedchenko, et al.: “Multidimensional photoemission spectroscopy—the space-charge limit”, New Journal of Physics **20**, 033004 (2018) doi:10.1088/1367-2630/aaa262

[194] http:www.surface-concept.com

[195] G. Schönhense, K. Medjanik, S. Babenkov, et al.: “Momentum-transfer model of valence-band photoelectron diffraction”, arXiv:1806.05871 (2018)

[196] O. Fedchenko, K. Medjanik, S. Chernov, et al.: “4D texture of circular dichroism in soft-x-ray photoemission from tungsten”, New Journal of Physics **21**, 013017 (2019) doi:10.1088/1367-2630/aaf4cd

[197] H. B. Gray, J. R. Winkler: “Living with Oxygen”, Acc. Chem. Res. **51**, 1850 (2018) doi:10.1021/acs.accounts.8b00245

[198] M. Kubin, J. Kern, S. Gul, et al.: “Soft x-ray absorption spectroscopy of metalloproteins and high-valent metal-complexes at room temperature using free-electron lasers”, Structural Dynamics **4**, 054307 (2017) doi:10.1063/1.4986627

[199] M. Kubin, M. Guo, T. Kroll, et al.: “Probing the oxidation state of transition metal complexes: a case study on how charge and spin densities determine Mn L-edge X-ray absorption energies”, Chem. Sci. **9**, 6813–6829 (2018) doi:10.1039/C8SC00550H

[200] P. Wernet, K. Kunnus, I. Josefsson, et al.: “Orbital-specific mapping of the ligand exchange dynamics of $Fe(CO)_5$ in solution”, Nature **520**, 78 (2015) doi:10.1038/nature14296

[201] R. Mitzner, J. Rehanek, J. Kern, et al.: “L-Edge X-ray Absorption Spectroscopy of Dilute Systems Relevant to Metalloproteins Using an X-ray Free-Electron Laser”, J. Phys. Chem. Lett. **4**, 3641 (2013) doi:10.1021/jz401837f

[202] P. Micke, S. Kuhn, L. Buchauer, et al.: “The Heidelberg compact electron beam ion traps”, Review of Scientific Instruments **89**, 063109 (2018) doi:10.1063/1.5026961

[203] L. Schmöger, O. O. Versolato, M. Schwarz, et al.: “Coulomb crystallization of highly charged ions”, Science **347**, 1233–1236 (2015) doi:10.1126/science.aaa2960

[204] P. Micke, Private Communication

[205] M. G. Kozlov, M. S. Safronova, J. R. Crespo López-Urrutia, et al.: “Highly charged ions: Optical clocks and applications in fundamental physics”, Rev. Mod. Phys. **90**, 045005 (2018) doi:10.1103/RevModPhys.90.045005

[206] R. E. Marrs, M. A. Levine, D. A. Knapp, et al.: “Measurement of electron-impact–excitation cross sections for very highly charged ions”, Phys. Rev. Lett. **60**, 1715–1718 (1988) doi:10.1103/PhysRevLett.60.1715

[207] M. A. Levine, R. E. Marrs, J. R. Henderson, et al.: “The Electron Beam Ion Trap: A New Instrument for Atomic Physics Measurements”, Physica Scripta **T22**, 157–163 (1988) doi:10.1088/0031-8949/1988/t22/024

[208] M. Levine, R. Marrs, J. Bardsley, et al.: “The use of an electron beam ion trap in the study of highly charged ions”, Nuclear Instruments and Methods in Physics Research Section B: Beam Interactions with Materials and Atoms **43**, 431–440 (1989) doi:10.1016/0168-583X(89)90386-8

[209] J. D. Gillaspy: “Highly charged ions”, Journal of Physics B: Atomic, Molecular and Optical Physics **34**, R93–R130 (2001) doi:10.1088/0953-4075/34/19/201

[210] F. (Currell: *The Physics of Multiply and Highly Charged Ions* (Springer 2003)

[211] S. W. Epp, J. R. C. López-Urrutia, G. Brenner, et al.: “Soft X-Ray Laser Spectroscopy on Trapped Highly Charged Ions at FLASH”, Phys. Rev. Lett. **98**, 183001 (2007) doi:10.1103/PhysRevLett.98.183001

[212] S. Bernitt, G. V. Brown, J. K. Rudolph, et al.: “An unexpectedly low oscillator strength as the origin of the Fe XVII emission problem”, Nature **492**, 225 (2012) doi:10.1038/nature11627

[213] M. C. Simon, J. R. Crespo López-Urrutia, C. Beilmann, et al.: “Resonant and Near-Threshold Photoionization Cross Sections of Fe^{14+}”, Phys. Rev. Lett. **105**, 183001 (2010) doi:10.1103/PhysRevLett.105.183001

[214] M. C. Simon, M. Schwarz, S. W. Epp, et al.: “Photoionization of N3 and Ar8 in an electron beam ion trap by synchrotron radiation”, Journal of Physics B: Atomic, Molecular and Optical Physics **43**, 065003 (2010) doi:10.1088/0953-4075/43/6/065003

[215] R. Steinbrügge, S. Bernitt, S. W. Epp, et al.: “Absolute measurement of radiative and Auger rates of K − shell − vacancy states in highly charged Fe ions”, Phys. Rev. A **91**, 032502 (2015) doi:10.1103/PhysRevA.91.032502

[216] J. K. Rudolph, S. Bernitt, S. W. Epp, et al.: “X-Ray Resonant Photoexcitation: Linewidths and Energies of $K\alpha$ Transitions in Highly Charged Fe Ions”, Phys. Rev. Lett. **111**, 103002 (2013) doi:10.1103/PhysRevLett.111.103002

[217] S. W. Epp, R. Steinbrügge, S. Bernitt, et al.: “Single-photon excitation of $K\alpha$ in heliumlike Kr^{34+}: Results supporting quantum electrodynamics predictions”, Phys. Rev. A **92**, 020502 (2015) doi:10.1103/PhysRevA.92.020502

[218] N. S. Oreshkina, S. M. Cavaletto, C. H. Keitel, et al.: “Astrophysical Line Diagnosis Requires Nonlinear Dynamical Atomic Modeling”, Phys. Rev. Lett. **113**, 143001 (2014) doi:10.1103/PhysRevLett.113.143001

[219] Y. Li, M. Fogle, S. Loch, et al.: “Non-equilibrium modeling of the Fe XVII 3C/3D ratio for an intense X-ray free electron laser”, Canadian Journal of Physics **95**, 869–877 (2017) doi:10.1139/cjp-2016-0882

[220] T. Nagayama, J. E. Bailey, G. P. Loisel, et al.: “Systematic Study of L-Shell Opacity at Stellar Interior Temperatures”, Phys. Rev. Lett. **122**, 235001 (2019) doi:10.1103/PhysRevLett.122.235001

[221] H. Collaboration: “The quiescent intracluster medium in the core of the Perseus cluster”, Nature **535**, 117 (2016) doi:10.1038/nature18627

[222] H. Collaboration: “Solar abundance ratios of the iron-peak elements in the Perseus cluster”, Nature **551**, 478 (2017) doi:10.1038/nature24301

[223] M. Mehdipour, J. S. Kaastra, T. Kallman: “Systematic comparison of photoionised plasma codes with application to spectroscopic studies of AGN in X-rays”, A&A **596**, A65 (2016) doi:10.1051/0004-6361/201628721

[224] F. Aharonian Hitomi Collaboration, H. Akamatsu, F. Akimoto, et al.: “Atomic data and spectral modeling constraints from high-resolution X-ray observations

of the Perseus cluster with Hitomi*", Publications of the Astronomical Society of Japan **70** (2018) doi:10.1093/pasj/psx156

[225] S. M. Cavaletto, Z. Harman, C. Ott, et al.: "Broadband high-resolution X-ray frequency combs", Nature Photonics **8**, 520 (2014) doi:10.1038/nphoton.2014.113

[226] C. Gohle, T. Udem, M. Herrmann, et al.: "A frequency comb in the extreme ultraviolet", Nature **436**, 234 (2005) doi:10.1038/nature03851

[227] C. Benko, T. Allison, A. Cingöz, et al.: "Extreme ultraviolet radiation with coherence time greater than 1 s", Nature Photonics **8**, 530 (2014) doi:10.1038/nphoton.2014.132

[228] A. Cingöz, D. Yost, T. Allison, et al.: "Direct frequency comb spectroscopy in the extreme ultraviolet", Nature **482**, 68 (2012) doi:10.1038/nature10711

[229] J. R. C. López-Urrutia: "Frequency metrology using highly charged ions", Journal of Physics: Conference Series **723**, 012052 (2016) doi:10.1088/1742-6596/723/1/012052

[230] J. Nauta, A. Borodin, H. B. Ledwa, et al.: "Towards precision measurements on highly charged ions using a high harmonic generation frequency comb", Nuclear Instruments and Methods in Physics Research Section B: Beam Interactions with Materials and Atoms **408**, 285–288 (2017) doi:10.1016/j.nimb.2017.04.077

[231] S. Kempf, A. Fleischmann, L. Gastaldo, et al.: "Physics and Applications of Metallic Magnetic Calorimeters", Journal of Low Temperature Physics **193**, 365–379 (2018) doi:10.1007/s10909-018-1891-6

[232] C. A. Kilbourne, J. S. Adams, R. P. Brekosky, et al.: "Design, implementation, and performance of the Astro-H SXS calorimeter array and anticoincidence detector", Journal of Astronomical Telescopes, Instruments, and Systems **4**, 1 - 8 –8 (2018) doi:10.1117/1.JATIS.4.1.011214

[233] T. Leopold, S. A. King, P. Micke, et al.: "A cryogenic radio-frequency ion trap for quantum logic spectroscopy of highly charged ions", Review of Scientific Instruments **90**, 073201 (2019) doi:10.1063/1.5100594

[234] P. Micke, J. Stark, S. A. King, et al.: "Closed-cycle, low-vibration 4 K cryostat for ion traps and other applications", Review of Scientific Instruments **90**, 065104 (2019) doi:10.1063/1.5088593

[235] M. S. Safronova, D. Budker, D. DeMille, et al.: "Search for new physics with atoms and molecules", Rev. Mod. Phys. **90**, 025008 (2018) doi:10.1103/RevModPhys.90.025008

[236] T. E. Chupp, P. Fierlinger, M. J. Ramsey-Musolf, et al.: "Electric dipole moments of atoms, molecules, nuclei, and particles", Rev. Mod. Phys. **91**, 015001 (2019) doi:10.1103/RevModPhys.91.015001

[237] J. R. Crespo López-Urrutia, P. Beiersdorfer, K. Widmann, et al.: "Nuclear magnetization distribution radii determined by hyperfine transitions in the 1*s*

level of H-like ions $^{185}Re^{74+}$ and $^{187}Re^{74+}$", Phys. Rev. A **57**, 879–887 (1998) doi:10.1103/PhysRevA.57.879

[238] S. R. Elliott, P. Beiersdorfer, M. H. Chen, et al.: "Measurements of the differences in the nuclear charge radii among uranium isotopes", Phys. Rev. C **57**, 583–589 (1998) doi:10.1103/PhysRevC.57.583

[239] C. Brandau, C. Kozhuharov, Z. Harman, et al.: "Isotope Shift in the Dielectronic Recombination of Three-Electron $^{A}Nd^{57+}$", Phys. Rev. Lett. **100**, 073201 (2008) doi:10.1103/PhysRevLett.100.073201

[240] V. M. Shabaev, A. N. Artemyev, V. A. Yerokhin, et al.: "Towards a Test of QED in Investigations of the Hyperfine Splitting in Heavy Ions", Phys. Rev. Lett. **86**, 3959–3962 (2001) doi:10.1103/PhysRevLett.86.3959

[241] S. G. Karshenboim: "Precision physics of simple atoms: QED tests, nuclear structure and fundamental constants", Physics Reports **422**, 1–63 (2005) doi:10.1016/j.physrep.2005.08.008

[242] P. Beiersdorfer: "Testing QED and atomic-nuclear interactions with high-Zions", Journal of Physics B: Atomic, Molecular and Optical Physics **43**, 074032 (2010) doi:10.1088/0953-4075/43/7/074032

[243] J. C. Berengut, D. Budker, C. Delaunay, et al.: "Probing New Long-Range Interactions by Isotope Shift Spectroscopy", Phys. Rev. Lett. **120**, 091801 (2018) doi:10.1103/PhysRevLett.120.091801

[244] L. N. Labzowsky, A. V. Nefiodov, G. Plunien, et al.: "Parity-violation effect in heliumlike gadolinium and europium", Phys. Rev. A **63**, 054105 (2001) doi:10.1103/PhysRevA.63.054105

[245] J. Gunst, A. Surzhykov, A. Artemyev, et al.: "Parity-nonconservation effects on the radiative recombination of heavy hydrogenlike ions", Phys. Rev. A **87**, 032714 (2013) doi:10.1103/PhysRevA.87.032714

[246] A. A. Bondarevskaya, D. V. Chubukov, E. A. Mistonova, et al.: "Considerations towards the possibility of the observation of parity nonconservation in highly charged ions in storage rings", Physica Scripta **93**, 025401 (2018) doi:10.1088/1402-4896/aa9692

[247] D. A. Glazov, Y. S. Kozhedub, A. V. Maiorova, et al.: "Tests of fundamental theories with heavy ions at low-energy regime", Hyperfine Interactions **199**, 71 (2011) doi:10.1007/s10751-011-0302-z

[248] P. Beiersdorfer: "Laboratory X-Ray Astrophysics", Annual Review of Astronomy and Astrophysics **41**, 343–390 (2003) doi:10.1146/annurev.astro.41.011802.094825

[249] T. Roth, W. Freund, U. Boesenberg, et al.: "Pulse-resolved intensity measurements at a hard X-ray FEL using semi-transparent diamond detectors", Journal of Synchrotron Radiation **25**, 177–188 (2018) doi:10.1107/S1600577517015016

[250] T. Martin, A. Koch, M. Nikl: “Scintillator materials for x-ray detectors and beam monitors”, MRS Bulletin **42**, 451–457 (2017) doi:10.1557/mrs.2017.116

[251] G. L. Dakovski, M.-F. Lin, D. S. Damiani, et al.: “A novel method for resonant inelastic soft X-ray scattering *via* photoelectron spectroscopy detection”, Journal of Synchrotron Radiation **24**, 1180–1186 (2017) doi:10.1107/S1600577517011869

[252] E. Hemsing, M. Dunning, B. Garcia, et al.: “Echo-enabled harmonics up to the 75th order from precisely tailored electron beams”, Nature Photonics **10**, 512–515 (2016) doi:10.1038/nphoton.2016.101

[253] E. Allaria, R. Appio, L. Badano, et al.: “Highly coherent and stable pulses from the FERMI seeded free-electron laser in the extreme ultraviolet”, Nature Photonics **6**, 699–704 (2012) doi:10.1038/nphoton.2012.233

[254] G. Geloni, V. Kocharyan, E. Saldin: “Cost-effective way to enhance the capabilities of the LCLS baseline”, arXiv:1008.3036 (2010)

[255] D. Ratner, R. Abela, J. Amann, et al.: “Experimental Demonstration of a Soft X-Ray Self-Seeded Free-Electron Laser”, Phys. Rev. Lett. **114**, 054801 (2015) doi:10.1103/PhysRevLett.114.054801

[256] J. Feldhaus, E. Saldin, J. Schneider, et al.: “Possible application of X-ray optical elements for reducing the spectral bandwidth of an X-ray SASE FEL”, Optics Communications **140**, 341–352 (1997) doi:10.1016/S0030-4018(97)00163-6

[257] Y. Feng, J. Hastings, P. Heimann, et al.: “Optics for Self-Seeding Soft X-ray FEL Undulators”, Hilton Malmö City, Sweden, Proceedings of the 32nd International Free Electron Laser Conference (FEL 10), 270 (2010)

[258] S. Serkez: “Design and optimization of the Grating Monochromator for Soft X-Ray Self-Seeding FELs”, PhD thesis (University of Hamburg 2015)

[259] J. MacArthur, J. Duris, Z. Huang, et al.: “High Power Sub-Femtosecond X-Ray Pulse Study for the LCLS”, Copenhagen, Denmark, Proc. of International Particle Accelerator Conference (IPAC’17), Copenhagen, Denmark, 14-19 May, 2017, International Particle Accelerator Conference 8, 2848–2850 (JACoW, Geneva, Switzerland 2017) doi:10.18429/JACoW-IPAC2017-WEPAB118

[260] S. Serkez, G. Geloni, S. Tomin, et al.: “Overview of options for generating high-brightness attosecond x-ray pulses at free-electron lasers and applications at the European XFEL”, Journal of Optics **20**, 024005 (2018) doi:10.1088/2040-8986/aa9f4f

[261] J. Duris, D. Li S., T., et al.: “Tunable isolated attosecond X-ray pulses with gigawatt peak power from a free-electron laser”, Nat. Photonics **14**, 30 (2020) doi:10.1038/s41566-019-0549-5

[262] A. Yaroslavtsev, A. Scherz: “X-ray beam split and delay unit for SASE3 of the European XFEL” (2016)